Investigation of Stratified Electromagnetically Driven Flows in Electrically Conducting Fluids

Vadims Geža

Advisor: Dr. Phys. Andris Jakovičs

Faculty of Physics and Mathematics

University of Latvia

A thesis submitted for the degree of

Doctor of Physics

2015

IEGULDĪJUMS TAVĀ NĀKOTNĒ

This work has been financially supported by the European Social Fund within the project 2013/0027/1DP/1.1.1.2.0/13/APIA/VIAA/007

Acknowledgement

I would like to express my deep gratitude to Prof. Andris Jakovičs, my research supervisor, for worthful and critical remarks and his support during whole study process.

I would like to thank Prof. E.Baake and Prof. B.Nacke for opportunity to make research in ETP institute.

Special thanks to Mihails Ščepanskis un Sergejs Spitāns for fruitful discussions, which led to new ideas. I am thankful to all colleagues of Laboratory of Mathematical Modeling of Environmental and Technological Processes and colleagues of Institute of Electrotechnology (ETP), Leibniz University of Hannover for all years spent together.

I would also like to extend my thanks to the technicians of ETP, in particular Mr. Köppen and Mr. Lohan.

Last, but not least, I would like to thank my wife Lilija for love and support in toughest moments and her patience during the past few years.

Abstract

This thesis is devoted to experimental, theoretical, and numerical investigation of stratified electromagnetically driven liquid metal flow that is typical for directional solidification method used in growth of photo-voltaic silicon.

Analytical model for description of flow under simplified conditions is derived. This model is able to predict flow velocity dependence on EM force parameters, e.g. field frequency. Experimental investigation of simplified (two-dimensionalized) flow allowed finding of critical Reynolds numbers (force shape dependent) for main flow vortex merging.

Experimental setup with Wood's metal as working liquid was designed and built; where temperature and velocity measurements are performed. In the experimental results a transition between three dimensional and stratified flow is observed at the critical Lorentz force.

Large eddy simulations were validated by the experimental results. Results showed unsymmetrical, rotational flow pattern, despite symmetrical distribution of EM forces, this fact is also proved experimentally. Anisotropy of velocity pulsations was proven for stratified flow, especially at very high Richardson numbers. Turbulent Prandtl number dependence on Richardson number was found.

Contents

List of Figures

List of Tables

List of Symbols

F_{EM}	Magnetic interaction parameter, $F_{EM} = F_{max}\frac{L^3}{\rho\nu^2}$
Gr	Grashof number, $Gr = \frac{g\beta(T-T_0)L^3}{\nu^2}$
N	Brunt–Väisälä frequency, $N = \sqrt{\frac{g\beta\Delta T}{L}}$
Pe	Peclet number, $Pe = \frac{LU}{\alpha}$
Pr	Prandtl number, $Pr = \frac{\nu}{\alpha}$
Re	Reynolds number, $Re = \frac{UL}{\nu}$
Re_m	Magnetic Reynolds number, $Re_m = LU\mu_0\sigma$
Ri	Richardson number, $Ri = \frac{\beta\Delta TgL}{U^2}$
i	Imaginary unit
e	Exponent
β	Thermal expansion coefficient
δ	Skin depth of magnetic field
ν	Kinematic viscosity
Ω	Magnetic scalar potential
ω	Angular frequency
ϕ	Electric scalar potential
ρ	Mass density
σ	Electrical conductivity
$\vec{A}$	Magnetic vector potential

$\vec{B}$	Magnetic flux density
$\vec{E}$	Electric field intensity
$\vec{g}$	Free fall acceleration
$\vec{j}$	Current density
$\vec{T}$	Vector electric potential
$\vec{u}$	Velocity
I	Electric current
L	Characteristic length
p	Pressure
T	Temperature
t	Time
U	Characteristic velocity scale

Chapter 1

Introduction

1.1 Motivation of research

With the depletion of fossil energy resources, the demand for alternative energy sources is growing. In 2013 renewable energy constituted 29% of the energy produced in Germany and double the 2006 amount [1]. Photovoltaic solar energy still constitutes a small fraction of the total power production (only 5.7%) but is continuing to grow. Directional solidification (DS) is widely used for the production of photovoltaic materials in crucibles, which are usually square shaped for convenient and effective wafer production.

In the DS process, silicon ingots are produced in different sizes that keep growing to meet the demand for solar cells. The quality and price of such ingot depends primarily on the feedstock [2]. However, the success of each production step (of which two, melting and solidification, involve the liquid phase) is also crucial for such parameters as polycrystalline grain size, concentration of incorporation, dislocation, and other defects. Understanding and controlling the melt flow during the solidification phase is important for the reduction of N, C, and O incorporation and precipitation formations [3], [4], [5]. Small concentrations of SiO_2 precipitations can positively influence the melt material, while SiC and Si_3N_4 dramatically decrease the efficiency of solar cells and make material brittle in the sawing process.

1.2 The directional solidification method

Nowadays, it is nearly impossible to produce materials and technological devices without the involvement of the liquid phase of the materials and the consequent solidification phase. However, the two phases are not mutually independent. In the

production of semiconductor materials, where shape of growth interface essentially influences defect formation, control of melt motion can significantly change the output material quality. Although silicon crystals can be grown from the solution [6] or vapor [7], growth from the melt is used most frequently because of larger growth rates. Growth from melt by different techniques provides various advantages and disadvantages in terms of material quality, production rate, and production cost.

In 1916, Jan Czochralski invented the process that can be used for growing of cylindrical single crystals [8]. During the Czochralski process (CZ), single crystal seed is dipped into the melt, which is contained in quartz crucible, and later on pulled to allow start growth of the crystal. Precise control of the pull rate, crucible, and crystal rotation are essential parameters for growth of defect-free single crystal and energetic efficiency of the growth process [9]. Nowadays, crystals up to 300 mm in diameter and up to several meters in length are grown. Recently, diameters of 450 mm [10] are reported in literature – the industrial production of the crystals is expected in the near future.

The disadvantages of the CZ process are relatively slow growth rates (in comparison to floating zone method) and large production costs, more than 30 kWh/kg [11]. For silicon production, this value varies between 18 kWh/kg and 40 kWh/kg [12]. Another drawback is the nonuniformity of resistivity of wafers, which is uniform in Floating-zone process.

Floating-zone (FZ) method was developed in Bell Labs in 1950s [13] for production of high-quality materials for transistor manufacture. Today it is the most widely used method for production of high-quality low-impurity level semiconductor materials.

A schematic setup of the FZ process is shown in Figure 1.1. High-purity crack-free polycrystalline silicon rod is held in a vertical arrangement. Both rod and monocrystalline seed are partially melted by using radio-frequency magnetic fields, and the seed is brought into the contact with the droplet formed at the rod. The rotation of the seed and rod allows stabilization of the liquid silicon and prevent spilling over. The molten zone is then moved along the rod, and single crystal is grown. The benefit of the FZ over the CZ process is crucible-free arrangement, which reduces the contamination of the silicon by impurities, while production cost range is similar (30 kWh/kg). The sizes of the FZ-grown crystals are smaller than those from CZ process, typically up to 200 mm [14].

Directional solidification (DS) in broad sense means solidifying material in such a way that the direction of heat losses in the system is controlled by means of some technical devices. In current work, this term will be used only in connection with

directional solidification method for silicon growth. Its main advantage in comparison to FZ and CZ processes is a low cost (12 kWh/kg [12]) and large volumes of grown polycrystalline material, which compensate slow growth rates.

The schematic principle of DS method is shown in Figure 1.2. The system consists of quartz crucible, which is initially filled with raw silicon (scrap or powder). Another necessary components are heater and heat sink to control thermal conditions in the furnace, for example, to melt the silicon during initial stage and later on to control growth rate of mc-Si (multicrystalline silicon). Various options for such furnace design exist. Instead of using heat sink, moving crucible can be used, which is pulled out of the hot zone [16]. Heaters positioned on sides of the crucible [17], [18] as well as on top (like in schematic drawing) are found in literature. Inductors are optional and depend on system design. Various magnetic fields are applied in silicon growth techniques – alternating magnetic field [19], traveling magnetic fields [20], [21], and rotating magnetic fields [22].

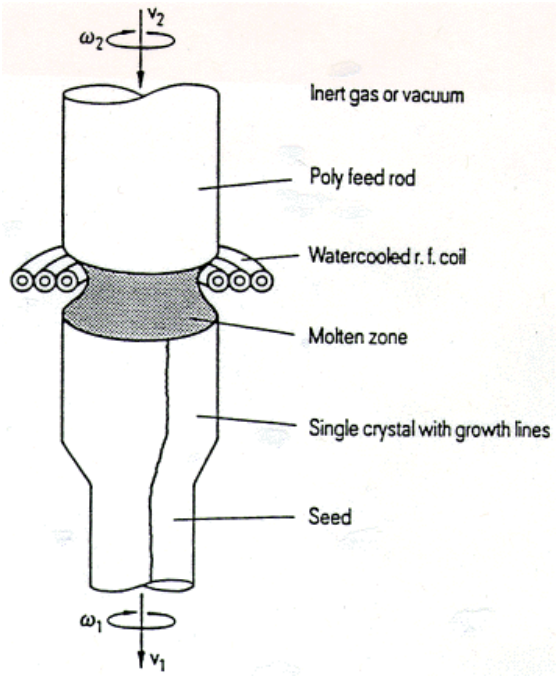

Figure 1.1: Principle of floating zone method [15]

But why is stirring of silicon melt necessary? One of the most important goals on the way of mc-Si production cost minimization is the reduction of the ingot's peripheral region, where carrier lifetime is significantly reduced in comparison with bulk silicon. This degraded region occurs because of the diffusion of impurities from the crucible and coating. The easiest way to reduce these impurities is decreasing the process time, that is, increasing the growth rate. But increased crystallization rate leads to concave bending of melting interface due to latent heat release and to enriching of diffusion boundary layer with impurities. Melt stirring can help to overcome both of these problems.

Another possibility for reducing degraded peripheral regions is the increase of ingot size, thus surface-to-volume ratio decreases. Currently, typical ingot size in industrial production is G5, generation 5 crucible. Number 5 points to the number

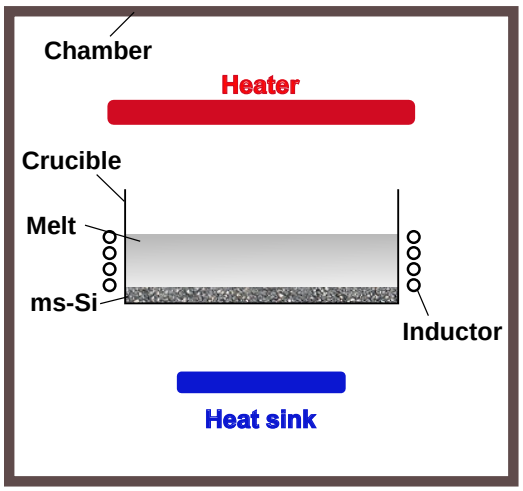

Figure 1.2: Schematic principle of directional solidification furnace

Figure 1.3: Crucible with grown polycrystalline silicon, cut in blocks

Atom	O	C	N	B	P	Fe
Segregation coefficient k	1.25	0.07	$7 \cdot 10^{-4}$	0.8	0.35	$8 \cdot 10^{-6}$

Table 1.1: Segregation coefficients for some atoms in silicon

of wafers (size 156 × 156 mm^2) obtained from ingot. Taking into account peripheral material losses, G5 crucible is typically 840 × 840 mm^2 [23].

DS method can also be used in the purification of the materials [24]. Purification phenomena is ensured by the small value of segregation coefficient, in other words, the solubility of the impurities in the melt is larger than in the solid. The last portions of solidified material contain most impurities, while other parts of solid are purified. The concentration of impurities in the solidified material is described by Scheil's equation

$$C_s = kC_0(1 - f_s)^{k-1}$$

where C_s is the impurity concentration in solid, f_s is fraction of solidified material (0 - all liquid, 1 - all solid), C_0 is initial concentration in liquid, and k is segregation coefficient. From this equation, it is clear that purification works only when segregation coefficient is small enough. Table 1.1 shows segregation coefficients for different atoms in silicon [25].

Investigation on the melt flow in silicon crystal growth methods is mostly limited to numerical research or similarity models using low melting temperature metals. The main limitation is high melting temperature of the silicon, which makes it impossible to use conventional flow measurement methods (see review in Section 3.1).

Several model experiments on Czochralski process are found in the literature. In the experiment with silicon oil as working liquid, the destabilization of the flow above the Richardson number, $Ri = 1$, is shown [26]. In similar experiments, the importance of Marangoni convection was shown [27]. In [28], liquid metal model experiments were carried out with the presence of rotating magnetic field, which might replace the crucible rotation in CZ crystal growth.

A number of investigations on flow in DS-type crucibles is found in literature. In model experiments, it is possible to satisfy the Reynolds number similarity criteria [29], but obtaining similar buoyancy force to inertial force ratio requires very high temperature gradients for downscaled models [30].

Numerical simulation tools are also widely used [31, 32] for calculation of concentration distribution, flow pattern, and solid-liquid interface shape. However, many aspects of turbulence are present in flows in DS process that are not analyzed. Assumption of isotropic turbulence is widely used without verification, but anisotropy is proven to be present in different flows, for example, MHD turbulence [33].

1.3 Objectives of the work

The research object of this thesis is electromagnetically forced liquid metal flow in square-shaped crucible with presence of vertical temperature gradient. Such flow class is of high importance for industry, in particular for photovoltaic silicon production using directional solidification method.

In this work, it will be proved that turbulence properties of temperature stratified EM force driven flow cannot be described by isotropic turbulence approach, and sharp transition in mean flow character exists in such flows near critical Richardson number.

The goals of this thesis are as follows:

- Make a theoretical analysis of two-dimensional flows in square-shaped crucible, derive flow parameter dependence on electromagnetic force distribution shape and amplitude, and compare results with works from literature.
- Investigate flow transition at intermediate Reynolds numbers using saltwater similarity model and find criteria for flow transition.
- Design and create experimental liquid metal model of directional solidification method with presence of vertical temperature gradient. Perform temperature and velocity measurements in liquid metal.

- Create numerical model of experimental setup. Validate flow simulations using experimental data.
- Analyze flow anisotropy, different flow regimes (isothermal and stratified), and turbulent heat transfer dependence on flow regime.

1.4 Outline

After the introduction, an overview on governing equations in described system will be given in Chapter 2. This includes basic description of electromagnetic laws, used simplifications and assumptions, as well as brief overview on fluid flow phenomena and turbulence description.

A literature review on measurement methods available for liquid metals will be given at the beginning of Chapter 3. The description of the experimental setup and used measurement methods will follow after that. The scaling of the present investigation results to industrial scales is discussed at the end of Chapter 3.

Chapter 4 is devoted to the simplified analysis of the flow in two dimensions, which corresponds to strongly stratified flow (no vertical velocity component). Velocity dependence on forcing parameters is obtained, and the results will be compared with numerical simulations. Same procedure is performed for 2D axisymmetrical case, where certain solutions are already known.

Simple salt-water similarity model is presented in Chapter 5, which allows using visual measurement technique – PIV. The discussion of vortex merging and transition between different flow regimes closes this chapter.

Chapter 6 shows results of UDV measurements in Wood's alloy with and without the presence of vertical temperature gradient. Temperature measurements are also performed. The transition between different flow regimes is discussed throughout this chapter.

Numerical results for present setup are shown in Chapter 7. At first, validation of results is shown. Afterward, flow structures are discussed for different regimes. The analysis of the anisotropy of flow reveals aspects previously untouched in context of directional solidification of silicon.

Chapter 8 gives example of numerical simulations for industrial furnace. Simulations show that intensive turbulent pulsations between main flow vortexes lead to wash-outs in seed crystal. It is shown that minimizing force near crucible bottom can prevent this effect.

Chapter 2

Governing Equations

2.1 Electromagnetic processes

Electric and magnetic fields are always present in the directional solidification devices – either they act only on the heating phenomena when resistive heaters are used or they influence melt flow, admixture distribution, and solidification front shape when AC inductors are used. The latter case is of high importance also for metallurgical applications because it offers an indirect (contactless) method for controlling the flow. At the same time, it also requires more sophisticated research methods and calculation algorithms, because of the coupled approach required for the mathematical description of such systems, where different physical phenomena act – electromagnetic, thermal processes and fluid dynamics of the melt.

Any electromagnetic process is described by Maxwell equations, which are simplified for the conditions used in technological applications. In the DS system description, the charge accumulation can be neglected since all conducting parts are usually grounded. The displacement currents can be neglected as well because of low frequencies used in such applications. In this frequency range (sub-GHz), conduction currents are of much higher importance. Both mentioned simplifications lead to the so-called quasi-stationary approximation:

$$\nabla \cdot \vec{E} = 0 \tag{2.1}$$

$$\nabla \cdot \vec{B} = 0 \tag{2.2}$$

$$\nabla \times \vec{E} = -\frac{\partial \vec{B}}{\partial t} \tag{2.3}$$

$$\nabla \times \vec{B} = -\mu_0 \vec{j} \tag{2.4}$$

Here, $\vec{E}$ is electric field intensity, $\vec{B}$ is magnetic flux density, $\vec{j}$ is current density, t is time, and μ_0 is magnetic permeability of free space. Combination with Ohm's law (equation 2.5) and insertion of equation 2.3 in 2.4 leads to the equation system that is usually solved to describe processes in MHD.

$$\vec{j} = \sigma \left[\vec{E} + \vec{u} \times \vec{B} \right] \tag{2.5}$$

$$\frac{\partial \vec{B}}{\partial t} = \nabla \times \left[\vec{u} \times \vec{B} \right] + \frac{1}{\mu_0 \sigma} \nabla^2 \vec{B} \tag{2.6}$$

$$\nabla \vec{j} = 0 \tag{2.7}$$

where σ is electrical conductivity, and $\vec{u}$ is local velocity of conducting media. Writing equation 2.6 in dimensionless form allows obtaining dimensionless number, which characterizes the importance of the advection term – magnetic Reynolds number, $Re_m = LU\mu_0\sigma$, where L and U are characteristic length and velocity, respectively. For $Re_m << 1$, the advection term is negligible, and equation 2.6 becomes form of a diffusion equation. The magnetic Reynolds number in laboratory and industrial scale applications is usually small.

For more convenient solution of equations 2.5-2.7, potentials are usually introduced – magnetic vector potential $\vec{A}$ and electric scalar potential ϕ that are defined as follows:

$$\vec{E} = -\nabla\phi - \frac{\partial \vec{A}}{\partial t} \tag{2.8}$$

$$\vec{B} = \nabla \times \vec{A} \tag{2.9}$$

For the solution of AC current systems, further simplifications are used. Since the source current can be written as $I = I_0 exp(\mathrm{i}\omega t)$, the magnetic field (and vector potential) can be expressed in the same way $B = B_0 exp(\mathrm{i}\omega t)$. $\omega = 2\pi f$ is angular frequency, where f is field oscillation frequency. Eq. 2.6 written for vector potential becomes the following form:

$$\mathrm{i}\omega \vec{A} = \vec{u} \times \nabla \times \vec{A} + \frac{1}{\mu_0 \sigma} \nabla^2 \vec{A} \tag{2.10}$$

For the uniform external magnetic field in an infinite conductor half–space, complex magnetic field distribution is expressed as follows:

$$B = B_0 exp\left[-\frac{x}{\delta}\right]\left[cos\frac{x}{\delta} - \mathrm{i}sin\frac{x}{\delta}\right]$$

$$\delta = \sqrt{\frac{1}{\sigma\mu\pi f}} \tag{2.11}$$

Eq. 2.11 describes the skin layer depth for magnetic field – the distance in which magnetic field decays e times.

In resource-demanding numerical simulations where the most finite elements are within nonconducting domains (air, insulator), the number of variables can be decreased by using $\vec{T} - \Omega$ formulation with vector electric potential $\vec{T}$ and magnetic scalar potential Ω .

$$\vec{j} = \nabla \times \vec{T}$$

$$\vec{H} = \vec{T} - \nabla\Omega$$

Here H is magnetic field intensity. Using 2.2 and 2.3, the following equations are obtained, which are numerically solved:

$$\frac{1}{\sigma}\nabla \times \nabla \times \vec{T} + \mathrm{i}\omega\mu_0\left(\vec{T} - \nabla\Omega\right) = 0$$

$$\nabla \cdot \left(\vec{T} - \nabla\Omega\right) = 0$$

Any conducting body in the EM field experiences a force that depends on the magnetic field intensity. The volumetric density of such force is:

$$\vec{f} = \vec{j} \times \vec{B} \tag{2.12}$$

By using equation 2.4, this force can be written as

$$\vec{f} = \frac{1}{\mu_0}\left[\vec{B}\nabla\right]\vec{B} - \nabla\left[\frac{B^2}{2\mu_0}\right] \tag{2.13}$$

In 2.13, the second term is gradient of a scalar; therefore, it is potential force and does not impact the flow motion. The first term is rotational ($\nabla \times \vec{f} \neq 0$), and it acts on the fluid as volumetric force, thus creating motion.

Additionally to the volumetric force, induced currents generate heat in the melt that is also able to influence the fluid motion by creating a nonuniform temperature distribution. The induced Joule heat is expressed as:

$$Q = \frac{\vec{j}^2}{\sigma}$$

In time-harmonic analysis, Lorentz force density and Joule heat density can be calculated by time averaging over one period of electromagnetic field oscillation.

$$\vec{f} = \frac{1}{2} Re\left[\vec{j}_0^* \times \vec{B}_0\right] = \frac{1}{2}\left[\vec{j}_{Re,0} \times \vec{B}_{Re,0} + \vec{j}_{Im,0} \times \vec{B}_{Im,0}\right]$$

$$Q = \frac{\vec{j}_0^2}{2\sigma} = \frac{\vec{j}_{Re,0}^2 + \vec{j}_{Im,0}^2}{2\sigma}$$

Here subscript 0 represents complex amplitude, and symbol * in superscript represents complex conjugate. Time dependence of force density, which oscillated with twice of the EM field frequency, can be neglected because liquid metals do not react to variations with frequency above 4 Hz [34].

The skin depth of the electromagnetic field is not the universal parameter for the characterization of the EM field impact depth. The relation of δ with size of the domain is also significant. For this purpose, dimensionless frequency $\tilde{\omega}$ is introduced as follows [35]:

$$\tilde{\omega} = \omega \mu_0 \sigma L^2 = 2\left(\frac{L}{\delta}\right)^2$$

In literature, the dimensionless frequency is also widely called as shielding parameter or shielding factor.

2.2 Fluid flow equations

The motion of an incompressible liquid is governed by the Navier-Stokes equations, which are momentum conservation laws written for fluid element (Eq. 2.14). The additional information necessary to describe flow, is the conservation of mass (Eq. 2.15), expressed by equation of continuity.

$$\frac{\partial \vec{u}}{\partial t} + (\vec{u} \cdot \nabla)\,\vec{u} = -\frac{\nabla p}{\rho} + \nu \nabla^2 \vec{u} - \vec{g}\beta(T - T_0) + \frac{\vec{f}(\vec{r}, t)}{\rho} \tag{2.14}$$

$$\nabla \cdot \vec{u} = 0 \tag{2.15}$$

Here, ρ is density, ν is kinematic viscosity, β is thermal expansion coefficient, $\vec{g}$ is free-fall acceleration, p is pressure, and T is temperature. The equation in this form (Eq. 2.14) already includes Boussinesq approximation for buoyancy force. This is true for a small density deviation condition, which is usually fulfilled in the liquid metal applications.

The scalability of the flow phenomena and applicability to different scales or materials is judged by comparing a dimensionless numbers. For this purpose, dimensionless variables are introduced. Velocity $u^* = u/U$, spatial dimension $x^* = x/L$, time $t^* = tU/L$, pressure $p^* = p/(U^2\rho)$, and temperature $\theta = \frac{T-T_B}{T_T-T_B}$.

$$\frac{\partial \vec{u^*}}{\partial t^*} + \left(\vec{u^*} \cdot \nabla\right) \vec{u^*} = -\nabla p^* + \frac{1}{Re}\nabla^2 \vec{u^*} - \frac{Gr}{Re^2}\theta \vec{z} + \frac{F_{em}}{Re^2}\vec{f^*} \tag{2.16}$$

Three dimensionless numbers are obtained here: Reynolds number Re, Grashoff number Gr, and magnetic interaction parameter F_{EM}.

$$Re = \frac{UL}{\nu} \tag{2.17}$$

$$Gr = \frac{g\beta(T_T - T_B)L^3}{\nu^2} \tag{2.18}$$

$$F_{EM} = F_{max}\frac{L^3}{\rho\nu^2} \tag{2.19}$$

Here, U is characteristic velocity, L is length scale, $T_T - T_B$ is typical temperature difference, and F_{max} is maximal EM force density.

In the direct solidification devices, melt is kept under a vertical temperature gradient with warmer (T_T) fluid (smaller density) on the top and colder fluid on the bottom (T_B). At strong temperature gradients, this can lead to stratified flow, where the buoyancy force decays any vertical motion. As stratified flows are well known in geophysics and atmosphere physics, some accomplishments can be transferred from investigations in this field.

For stratified flows, Richardson number is often used, as it characterizes the ratio of buoyancy forces to the inertial forces.

$$Ri = \frac{Gr}{Re^2} = \frac{\beta \Delta T g L}{U^2} = \frac{N^2}{\left({}^{U}/_{L}\right)^2} \tag{2.20}$$

$$N = \sqrt{-\frac{g}{\rho_0}\frac{d\rho}{dz}} \approx \sqrt{\frac{g\beta\Delta T}{L}} \tag{2.21}$$

Brunt-Väisälä frequency N characterizes the level of stratification. Its physical interpretation can be understood in simple example. If a fluid element is vertically displaced, say upward, in the stably stratified fluid, buoyancy forces will push it downward to its initial vertical level because the density of fluid element is lower than the density of the surrounding fluid. Assuming this process to be adiabatic and neglecting viscous dissipation, the fluid element will pass it's zero level and keep moving downward because of inertia, while buoyancy forces will decelerate the fluid element because its density is now lower than the density of the surrounding fluid. Such oscillations of fluid element continue further on with frequency N, unless any damping forces exist.

For the complete description of the phenomena in the melt during directional solidification process, energy balance equation needs to be added to the equation system.

$$c\rho\left(\frac{\partial T}{\partial t} + \vec{v}\cdot\nabla T\right) = \nabla\left[\lambda\nabla T\right] + Q \tag{2.22}$$

Here λ is heat conductivity; Q is heat source, Joule heat density in particular; and c is specific heat capacity. Radiation heat transfer is neglected here (although it is present in DS systems but not inside the melt – the melt is assumed to be opaque). Corresponding dimensionless equation can be obtained by using the same substitutions described previously.

$$\frac{\partial\theta}{\partial t^*} + \vec{v^*}\cdot\nabla\theta = \frac{1}{Pe}\nabla^2\theta + \frac{LQ_{max}}{U\Delta Tc\rho}Q^* \tag{2.23}$$

Here Q_{max} is maximal Joule heat density in the volume. Peclet number Pe characterizes the ratio between convective heat transfer governed by fluid motion with velocity U and molecular heat transfer with thermal diffusivity $\alpha = \lambda/\rho c$.

$$Pe = \frac{LU}{\alpha} = \frac{LU\rho c}{\lambda} \tag{2.24}$$

Rayleigh number is often considered as criteria for flow regimes in buoyancy-driven flows. Rayleigh number is a ratio between buoyancy and viscous forces in the liquid and is defined as $Ra = GrPr$, where Pr is Prandtl number.

$$Pr = \frac{\nu}{\alpha}$$

2.3 Turbulence description in stratified flow

2.3.1 Necessity of turbulence modeling

In the flow with $Re < 1$, the inertial term of the Navier-Stokes equation becomes significantly smaller than the viscous term. Such flow is called Stokes flow or creeping flow. Stokes flow appears in the case of a large viscosity (e.g. glass-melt flow) or small dimension of the flow (e.g., biological microelectromechanical systems – bio-MEMS).

On the other hand, when $Re > 10^3$, the flow is highly unstable, irregular, with strong variation of velocity, pressure, and temperature in the time and space. Critical Reynolds number Re_C is assumed criteria for the transition between laminar and turbulent regime; for example, for the flow in pipe, critical value is $Re_C = 2000$, but this value is not strict and can be different for each observed flow.

Although laminar flow characteristics can be calculated easily and computation powers nowadays are capable to solve these problems, it is rarely necessary in practice. To solve the Navier-Stokes equations for the turbulent flow, spatial and time discretization must resolve all flow structures larger than Kolmogorov scales (smallest scales present in the flow). Even with the most up-to-date computers, solving this problem for standard technical application in reasonable time is a challenging task, even for relatively small Reynolds numbers. The number of spatial nodes required for Direct Numerical Simulation (DNS) can be evaluated as [36]

$$N^3 \sim Re^{9/4} = Re^{2.25}$$

So even at the flow with Re=10,000, the number of finite volume cells in mesh is approximately one billion. These requirements are reviewed in [37], where relation $N^3 \sim Re^{37/14} \approx Re^{2.64}$ is derived. Nowadays, some very ambitious projects can handle flows at even higher Reynolds numbers, in [38] DNS with 242 billion degrees of freedom performed on 767k cores. However, such calculations usually have fundamental character. DNS in engineering is rare.

2.3.2 Reynolds averaging

Instead of resolving all the time and space scales of the flow, one can use statistical relations to reduce the number of degrees of freedom. An approach was suggested by Reynolds, where flow is described by its mean characteristic values and their deviation from the mean.

$$a = \bar{a} + a'$$

where a is variable of flow (pressure, velocity component, or temperature). $\bar{a}$ denotes time-averaged value, and a' is deviation from mean. This approach does not resolve small amplitude and short-period fluctuations but describes them as deviation from averaged mean value. The mean value of deviations is zero – $\bar{a'} = 0$.

Other properties of averaging operation have to be recalled [39].

$$\bar{\bar{a}} = \bar{a}; \qquad \overline{a + b} = \bar{a} + \bar{b}; \qquad \overline{a\bar{b}} = \bar{a}\bar{b}$$

Another important property arises from all mentioned.

$$\overline{(\bar{a} + a')(\bar{b} + b')} = \bar{a}\bar{b} + \overline{a'b'}$$

Averaging of the Navier-Stokes equations 2.14 in this way leads to the Reynolds Averaged Navier-Stokes equations (RANS).

$$\bar{u_i}\frac{\partial \bar{u_i}}{\partial x_j} = \frac{\partial}{\partial x_j}\left[-\frac{\bar{p}}{\rho}\delta_{ij} + \nu\left(\frac{\partial \bar{u_i}}{\partial x_j} + \frac{\partial \bar{u_j}}{\partial x_i}\right) - \overline{u_i' u_j'}\right] - \vec{g}\beta(\bar{T} - T_0) + \frac{\vec{f}}{\rho} \tag{2.25}$$

The term $\overline{u_i' u_j'}$ here is a new unknown, which leads to the equation system closure problem. The correlation $\tau_{ij} = \rho\overline{u_i' u_j'}$ is called Reynolds stress tensor. The equation for correlation contains third-order statistical moments, third-order moment equation contains fourth-order moments, etc. Therefore, the number of unknowns is always larger than the number of equations, and this approach always results in an unclosed equation system.

Well-known approach used to tackle this problem is the Boussinesq hypothesis, which defines an assumed linear relation between Reynolds stress tensor and mean velocity deformation tensor.

$$\frac{\tau_{ij}}{\rho} = \nu_t\left(\frac{\partial \bar{u_i}}{\partial x_j} + \frac{\partial \bar{u_j}}{\partial x_i}\right) - \frac{2}{3}k\delta_{ij} \tag{2.26}$$

Here, ν_t is turbulent viscosity, which is a property of the flow, unlike the molecular viscosity, which is the property of matter, and $k = 0.5\overline{u_i' u_i'}$ is turbulence kinetic energy.

Surely, Boussinesq formula does not solve the closure problem, because it leads to the new unknown ν_t, but it defines an approach, which allows to model Reynolds stress tensor with a help of turbulent viscosity. Since 70s of the last century, many turbulence models with different level of complexity are developed for numerical applications [40]. Most of them are based on empirical approach, where model coefficients are adjusted to obtain best agreement with an experimental data for certain flow types. Such models solve closure problem and allow obtaining solution with currently available computer power in a reasonable time.

One of most universal turbulence models in terms of its applicability to engineering problems is Shear Stress Transport ($k - \omega$-SST) model [41]. It combines properties of two popular models: $k - \epsilon$ and $k - \omega$. In this model two additional transport differential equations for turbulence kinetic energy k and specific dissipation rate ω_d are solved:

$$\frac{Dk}{Dt} = P_k - \beta^* \omega_d k + \frac{\partial}{\partial x_j}\left[(\nu + \sigma_k \nu_t)\frac{\partial k}{\partial x_j}\right]$$

$$\frac{D\omega_d}{Dt} = \frac{\gamma}{\nu_t} P_k - \beta \omega_d^2 + \frac{\partial}{\partial x_j}\left[(\nu + \sigma_\omega \nu_T)\frac{\partial \omega_d}{\partial x_j}\right] + 2(1 - F_1)\frac{\sigma_{\omega 2}}{\omega_d}\frac{\partial k}{\partial x_j}\frac{\partial \omega_d}{\partial x_j}$$

D/Dt here is convective derivative, P_k is generation of turbulence kinetic energy. Meaning and numerical values of other variables and constants from this model are discussed in [41]. In engineering applications, $k - \omega$-SST shows better performance than standard $k - \epsilon$ and $k - \omega$ models in wide range of problems [42, 43].

2.4 Large eddy simulation

Large eddy simulation (LES) approach is based on filtering of Navier-Stokes equations, and described quantities (e.g. velocity) are separated into filtered $\bar{a}_i$ and subgrid scale components $\widetilde{a}_i$.

$$a_i = \bar{a}_i + \widetilde{a}_i$$

Filtering operation is defined as follows:

$$\bar{a}_i(\vec{x}) = \int G(\vec{x} - \vec{\xi}) a_i(\vec{\xi}) d\vec{\xi}$$

Integration takes place in the whole domain of described flow. $G(\vec{x}-\vec{\xi})$ here is a filter function, which is dependent on finite volume mesh used in calculations. G is even function, which satisfies normalization condition.

$$\int G(\vec{x}-\vec{\xi})d\vec{\xi} = 1$$

Most often used are box, Gaussian, and Fourier filters [44]. After performing filtering operation, filtered Navier-Stokes equation can be obtained.

$$\rho\left[\frac{\partial \bar{u}_i}{\partial t} + \frac{\partial \bar{u}_i\bar{u}_j}{\partial x_j}\right] = \frac{\partial}{\partial x_j}\left[\eta\left(\frac{\partial \bar{u}_i}{\partial x_j} + \frac{\partial \bar{u}_j}{\partial x_i}\right) - \bar{p}\delta_{ij} + \rho T_{ij}\right] + f_i$$

where $T_{ij} = \overline{u_i u_j} - \bar{u}_i\bar{u}_j$ sub-grid stress tensor.

Similarly as in RANS case, equation system can be closed with assumption, that stress tensor T_{ij} is proportional to the deformation tensor of filtered velocity:

$$T_{ij} = 2\nu_{SGS}\bar{S}_{ij} + \frac{\delta_{ij}T_{ij}}{3} = \nu_{SGS}\left(\frac{\partial \bar{u}_i}{\partial x_j} + \frac{\partial \bar{u}_j}{\partial x_i}\right) + \frac{\delta_{ij}T_{ij}}{3}$$

where ν_{SGS} is sub-grid viscosity. To close equation system, assumptions about ν_{SGS} are made. The models that are based on such approach are called sub-grid viscosity models. One of the most popular models in this group is Smagorinsky model [45].

$$\nu_{SGS} = (C_s\Delta)^2\sqrt{2\bar{S}_{ij}\bar{S}_{ij}}$$

where Δ is mesh element size, and C_s is Smagorinsky constant with typical range $C_s = 1.4...1.5$.

2.4.1 Locally isotropic turbulence

In 1941, Kolmogorov proposed a hypothesis, which stated that large vortexes in turbulent flows are unique and individual for each flow. They are defined by domain geometry and the character of dominating flow.

These large vortexes split into smaller ones, and this process continues until such small eddies are reached, which can be dissipated by the viscosity. This process is called cascade energy transfer. Small eddies are, however, universal for all flows, because they are defined by the viscosity, and therefore, in these scales (small eddies), turbulence is unique for all flows in all directions (isotropic and homogeneous turbulence).

To quantify this description, various scales are introduced. The largest eddies existent in the flow have size l_0 (integral length scale), and they are comparable

with the characteristic size of the flow domain L. Their characteristic velocities are $u' = \sqrt{2k/3}$.

In the small eddies, dissipation suppresses energy transfer, therefore they are characterized by other variables than used in energy-containing scales. One of them is turbulent eddy dissipation rate ϵ. From dimensional analysis, one can get [39]:

$$\epsilon \sim \frac{u'^3}{l}$$

The size of the small vortexes can be estimated in the same way by using dissipation and viscosity. From these quantities, Kolmogorov lengh scale l_K can be combined.

$$l_K \sim \left(\frac{\nu^3}{\epsilon}\right)^{1/4}$$

Kolmogorov timescale in similar manner is defined as

$$\tau_K \sim \left(\frac{\nu}{\epsilon}\right)^{1/2}$$

Kolmogorov-scale Reynolds number ($Re_K = l_K v_k/\nu$) of the smallest eddies is 1, and this fact corresponds to the significant viscous dissipation in Kolmogorov scale eddies.

For intermediate scales, the following Kolmogorov's hypothesis is stated: *in every turbulent flow at sufficiently high Reynolds number, the statistics of the motions of scale l in the range $l_0 >> l >> l_K$ have a universal form that is uniquely determined by ϵ independent of ν* [44].

The motions of length scale l correspond to the wave number $\kappa = 2\pi/\lambda_w$ (λ_w is wavelength). In the spectral space, small wave number domain is called energetic region, while the cascade energy transport takes place in the inertial region $2\pi/L < \kappa < 2\pi/l_K$. Energy spectral density in inertial region follows from Kolmogorov's second hypothesis of similarity [46].

$$E(\kappa) = C_K \epsilon^{2/3} \epsilon^{-5/3}$$

Here, $C_K = 1.5$ is Kolmogorov constant [47]. $E(\kappa)$ is the energy spectral density; in other words, it shows how much energy contain vortexes with the wave number κ. The integral of energy spectral density over whole wave number space characterizes turbulence kinetic energy k.

$$k = \int_0^\infty E(\kappa) d\kappa$$

The Kolmogorov's hypotheses have no direct connection with Navier-Stokes equations. In 1930s, this drawback was resolved by approach based on two-point correlations [48], [49].

$$R_{ij}(\vec{\xi}, t) = \frac{\overline{u_i'(\vec{r}, t) u_j'(\vec{r} + \vec{\xi}, t)}}{\sqrt{u_i'(\vec{r}, t)^2 u_j'(\vec{r} + \vec{\xi}, t)^2}} = \frac{r_{ij}(\vec{\xi}, t)}{\sqrt{u_i'(\vec{r}, t)^2 u_j'(\vec{r} + \vec{\xi}, t)^2}} \tag{2.27}$$

In homogeneous turbulence, the correlation coefficient is not dependent on $\vec{\xi}$. Correlation allows obtaining one-dimensional energy spectrum.

$$E_{ij}(\kappa_1) = \frac{1}{2\pi} \int_{-\infty}^{\infty} r_{ij}(\vec{\xi}, t) \exp \mathrm{i}\kappa r_1 dr_1 \tag{2.28}$$

However, in practice, obtaining spatial two-point correlation is challenging because of the necessity of two simultaneous measurements at different locations; furthermore, measurements have to be repeated with different distances between measurement points $\vec{\xi}$. As shown by Taylor [50], measurements from one single point can also be used to obtain turbulence spectral properties. For this purpose, an autocorrelation function is used:

$$R_{ii}(\tau) = \frac{\overline{u_i'(t) u_i'(t + \tau)}}{u_i'(t)^2} = \frac{r_{ii}(\tau)}{u_i'(t)^2} \tag{2.29}$$

Power spectrum can be obtained by taking Fourier transform of the autocorrelation function:

$$F_{ii}(\omega) = \int_{-\infty}^{\infty} r_{ii}(\tau) \exp \mathrm{i}\omega\tau d\tau \tag{2.30}$$

According to Taylor's frozen turbulence hypothesis, one can write,

$$E_{ii}(\kappa) = \frac{\bar{u}}{2\pi} F_{ii}(\omega); \qquad \kappa = \frac{\omega}{\bar{u}} \tag{2.31}$$

An intermediate scale between integral and Kolmogorov scales, the Taylor length scale λ_T, is important in the characterization of turbulence intensity. It is often referred as turbulence length scale. If the spatial two-point correlation function is known, λ_T can be calculated as follows:

$$\lambda_T^i = \frac{1}{\sqrt{-0.5 R_{ii}''(0, t)}} \tag{2.32}$$

Here, prime indicates derivative over distance ξ. By introducing Eulerian timescale $\tau_E^i = \lambda^i / \bar{u_i'}$, the autocorrelation can be used to estimate microscales:

$$\tau_E^i = \frac{1}{\sqrt{-0.5 R_{ii}''(0)}} \tag{2.33}$$

2.4.2 Stratified flow

Ozmidov [51] assumed that some length scale l_O exists in the stratified flow, above which all eddies have only vertical vorticity vector. Corresponding velocity scale is $(\epsilon l_O)^{1/3}$. For critical Richardson number Ri_{CR}, one can write:

$$Ri_{CR} = \frac{N^2 l_O^2}{(\epsilon l_O)^{2/3}}$$

Assuming that $Ri_{CR} = 1$, Ozmidov length scale can be obtained as follows:

$$l_O = \sqrt{\frac{\epsilon}{N^3}}$$

At Ozmidov length scale, which is sometimes referred as Dougherty-Ozmidov scale, a balance exists between the buoyancy and inertial effects. Important ratio between integral l_0 and Ozmidov length scale l_O can be expressed by means of Richardson number.

$$\frac{l_0}{l_O} = \left(\frac{N u'^2}{\epsilon} \right)^{3/2} = Ri^{3/4}$$

This ratio shows that stratification takes place when $l_O << l_0$, and it is negligible at $l_O >> l_0$. It is also clear that in bounded flows, no turbulence scales can form that exceeds integral scale.

2.4.3 Characterization of anisotropy

Anisotropy of flow is characterized by anisotropy coefficients, which are 1.0 in the isotropic turbulence.

$$K_{ijkl} = C \frac{\left\langle \left(\frac{\partial u_i}{\partial x_j} \right)^2 \right\rangle}{\left\langle \left(\frac{\partial u_k}{\partial x_l} \right)^2 \right\rangle}$$

Angle brackets here indicate volume averaging. Coeffiecient C is 0.5, 1.0, or 2.0, depending on which components of velocity and derivative are used. The choice is based on the properties of the isotropic turbulence [52]:

$$\left\langle \left(\frac{\partial u_x}{\partial x}\right)^2 \right\rangle = \left\langle \left(\frac{\partial u_y}{\partial y}\right)^2 \right\rangle = \left\langle \left(\frac{\partial u_z}{\partial z}\right)^2 \right\rangle = \frac{1}{2}\left\langle \left(\frac{\partial u_i}{\partial x_j}\right)^2 \right\rangle, i \neq j$$

The anisotropy of the energy-containing scales can also be characterized by the use of traceless anisotropy tensor defined by [53]

$$b_{i,j} = \frac{\langle u_i' u_j' \rangle}{\langle u_k' u_k' \rangle} - \frac{1}{3}\delta_{ij} \tag{2.34}$$

It has two invariants – $II = b_{ij}b_{ji}$ and $III = b_{ij}b_{jk}b_{ki}$. II is positively defined, and its value represents degree of anisotropy. Sign of III points to the nature of anisotropy – at positive III, flow tends to be “prolate” or “rod-like” (with one component dominating), while at negative III, flow is “oblate” or “disk-like” with two components dominating.

Chapter 3

Experimental Facility and Measurement Systems

This chapter is devoted to the description of measurement techniques used further in this work (Chapters 5 and 6), and setup of experimental model (Chapter 6). Scaling of results obtained in experimental model to industrial silicon growth equipment is also discussed in this chapter.

3.1 Measurement methods

Velocity measurements in liquid metals are relatively rare because of their complexity - aggressive media and high temperatures limit applicable technology range. Furthermore, metals are opaque; therefore, visual evaluation methods (photography of tracers) and methods connected with the use of laser cannot be used. For these reasons, numerical simulations are the most powerful tools for the investigation of heat and mass exchange processes in the systems with molten silicon, as well as other materials that are molten at the temperatures well above 700° C.

Another way to investigate such systems is experimental modeling, using model liquid with properties similar to the material of interest. Such models are often used in different branches of metallurgy and even glass melting industry. Model liquids are usually eutectic alloys that have low melting point (lead-bismuth and other alloys with Pb and Bi content) or are liquid even at room temperature (gallium, gallium-indium-tin). For modeling of glass properties, a glycerin-sulfuric acid-water mixture can be used [54], which is transparent and allows usage of visual techniques like particle image velocimetry (PIV). In model liquids, it is easier to perform measurements because they do not react chemically with probes, are less dangerous for human (experimentalist), and their working temperature is strictly below the critical temperature for

sensor materials (e.g., depolarization of piezoelectric materials at Curie temperature [55]). However, because of opaqueness, most of the methods applied for liquid metals are intrusive (sensor is introduced in flow). Wide range of applications for intrusive sensors can be explained with comparably low costs and relative simplicity of technology. Intrusive methods used in liquid metals can be classified in mechanical, thermal, and electromagnetic methods. Almost all of them are also used in water and gases.

To determine the local pressure in liquid metal, Pitot tubes can be used, which allow determining local velocity value by means of Bernulli formula. Maximal time resolution in this method is limited, because pressure leveling in tubes complies with significant inertia. However, measurements with frequency that exceeds 1kHz are obtained by using piezoelectric pressure transducer [56]. Optical fiber velocity sensors should also be added to mechanical sensors. They measure deformation of fiber introduced in flow by means of light intensity variation measurement.

The most widely used thermal velocity sensors are hot films and hot wires. Sensor is heated to some temperature above the ambient, but flow is removing heat from it. A correlation exists between flow velocity and temperature of the sensor. Using a specific electric conductivity of sensor material dependence on temperature, and calibration curve as well, local flow velocity can be obtained. In this method, data is obtained in local points; furthermore, finite dimensions of sensor are limiting spatial resolution. But high temporal resolution is inherent to this method, which is important for turbulence research.

The amount of heat removed by convective heat transfer is influencing measurements significantly. Even more important this is in liquid metals, where Prandtl number is small ($\sim 10^{-2}$). It means a situation when heat removal from sensor surface is determined mainly by molecular heat conductivity and not convective heat transfer. Because of high temporal resolution, thermal sensors are widely used in the investigation of turbulent flows in water and gases. Measurements in liquid metals are more seldom because of high molecular conductivity. In metals (e.g., mercury) and alloys (e.g., Wood's metal) with low melting temperature (70 ℃), several experimental measurements are known [57], although measurements at higher temperatures (250 ℃) are also found in literature, for example, liquid sodium [58]. Though most of these works are done in 80s of last century, in further period, the amount of research projects in this field is decreased.

Potential difference probe (PDP) is the most widely used electromagnetic flow sensor. This method is based on measurement of potential difference on electrodes $\Delta\phi$, that are in distance Δl from each other. Using Ohm's law for movement of

electric conductor in magnetic field, and knowing magnetic flux density, velocity value in spatial point can be obtained [59]. Since magnetic field with known flux density in measurement point is needed, it has to be applied externally - either globally for all domain or locally in measurement point by incorporating permanent magnet in the sensor. Usability range is limited from above by Curie temperature of the magnets; therefore, electromagnets are used at high temperatures, for example, in aluminum melt [60] and [61] in liquid zink at 700 ℃. Two velocity components can be obtained with this method, with typical time resolution $\sim$ 50 Hz [62, 63]. But as a drawback for this method to mention relatively large sensor dimensions (several millimeters), which influences the flow and leads to low spatial resolution, obtained signal have to be interpreted as averaged value over volume with characteristic sensor dimension. The reduction of sensor dimension is limited, because it leads also to reduction of sensor sensitivity. In [64], it was shown that it is, however, not the sensitivity that limits the small velocity measurements but the nonlinear response due to magnetic breaking effect. In this work, the wires on the probe were 1 mm apart, and the magnetic field intensity was 30 mT <B <70 mT, velocities down to fractions of millimeters per second.

A number of nonintrusive velocity measurement methods exist, which are used in liquid metals, water, and gases. The development of ultrasound doppler velocimetry (UDV) is substantially influenced by Takeda [65], and it became possible to perform measurements in metals. The restrictions of this method are associated with maximal working temperature of piezoelectric transducers. Nevertheless, latest works on development of this technique ensure measurements in media with temperature up to 800 ℃. UDV was already applied in CuSn melt at 620 ℃ [66] by using waveguides. The improvement of waveguide technique might make it possible to reach even higher possible temperatures for UDV measurements. The main advantage of this technique is a possibility of obtaining full velocity profile along certain path. The use of ultrasound probe arrays allows obtaining velocity distribution in one full cross section [67] or even full volume.

Besides restrictions, which are associated with the characteristics of media (aggressiveness, high temperatures), in metals, there are also factors, which expand the range of applicable measurement technologies. Metals usually are good electrical conductors, thus magnetic Reynolds number can be large enough for flow-induced magnetic field to be sufficient for registration and determination of the flow velocity.

Contactless induced flow tomography is a relatively new method, which allows determining the flow velocity in conductive liquid by means of flow-induced magnetic

field measurement. For this reason, external magnetic field is applied with known distribution in measurement domain, therefore, currents appear ($\vec{j} = \sigma\vec{u} \times \vec{B}$), which generate secondary magnetic field. The main advantage of this method is contactless measurement, which gives 3D velocity field, but spatial and temporal resolution of obtained data is relatively low ($\Delta t = 6$ seconds, $\Delta x = 4$ cm in [68]), which makes it insufficient for understanding fine flow structures and investigating turbulence characteristics.

3.2 Ultrasound Doppler velocimetry

3.2.1 Basic principles

The instantaneous measurement of velocity in multiple points is a benefit of methods like PIV, LIF, and UDV. But as stressed already in pioneer work of Takeda (1986) [69], UDV has advantage of it's applicability in opaque liquids. Since the late 80s, this technique is well developed and produced commercially. In this work, commercial measurement unit DOP3010 from *Signal Processing SA* was used.

The Doppler effect is the shifting of the frequency that occurs when an observer is moving relative to a source of sound (generally speaking, Doppler effect takes place also in electromagnetic waves, but in this work, the discussion will be limited to sound waves only). This principle is used in different measurement techniques, for example, Doppler radars that measure the speed of moving cars on the highways or equipment for medical examination of blood flow in different sections of cardiovascular system.

If in a moving liquid there exist some particles that reflect the ultrasound, the speed of the particle can be obtained by sending ultrasound signal and then measuring the frequency shift of the reflected signal. This is the basic principle of the continuous ultrasound Doppler velocimetry. However, this is never the case in pulsed ultrasonic Doppler velocimetry.

The distance of the particle from the ultrasonic probe can be found easily as $l = ct_d/2$, where c is speed of sound, and t_d is time delay between sent and received ultrasonic signal [70]. The velocity of the particle along the ultrasonic beam $v^{\parallel} = v\cos\theta$ can then be found from the difference between two positions $\Delta l = l_2 - l_1$ separated by the time $\Delta t = t_2 - t_1$ (see Figure 3.1). In this time the particle will travel the distance Δd, but only the disposition component $\Delta l = \Delta d \cos\theta$ can be measured using the ultrasonic beam. The time difference between pulses ΔT is always very short and therefore is replaced by the phase shift between two received echoes

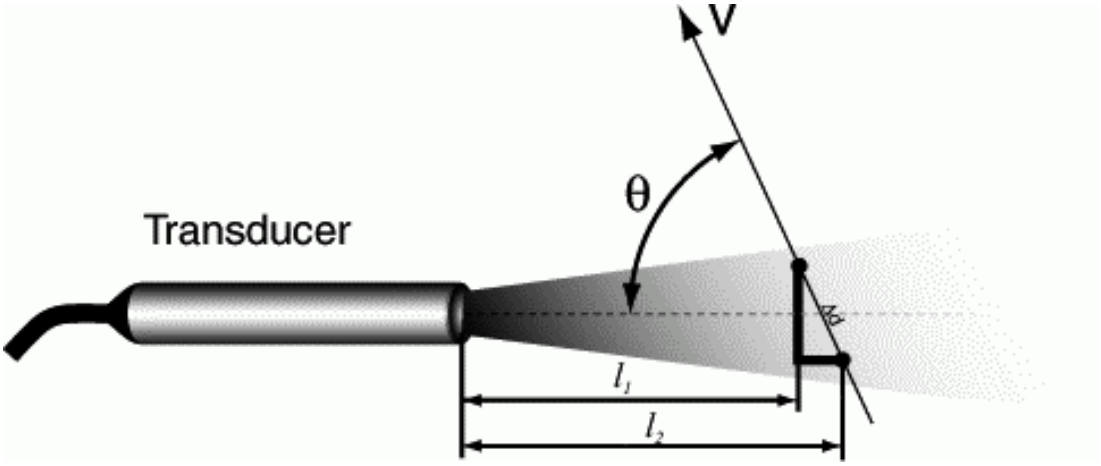

Figure 3.1: Principal sketch of pulsed UDV [70]

$\delta = 2\pi f_e \Delta t$, where f_e is emitted ultrasound frequency. The velocity information is then obtained by the following expression [71]:

$$v^{\parallel} = \frac{c\delta}{4\pi f_e T_{PRF}} = \frac{c f_d}{2 f_e} \tag{3.1}$$

$f_{PRF} = 1/T_{PRF}$ is the pulse repetition frequency (PRF), f_d - Doppler frequency. The formula for continuous Doppler velocimetry, where Doppler frequency is measured, is identical to the equation 3.1 for pulsed UDV, where the shift in echo signals is measured, although in the pulsed method, Doppler effect plays a minor role.

The shown description is valid for one particle, but in the reality, there are always many particles, randomly distributed in the sampling volume. Practice shows that there exists high degree of correlation between two consecutive echoes; therefore, these equations are valid for the real flows.

The drawback of the pulsed UDV is the limited maximal depth, which is connected with the time needed by the sound to travel from the emitter to the measurement volume and back. The maximal measurement depth is $l_{max} = cT_{PRF}/2$.

Another limitation of pulsed UDV is the maximal velocity due to aliasing effect. According to Nyquist-Shannon sampling theorem, the Doppler frequency f_d is limited by the relation $max(f_d) < f_{PRF}/2$. Using the equation 3.1, the maximal velocity can be expressed by:

$$v^{\parallel}_{max} = \frac{c}{4 f_e T_{PRF}}$$

Pulse repetition frequency is an essential parameter that influences both $v^{\parallel}_{max}$ and l_{max}. The increase of T_{PRF} will increase the maximal measurement depth, but reduce

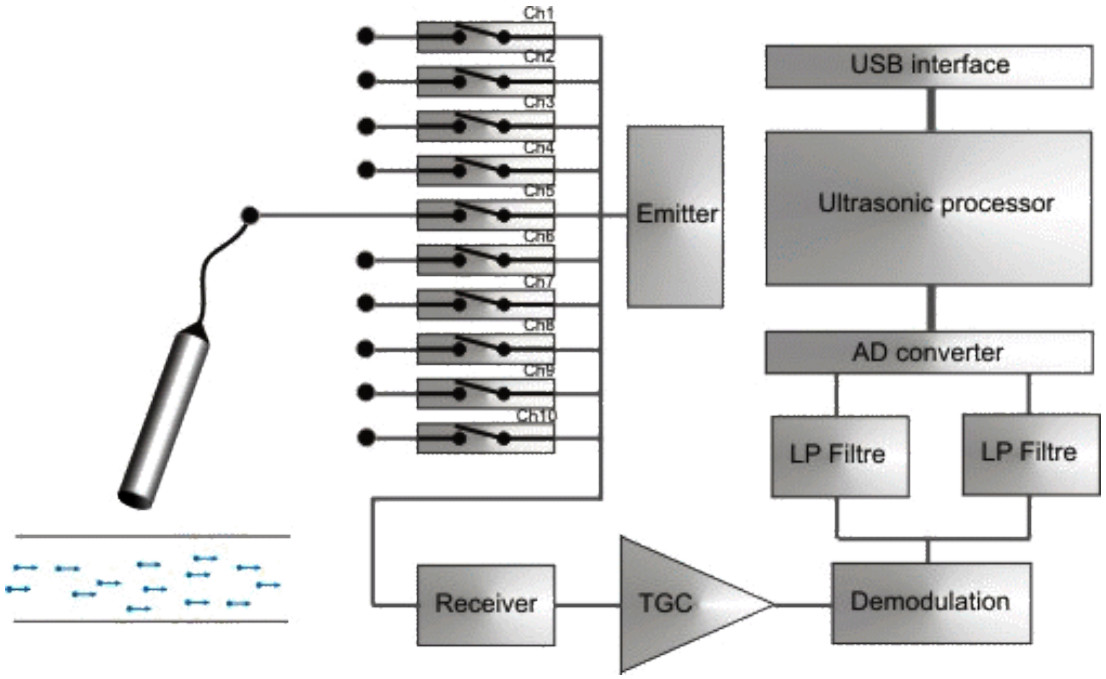

Figure 3.2: Internal architecture of the DOP3010 velocimeter [72]

the maximal velocity. On the other hand, emitting frequency is the possible adjusting parameter, which is related with both $v^{\parallel}_{max}$ and l_{max} via the expression:

$$l_{max} v^{\parallel}_{max} = \frac{c^2}{8 f_e}$$

3.2.2 DOP3010 velocimeter

Figure 3.2 shows the schematic view of the DOP3010 velocimeter. The emitter and receiver is the same transducer, and with DOP3010, up to 10 transducers can be used at the same time. Received signal is amplified using time gain compensation (TGC) to compensate the attenuation of the ultrasound during the propagation in the liquid. The next step is the multiplication of the echo signal by the reference (emitted) signal. The low-pass filter then isolates the Doppler information, which is converted into digital data by AD converter. The Doppler frequency is then calculated using powerful autocorrelation algorithm, and the resulting data is then sent to the PC via the USB interface.

3.3 Particle image velocimetry basics

PIV method, which has begun in 80s, allows obtaining velocity vector distribution in a certain plane with high spatial resolution. Nowadays, it is a well-known method used in various branches of aerodynamics and biology, two-phase flows, combustion processes, fundamental turbulence research, as well as very small scale flows. Because of different requirements and specifics of applications, a number of PIV variations are developed, and nowadays, with PIV name are associated such modifications of this method as 3C PIV, 2 + 1D PIV, micro-PIV, stereo PIV, time-resolved PIV, etc. The method that is described here and used in this work is called 2D 2C PIV (two-dimensional, two-component PIV) because it allows obtaining two velocity components in one two-dimensional plane (cross section).

It is possible to get the information about the flow character by introducing tracers in the flow and by following their movement. The simplest example is a leaf that falls on a surface of river. Such approach gives good qualitative impression about the flow field character but no measurable data. PIV brings this idea to quantitative description level.

PIV measurement system consists of several components (Figure 3.3). Particles (tracers) are injected into the investigated flow, where they are illuminated by a laser beam. In most PIV systems, two lasers are used due to necessity of producing two impulses with short time delay (couple of microseconds). Lasers are usually of the same type, power, and wavelength, and their beams are aligned to have the same axis. Lenses are used to convert the laser beam into the light sheet.

Light that is scattered by particles, is registered with digital camera. Cameras for PIV are specially designed for recording an image pair within couple of microseconds. The interval between image pairs is usually approximately 0.1 s for standard PIV.

The test sections have to be manufactured of transparent material, usually of glass or organic glass. Additional requirement is a minimization of reflections to obtain an image of high quality. This can be done either by covering reflecting surface with a black paper or tape or by painting these surfaces with special coverings (colors) that reduce reflections.

In PIV data post processing each particle is not tracked because unlike in PTV (particle tracking velocimetry), the volumetric particle density is high. The velocity information is obtained by following the groups of particles – first image from a pair is divided in interrogation windows, which size determine spatial resolution of the

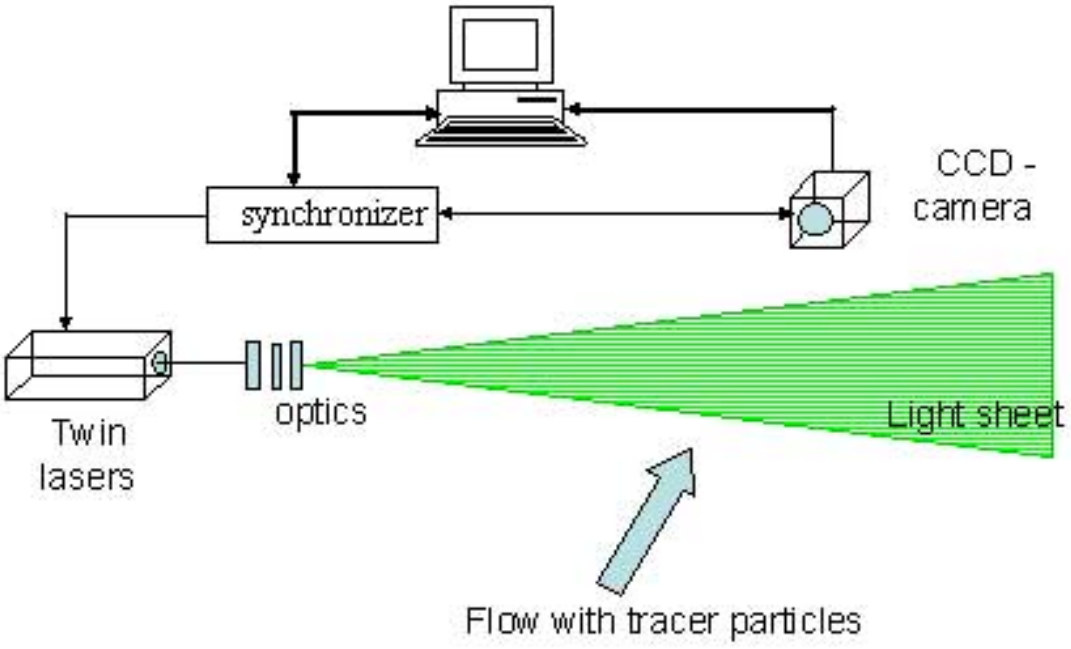

Figure 3.3: PIV principle [73]

velocity field. Translating interrogation window by a vector (ξ, η), a cross correlation can be found between the first and second images in pair.

$$R(\xi, \eta) = \sum_{i}^{N} \sum_{j}^{N} I(x, y) I(x + \xi, y + \eta)$$

Here, I is the intensity of the light in the interrogation window. As the result, correlation distribution dependence on vector (ξ, η) is found. The maxima of the correlation corresponds to most probable displacement vector in current interrogation window. In the same way, vectors are found in the whole plane.

Multipass interrogation algorithm is also widely used. In the first step (pass), the frame is divided into $N \times N$ pixel interrogation windows, and the standard procedure is performed to find the velocity field. In the next pass, the frame is divided into smaller IW, say $N/2 \times N/2$. For this pass, the velocity value from the previous pass is used as an initial guess. This process can continue on many levels. Multipass algorithm allows speeding up the velocity calculation time.

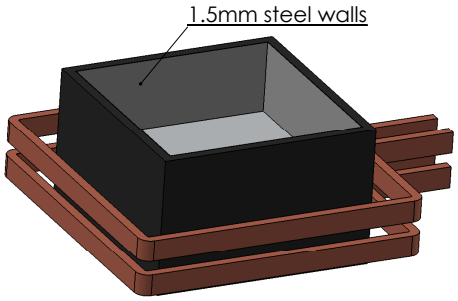

(a) Isometric view of the experimental model

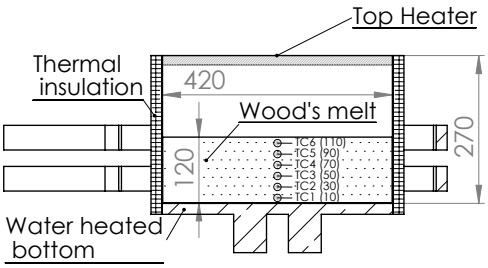

(b) Middle cross section of the experimental model. Positions of thermocouples are showed as TC1. . .6

Figure 3.4: Sketch of experimental model. Sidewalls are isolated to reduce the horizontal temperature gradient.

3.4 Setup of the model

Experimental results were obtained using physical model (Figure 3.4a), which consisted of square-shaped steel crucible (wall thickness 1.5 mm) with side length $W = 420$ mm and height $H = 270$ mm, filled to the level of $L = 120$ mm, placed on the aluminum plate with constant temperature, which is obtained by hot water ($T = 80$ ℃) flow. Wood's alloy (50% Bi, 25% Pb, 12.5% Sn, 12.5% Cd, melting temperature 72 ℃) was used as working liquid. The properties of Wood's alloy in comparison with silicon properties are listed in Table 3.1. The differences between both metals are within one order of magnitude that allows using this alloy for downscaled model.

The crucible is surrounded by two copper windings that are connected in one phase to the 50 Hz power supply. As both windings are connected with the bridge, the current can redistribute between them, but the current ratio between top and bottom winding I_{TOP}/I_{BOTTOM} was approximately 1.08 for all cases. The maximal current was 5,000 A with total power up to 8.2 kW.

The radiation heater is used as lid on the crucible, which allows obtaining vertical temperature gradient in the alloy. The emissivity of the Wood's alloy is low ($\epsilon \sim 0.15$), and the radiation heating is not efficient for obtaining high temperature-gradients. However, significant part of the heat flux on the free surface is ensured by the heated air in the space between alloy and lid. In this setup steady temperature difference between top and bottom surface up to 80 ℃ was obtained in the liquid at rest. Vertical temperature profile was measured using six thermocouples (TC); their vertical coordinates z (bottom corresponds to z = 0) are shown in Figure 3.4b. Photo of experimental equipment is shown in Figure 3.5.

Figure 3.5: Photo of the experimental setup

Property	Silicon	Wood's Alloy	Ratio
Density, kg/m^3	2,530	9,400	3.72
Kinematic viscosity, m^2/s $\cdot 10^{-7}$	3.3	4.5	1.36
Heat conductivity, W/m K	67.0	14.0	0.21
Heat capacity, J/kg K	990	168	0.17
Thermal expansion coefficient, 1/K $\cdot 10^{-4}$	1.44	1.20	0.83
Electrical conductivity, S/m $\cdot 10^6$	1.2	1.15	0.96

Table 3.1: Liquid silicon and Wood's alloy physical properties

Experimental setup allows also measuring velocity field in the crucible using ultrasound Doppler velocimetry. Profiles were measured with single ultrasound probe through the wall and the free surface. For 2D velocity distributions, several profiles were taken in one plane. See details of measurement procedure in Chapter 6.

3.5 Scaling of the model

For the scaling of the present investigation results, all relevant dimensionless numbers have to be matched. In this section, the scaling coefficients for all relevant parameters will be calculated for the transfer of the current results to generation 5 (G5) silicon growth crucible with the side length $L = 840$ mm and filling height $H = 240$ mm. The data from the Table 3.1 will be useful for this task. The relevant dimensionless parameters discussed here will be molecular Prandt number Pr, dimensionless

Property	Model	G5
Length, cm	42	84
Frequency, Hz	50	12
Magnetic field in melt, mT	20	2.7
Temperature gradient, K/m	750	21
Velocity, cm/s	5.0	1.85

Table 3.2: Summary of the typical parameters for physical model and corresponding scaled values for G5 crucible

frequency $\tilde{\omega}$, Reynolds number Re, Grashof number Gr, Richardson number Ri, and magnetic interaction parameter F_{em}.

Prandtl number is defined only by the material properties of the melt. Both silicon and Wood's alloy are low Prandtl number liquid, for silicon, $Pr_{G5} = 0.011$, while for Wood's alloy, Prandtl number is 4.64 times higher, $Pr_M = 0.051$. Here and further, the subscript G5 stands for the value for silicon production crucible of the generation G5, and subscript M is for physical model with Wood's alloy.

The dimensionless frequency $\tilde{\omega}$ gives the possibility to calculate the corresponding frequency of the G5 crucible. Assuming equal $\tilde{\omega}$ in both cases, the following equality is obtained:

$$f_{G5} = \frac{\sigma_M L_M^2}{\sigma_{G5} L_{G5}^2} f_M = 0.24 f_M$$

The G5 frequency corresponding to the 50 Hz in the model is 12 Hz, which is still enough for mixing, but it is already in the range when pulsations of the EM field might influence the flow. The skin depth for the physical model at 50 Hz is $\delta = 66.3$ mm, and the dimensionless frequency is $\tilde{\omega} = 20.1$ (half of the side length is used as characteristic length).

The magnetic force F_{MAX} is proportional to B^2, and therefore, relation for magnetic field can be obtained $B_{G5} = 0.134 B_M$.

Reynolds numbers equal for model and G5 crucible, the scaling of the velocity is obtained $Re_{G5} = Re_M$. The obtained relation is $U_{G5} = 0.37 U_M$.

The scaling of temperature conditions in small physical models reported in literature (in [30] model with length ratio $L_{G5}/L_M = 8$) is limited because it is proportional to the cube of length ratio. In the current work, the length ratio is relatively small $L_{G5}/L_M = 2$. The equality of Grashof numbers leads to the temperature relation $T_{G5} = 0.056 T_M$. Vertical temperature derivative $G = \partial T/\partial z$ is also important for scaling of heat fluxes, and the estimation of buoyancy forces is $G_{G5} = 0.028 G_M$.

The highest temperature gradients that can be obtained in this model are $G = 750$ K/m, which corresponds to $G_{G5} = 21$ K/m (see Table 3.2). The typical numbers for silicon furnaces are one order of magnitude higher.

All parameters are summarized in Table 3.2. This data can be used for scaling of the current results to the G5 silicon production crucible. Since most of hydrodynamic parameters are within the same order of magnitude, conclusions made from current research can be partially transferred to G5 silicon crucibles.

Chapter 4

Simplified 2D Analysis

At very high Ri numbers, the main flow tends to become more two dimensional. In the limit $Ri \to \infty$, flow is perfectly two dimensional, and any body forces that have vertical component will be balanced by buoyancy, and the flow will be determined by horizontal force components. In other words, horizontal fluid layers can be treated as isolated and vertical momentum transport neglected.

This chapter is devoted to theoretical analysis of the simplified flow in two dimensions. Velocity dependence on EM field frequency will be derived.

4.1 Creeping flow in rectangular box

4.1.1 General solution

The flow is analyzed in a bounded 2D box with size $2L_x \times 2L_y$: $-L_x > x > L_x$, $-L_y > y > L_y$ with stream function formulation:

$$\frac{\partial\left(\nabla^2\psi\right)}{\partial t} + \frac{\partial\psi}{\partial y}\frac{\partial}{\partial x}\left(\nabla^2\psi\right) - \frac{\partial\psi}{\partial x}\frac{\partial}{\partial y}\left(\nabla^2\psi\right) = \nu\nabla^4\psi + \frac{1}{\rho}\left(\frac{\partial f_y}{\partial x} - \frac{\partial f_x}{\partial y}\right) \tag{4.1}$$

Here, ν is kinematic viscosity, ρ is density, f_x and f_y are body force density components. The stream function ψ is defined as follows:

$$u_x = \frac{\partial\psi}{\partial y}; \qquad u_y = -\frac{\partial\psi}{\partial x} \tag{4.2}$$

Analytic solution is not possible to obtain for this equation, but certain assumptions or simplifications can lead to solutions that are able to describe certain characteristics of unsimplified system. Precise solution can be easily obtained for one-dimensional case of Stokes flow [74],[75]. If the body forces are constant in time and

inertial terms negligible, this problem can be described by inhomogenous biharmonic equation:

$$\nabla^4 \psi = F(x, y)$$

Here, $F(x, y) = -\nu^{-1}\rho^{-1}(\partial f_y/\partial x - \partial f_x/\partial y)$ is last term in equation (4.1). When Reynolds number is large, this assumption is never correct. However, in Stokes approximation, the balance between viscous dissipation and flow generation by body forces takes place. It was shown in [76] that neglecting inertial terms can still give good approximation for flow dependency on body force parameters.

For two-dimensional flow, no-slip boundary condition makes finding solution more complicated; therefore, free-slip condition is used for simplicity:

$$\frac{\partial \psi}{\partial x}|_{y=\pm L_y} = 0$$
$$\frac{\partial \psi}{\partial y}|_{x=\pm L_x} = 0$$

Green's function for biharmonic equation is found by Fourier series representation of Dirac delta function:

$$G(x, y, \xi, \eta) = \frac{1}{L_x L_y} \sum_{n=1}^{\infty} \sum_{k=1}^{\infty} \frac{1}{(p_n^2 + q_k^2)^2} sin\,(p_n x)\, sin\,(q_k y)\, sin\,(p_n \xi)\, sin\,(q_k \eta) \quad (4.3)$$

Here, coefficients p_n and q_k are:

$$p_n = \frac{\pi n}{L_x}; \qquad q_k = \frac{\pi k}{L_y}$$

The solution of inhomogenous equations can be found now for any analytic force field:

$$\psi(x, y) = \int_{-L_x}^{L_x} \int_{-L_y}^{L_y} F(\xi, \eta) G(x, y, \xi, \eta) d\xi d\eta \quad (4.4)$$

4.1.2 Analytical example

As an example for two-dimensional creeping flow approach, simple 2D analytic force function is chosen in the form:

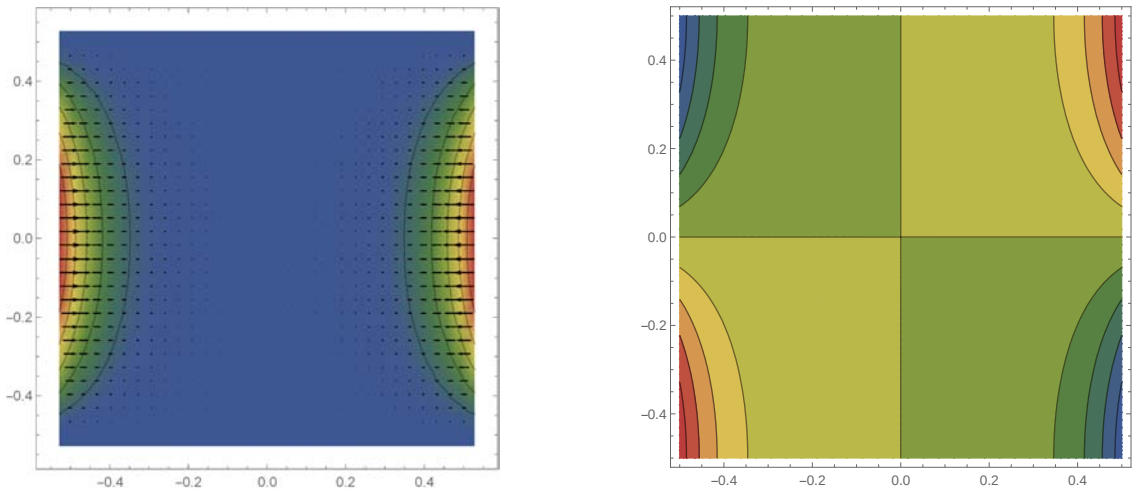

(a) Force density f (b) $\nabla \times \vec{f}$

Figure 4.1: Force distribution in the rectangle according to eq. 4.7. The force is assumed to have only x component. $L_x = L_y = 0.5$, $\delta = 0.2$

$$f_x = A \cdot sinh\left(\frac{2x}{\delta}\right) cos\left(\frac{\pi y}{2L_y}\right); \tag{4.5}$$

$$f_y = 0; \tag{4.6}$$

$$F(x,y) = \frac{\pi A}{2\rho\nu L_y} sinh\left(\frac{2x}{\delta}\right) sin\left(\frac{\pi y}{2L_y}\right) \tag{4.7}$$

This force function is chosen to have exponential decay of force on two opposite sides (along x coordinate) and have maximum in the middle along y coordinate. δ is the skin depth of electromagnetic field, while $\delta/2$ is the decay of Lorentz force. The force field is shown in Figure 4.1a with corresponding curl of force in 4.1b.

The obtained stream function is expressed as sine series with known coefficients $C_{i,j}$:

$$\psi(x,y) = \Psi_0 \sum_{n=1}^{\infty}\sum_{k=1}^{\infty} C_{n,k} \sin(p_n x) \sin(q_k y) \tag{4.8}$$

$$C_{n,k} = \frac{(-1)^n(-1)^k nk}{\left(p_n^2 + \frac{4}{\delta^2}\right)\left(4k^2-1\right)\left(p_n^2+q_k^2\right)^2}$$

$$\Psi_0 = \frac{8\pi A \sinh\left(\frac{2L_x}{\delta}\right)}{\rho\nu L_x^2 L_y}$$

Using stream function definition (4.2), velocity distribution can be obtained:

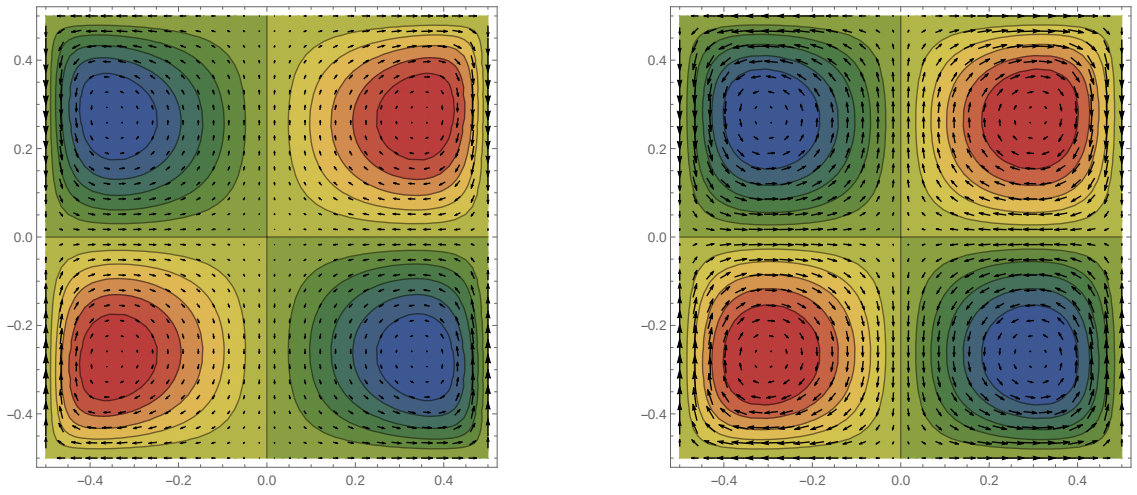

(a) $\delta = 0.01$ m (b) $\delta = 0.2$ m

Figure 4.2: Analytically obtained stream function (in colormap) and corresponding velocity field (vectors) for two different skin depth δ

$$u_x(x,y) = \Psi_0 \sum_{n=1}^{\infty}\sum_{k=1}^{\infty} C_{n,k} q_k sin\,(p_n x)\, cos\,(q_k y)$$
$$u_y(x,y) = \Psi_0 \sum_{n=1}^{\infty}\sum_{k=1}^{\infty} C_{n,k} p_n cos\,(p_n x)\, sin\,(q_k y)$$

The obtained flow (shown in Figure 4.2) contains four main vertexes, two of them rotating in clockwise and two other in counterclockwise direction. This calculation is performed for the rectangle $L_x = L_y = 0.5$ m, with constant coefficient $\Psi_0 = 20,100$ s^{-1} m^{-4} for two different skin depths - $\delta = 0.01$ m (Figure 4.2a) and $\delta = 0.2$ m (Figure 4.2b). The results show that at lower δ, the vortex centers become closer to the wall, and vortexes become less circular.

The convergence of the series is judged by observing normalized stream function values ψ_C at fixed space points with different number of terms N. Normalization performed against stream function value in the same point with $N = 50$ sum terms (it was checked that with 50 terms, series are always converged to within 99.5% precision for skin depths between 0.01 m and 0.2 m). Figure 4.3 shows that stream function value with 90% precision is obtained already at $N = 10$. One percent error is achieved at number of terms $N = 30$, which is used for all calculations in Figure 4.2.

Convergence character depends also on skin layer thickness. At shielding factor $\tilde{\omega} = 2(L/\delta)^2 = 20,000$ more sum terms are necessary for converged solution, since at

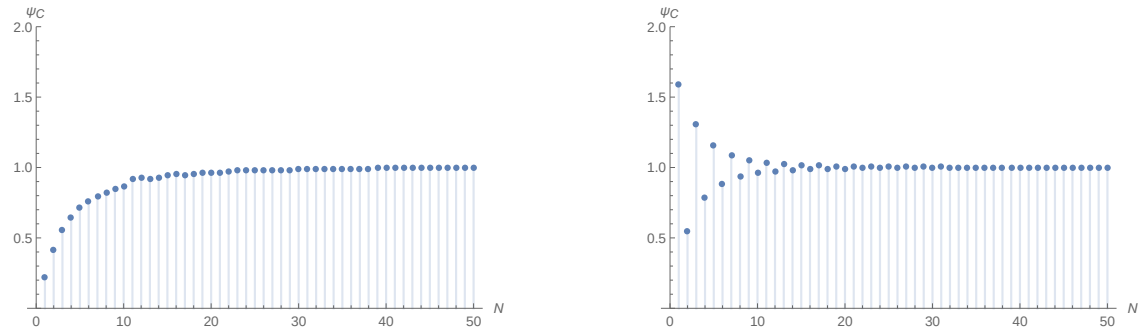

(a) Point $x = L_x$, $y = L_y$ (b) Point $x = 0$, $y = L_y$

Figure 4.3: Normalized stream function values with different number of series terms at fixed space points. $\delta = 0.05$ is used here.

$N = 50$, only 95% precision is achieved. On the other hand, at small frequency (large skin depth), fewer terms are required. For example, at $\tilde{\omega} = 2$, first term of the series already gives 95% precision.

The analysis of coefficients $C_{n,k}$ shows that $C_{1,1}$ is always the largest in series, and this is the reason why exactly four vortexes are formed. At smaller skin depth the ratio between first coefficient $C_{1,1}$ and $C_{2,1}$ becomes smaller and has limit $\lim_{\delta\to 0} C_{1,1}/C_{2,1} = 3.125$. At finite skin depth, this ratio is larger and reaches another limit $\lim_{\delta\to\infty} C_{1,1}/C_{2,1} = 12.5$. At large skin depths, investigated flow is very similar to Taylor-Green vortex [77], which is characterized by stream function in the form

$$\psi_T = Csin(ax)sin(by)$$

The dependence of stirring velocity on the frequency is a widely investigated topic [78, 79]; however, there is no general law derived for this dependence. Eq. (4.8) could be used to deduce such dependence, but it contains only dependence of the velocity on the skin depth parameter δ. Parameter A can also depend on δ; in the case of stirring by AC fields, it depends strongly on the frequency and magnetic field intensity. For half-space with magnetic field intensity B_0 on its surface, known solution for force density is expressed as follows:

$$f = \frac{B_0^2}{2\mu_0\mu\delta} exp(-\frac{2x}{\delta}) \tag{4.9}$$

From here, simple relation between velocity magnitude and skin depth δ can be obtained. For the simplest result, only $C_{1,1}$ from the series is used.

$$U(\tilde{\omega}) \sim \frac{B^2}{\nu} \frac{\sqrt{\tilde{\omega}}}{\pi^2 + 2\tilde{\omega}} \tag{4.10}$$

To validate these theoretical considerations, 2D numerical simulations for bounded flow were performed with no-slip boundary condition, because it has more practical importance than the free-slip boundary condition, which was used in theoretical result. In the numerical simulations, $k-\omega-SST$ turbulence model is used in turbulent regime, and formula 4.7 is used as forcing function. Symmetry condition was used on the boundaries x=0 and y=0 to stabilize the flow and prevent flow structure changes. For comparison with numerical data, maximal velocity in the volume is taken. Since the magnitude of the velocity for case with and without slip on walls differs significantly, all results are normalized so, that the maximal velocity is 1: $max(U(\tilde{\omega})) = 1$.

Good agreement with numerical simulations is obtained for $Re < 1,000$ (Figure 4.5). For larger Reynolds, numbers numerical results have the same peak value, but their decrease is slower with $\tilde{\omega}$ increase. For flows with pronounced inertial effects, the turbulence can be considered by using eddy viscosity η_T concept. In developed turbulence, the scaling laws suggest that $\nu_{lam} << \nu_t \sim U$. Using this assumption for Eq. 4.10, the velocity dependence on frequency for turbulent regime will be $U_T(\tilde{\omega}) \sim \sqrt{U(\tilde{\omega})}$. This result is in correspondence with the asymptotic relation for large frequencies $\lim_{\tilde{\omega}\to\infty} U_T(\tilde{\omega}) = \tilde{\omega}^{-1/4}$ shown in [80]. Figure 4.5 shows better agreement between $U_T(\tilde{\omega})$ and numerical simulation data for small frequencies $\tilde{\omega} < 100$ than dependence for laminar case $U(\tilde{\omega})$. The discrepancies at the larger frequencies can be explained with the fact, that skin depth becomes comparable in size with hydrodynamic boundary layer thickness. Another problem is that velocity at higher frequencies first member of series gives less accurate solution.

The equation 4.9 leads to the $U \sim B^2 \sim I^2$ velocity dependence, which does not agree with well-known fact $U \sim B \sim I$ [81], [82]. 2D RANS simulations with $k-\omega-SST$ model show that there is a validity region for both relations – the analytic solution for small Reynolds numbers and linear proportionality for large Reynolds numbers (Figure 4.4). The sharp transition between the regimes in numerical results is not necessarily physical effect; however, the general tendency is plausible. In Figure 4.4, the transition Reynolds number $Re^{CR} = 1200$ is also a point where electromagnetic forcing and inertial forces are in balance, and ratio F_{EM}/Re^2 (see equation 2.16) is 0.87. Noteworthy is also the fact that this ratio does not exceed 1.0 with further increase of the current.

4.1.3 Cylindrical container with axially symmetric forces

The velocity dependence on the frequency can be estimated in similar was as described in previous section for other systems with EM forces. One of the most

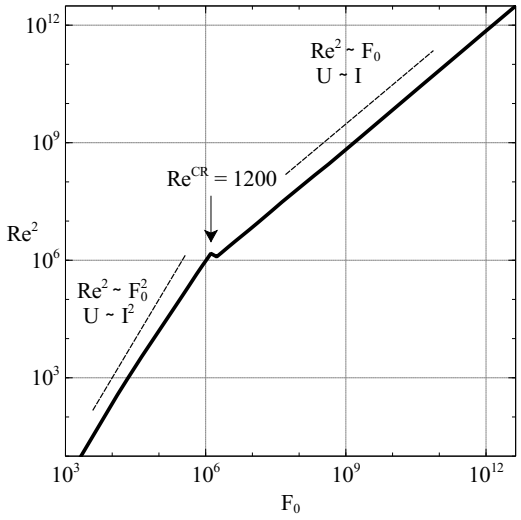

Figure 4.4: Re^2 dependence on EM forcing parameter F_0 in $k-\omega$ results. Transition between regimes occurs at Reynolds number $Re^{CR} = 1,200$.

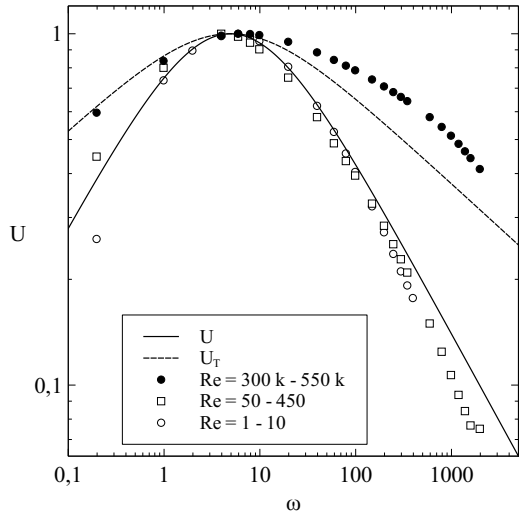

Figure 4.5: Flow velocity dependence on the frequency. Lines represent analytical models, symbols – numerical simulations

known configurations of this type is cylindrical melt domain in cylindrical inductor. Such setups are widely used in metallurgy, as well as crystal growth (e.g., Bridgeman technique). The results from current estimation can be compared with existing results in this field.

Axisymmetric Stokes flow in cylindrical coordinates under the influence of the force density $\vec{f}$ can be written in the following form:

$$\frac{1}{r^2}\Delta^*\left(\Delta^*\psi\right) + \frac{1}{r\rho\nu}\left(\frac{\partial f_z}{\partial r} - \frac{\partial f_r}{\partial z}\right) = 0 \tag{4.11}$$

Here, Δ^* is the elliptic Grad-Shafranov operator – $\Delta^* = \frac{\partial^2}{\partial r^2} - \frac{1}{r}\frac{\partial}{\partial r} + \frac{\partial^2}{\partial z^2}$. In cylindrical coordinate system, stream function is defined as follows:

$$u_r = -\frac{1}{r}\frac{\partial\psi}{\partial z}; \qquad u_z = \frac{1}{r}\frac{\partial\psi}{\partial r} \tag{4.12}$$

Green's function for equation (4.11) can be found by solving equation

$$\frac{1}{r^2}\Delta^*\left[\Delta^* G^*(r,z,r',z')\right] = \frac{\delta(r-r')\delta(z-z')}{2\pi r} \tag{4.13}$$

By choosing z dependence of G^* in the form of sine series (see eq. (4.3)), the equation (4.13) simplifies to

$$\frac{1}{r^2}\Delta^k\left[\Delta^k g^*(r,r')\right] = \frac{\delta(r-r')}{2\pi r} \tag{4.14}$$

Here, $\Delta^k = \frac{\partial^2}{\partial r^2} - \frac{1}{r}\frac{\partial}{\partial r} - q_k^2$. The solution of homogeneous equation $\Delta^k \Delta^k g_0^* = 0$ is $g_0^* = c_1 r J_1(kr/R) + c_2 r Y_0(kr/R)$. The term containing modified Bessel function of the first kind does not go to zero at the axis – $\lim_{r\to 0} rY_1(kr/R) = 2R/\pi k$. Therefore, only the first term of this solution fits the boundary conditions. As it was shown in [83], g^* is expressed in the following form:

$$g^*(r, r') = \sum_{n=1}^{\infty} A_n(r') r J_1(\frac{\alpha_n r}{R}) \tag{4.15}$$

Here, α_n is n-th root of $J_0(\alpha_n) = 0$. Then the substitution of (4.15) into (4.14) yields

$$\sum_{n=1}^{\infty} \left(\left(\frac{\alpha_n}{R}\right)^2 + q_k^2 \right)^2 A_n(r') J_1\left(\frac{\alpha_n r}{R}\right) = \frac{\delta(r - r')}{2\pi}$$

Now the expansion of $\delta(r - r')$ as Fourier-Bessel series gives the expression for A_n.

$$A_n(r') = \frac{1}{\pi R^2} \frac{r' J_1\left(\frac{\alpha_n r'}{R}\right)}{\left(\left(\frac{\alpha_n}{R}\right)^2 + q_k^2\right)^2}$$

Finally, the solution of equation (4.13) is the Green's function in the form

$$G^*(r, z, r', z') = \frac{2}{\pi R^2 L_z} \sum_{n=1}^{\infty} \sum_{k=1}^{\infty} \frac{r r' J_1\left(\frac{\alpha_n r}{R}\right) J_1\left(\frac{\alpha_n r'}{R}\right)}{\left(\left(\frac{\alpha_n}{R}\right)^2 + q_k^2\right)^2 \left[J_2(\alpha_n)\right]^2} \times \\ \times sin\left(q_k z\right) sin\left(q_k z'\right) \tag{4.16}$$

To obtain the solution, an integration over whole domain needs to be performed similarly like in case of 2D solution. Integration over z is simple, while integration over r is more complicated due to integral of the type:

$$\int_0^R r F^r(r) J_1\left(\frac{\alpha_n r}{R}\right) dr$$

Here, F^r is the radial-dependent part of the force function $F(r, z) = F^r(r) F^z(z)$ (it is assumed that F can be split in such way).

4.1.4 Example solution in cylindrical flow container

In the well-known 1D solution (dependence only on r) of Eq. (2.10) the axial magnetic field distribution in conducting cylinder of radius R is

$$B_z(r) = B_0 \frac{J_0((\mathrm{i} - 1) r/\delta)}{J_0((\mathrm{i} - 1) R/\delta)} \tag{4.17}$$

However, this result is valid only in the middle of a very long cylinder, while in the edge zones, the radial component of magnetic field appears. Bowler in [84] has shown the analytic solution for eddy current distribution in finite cylinder. The magnetic vector potential $\vec{A}$ is given by distribution $C_n \cos(q_n z) I_1(\gamma_n r)$, where $\gamma_n = \sqrt{q_n^2 - \mathrm{i}\omega\mu_0\sigma}$ is the n-th root of transcendental equation. Cosine is used in case of symmetrical coil with $z = 0$ is a symmetry plane. Although this solution is explicit, the roots are not explicitly found and require numerical algorithm to be found. Finding the q_n roots is a difficult problem, which is described in details in [85].

If the coil is significantly shorter than the cylinder, then the assumption $\vec{A} = 0$ at the top and bottom of the cylinder is reasonable. This leads to $q_n = \pi(2n-1)/H$ eigenvalues. Assuming cosine pattern of the field is widely used to derive simplified formulas in electrical engineering [86], therefore, here, only one coefficient q_1 with $n = 1$ will be used. For this case, B_z can be written as follows:

$$B_z = \frac{\partial}{\partial r}\left[C \cos(q_1 z) I_1(\gamma_1 r)\right] = C\gamma_1 \cos(q_1 z) I_0(\gamma_1 r)$$

If constant magnetic field density B_0 is set on the surface of the melt at the point $(R, 0)$, which corresponds to constant current in windings, the coefficient C can be found

$$C\gamma_1 I_0(\gamma_1 R) = B_0$$

The B and j distributions in this case are written as follows:

$$B_z = B_0 \cos\left(q_1 z\right) \frac{I_0\left(r\gamma_1\right)}{I_0\left(R\gamma_1\right)};$$
$$j_\phi = \frac{B_0 \mathrm{i}\omega\sigma}{\gamma_1} \cos\left(q_1 z\right) \frac{I_1\left(r\gamma_1\right)}{I_0\left(R\gamma_1\right)}$$

The curl of force term from the equation 4.11 can be therefore written in the following form:

$$F(r,z) = -\frac{1}{r\rho\nu}\frac{1}{2} Re\left[\frac{\mathrm{i}\omega\sigma|B_0|^2}{\gamma_1} q_1 \sin(2q_1 z) \frac{I_1\left(r\gamma_1\right) I_0^*\left(r\gamma_1\right)}{I_0\left(R\gamma_1\right) I_0^*\left(R\gamma_1\right)}\right] \tag{4.18}$$

The obtained solution of the stream function is expressed with equation:

$$\psi(r,z) = \frac{2|B_0|^2}{\rho\nu R^2 H^2} \sum_{n=1}^{\infty} C_n J_0\left(\alpha_n r\right) sin\left(\frac{2\pi z}{H}\right) \tag{4.19}$$

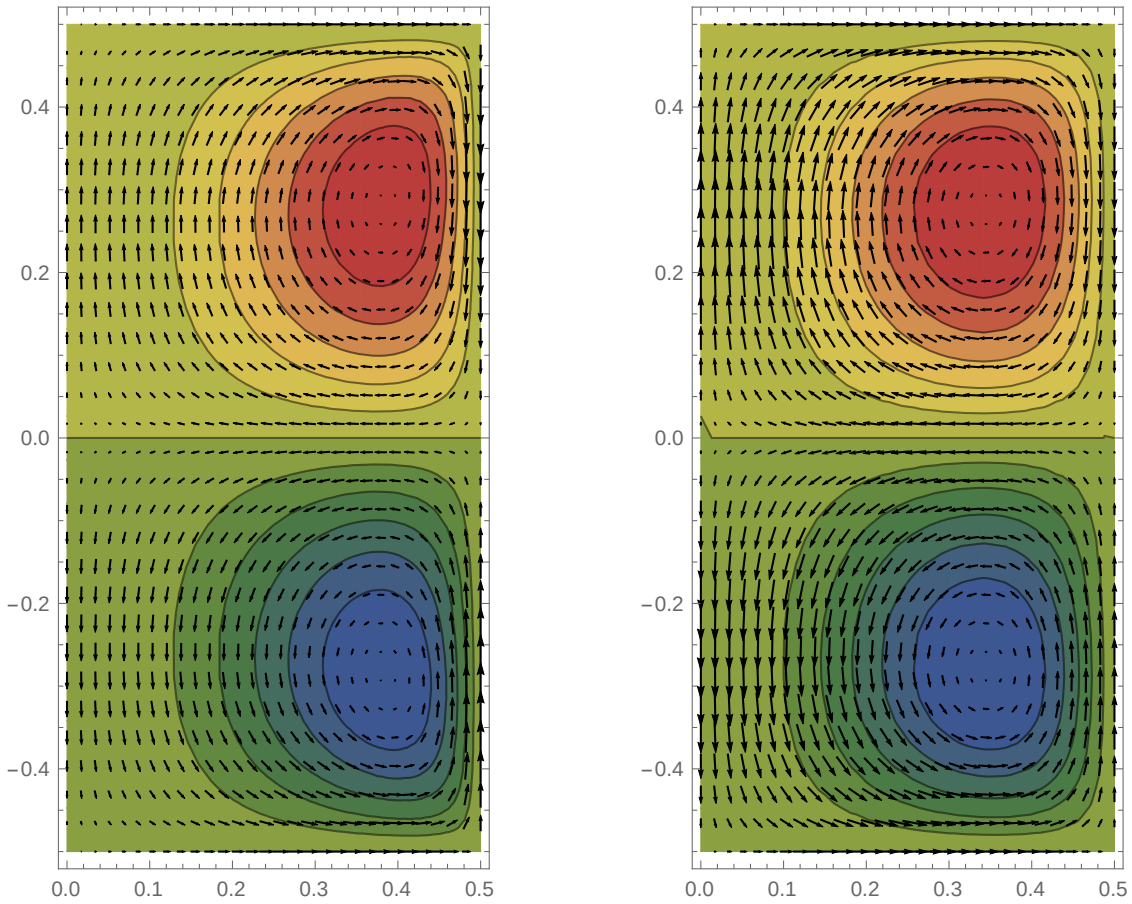

(a) $\delta = 0.01$ m (b) $\delta = 0.2$ m

Figure 4.6: Analytically obtained 2D axisymmetric stream function (in colormap) and corresponding velocity field (vectors) for two different skin depth δ.

$$C_n = \frac{P_n}{\left(\frac{\alpha_n}{R}^2 + \left(\frac{2\pi}{H}\right)^2\right)^2 \left[J_2(\alpha_n)\right]^2}$$

Constant P_n can be written in explicit form but requires numerical integration to be computed because it includes three Bessel function terms:

$$P_n = \int_0^R rRe \left[\frac{\mathrm{i}\omega\sigma I_1\left(r\gamma_1\right) I_0^*\left(r\gamma_1\right)}{\gamma_1 I_0\left(R\gamma_1\right) I_0^*\left(R\gamma_1\right)}\right] J_1\left(\frac{\alpha_n r}{R}\right) dr \tag{4.20}$$

The stream function of this flow is depicted in Figure 4.6 for a cylinder with radius $R = 0.5$ m, height $H = 1.0$ m for two different skin depths $\delta = 0.01$ m (Figure 4.6a), and $\delta = 0.2$ m (Figure 4.6b). Here, like in 2D flow, smaller skin depth leads to stronger velocity gradient near wall.

This solution have one practical interest because it gives the velocity dependence

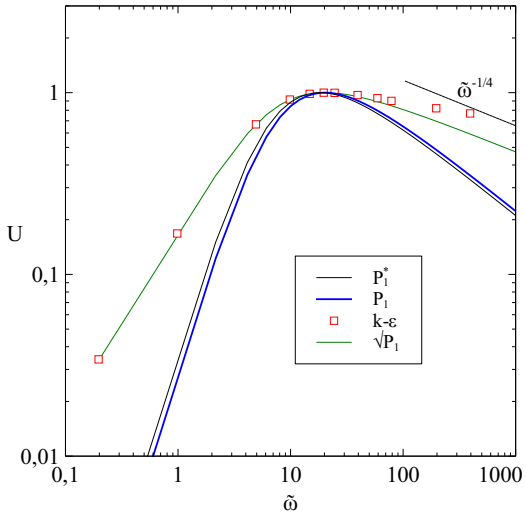

Figure 4.7: Flow velocity dependence on the frequency for axisymmetric crucible.

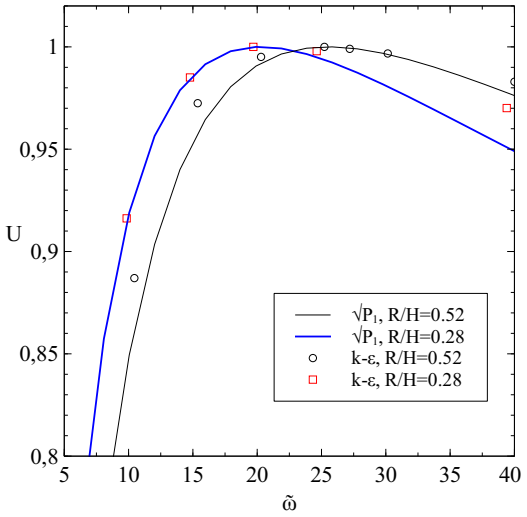

Figure 4.8: Flow velocity dependence on the frequency for different crucible radius/height ratio

on frequency. The first-order approximation is $U(\tilde{\omega}) \sim P_1$. In case of a very long cylinder, simplified expression can be obtained that can also be derived from equation (4.17).

$$P_1^* = \int_0^R rRe \left[\frac{2J_1\left((\mathrm{i}-1)r/\delta\right) J_0^*\left((\mathrm{i}-1)r/\delta\right)}{\mu_0 \delta J_0\left((\mathrm{i}-1)R/\delta\right) J_0^*\left((\mathrm{i}-1)R/\delta\right)} \right] J_1\left(\frac{\alpha_1 r}{R}\right) dr \tag{4.21}$$

Following the same considerations as in section 4.1.2, the dependence for turbulent regime can be obtained $U_T \sim \sqrt{P_1}$.

To validate the predicted frequency dependence, numerical simulations were performed using $k-\omega-SST$ turbulence model for the experimental crucible described in [82] – Wood's alloy as working material, height H=570 mm, radius R=158 mm. In these simulations, the force density was not assumed in analytic form but calculated numerically using exact geometry of the crucible. In this setup the force distribution is symmetrical with respect to the horizontal middle plane of the crucible due to symmetric position of windings. The maximal average velocity in the crucible as function of dimensionless frequency $\tilde{\omega}$ is shown in Figures 4.7 and 4.8.

The frequency dependence predicted by equation 4.20 shows too narrow peak, exactly as in the 2D case. However, the $\sqrt{P_1}$ shows almost perfect agreement with numerical results up to the $\tilde{\omega} = 80$. In Figure 4.7 all results shown are for $R/H = 0.28$. It is visible that at this R/H ratio, the P_1 and P_1^* give very similar result. This result is also close to the one presented by Tir [76] already in 1976, which was obtained

by assuming plausible flow pattern. The expressions proposed by Tir were written using Kelvin functions and were nearly identical to equation 4.21. The difference is the $rJ_1(\alpha_1 r/R)$ multiplier under the integral, which represents the velocity shape. In [76], two different shape profiles were assumed: rectangular

$$\tilde{u}_z(r) = \begin{cases} 1 & \text{if } \xi < r < R \\ -1 & \text{if } 0 < r < \xi \end{cases}$$

where ξ is empyrically found coordinate detaching two streams, and a pattern which is equal with force radial pattern.

In Figure 4.8, two cases are compared with different r/H ratios. The shift of maximal frequency is small and would not be visible on the logarithmic scale in Figure 4.7. It is clear that equation 4.20 represents correct the tendency that with increase of R/H ratio, the maximal frequency shifts to the higher values.

Showed 2D stream function approach showed good agreement with known theoretical and numerical results, and therefore, it can be used to predict velocity-frequency dependence. However, this approach here was tested only with analytic force function. For more precise results, knowledge of exact force distribution is necessary. Unfortunately, force distribution is rarely known in analytic form.

Chapter 5

Vortex Merging in 2D Recirculating Flows

This chapter is devoted to vortex merging topic in 2D planar flows. Vortex merging is responsible for unsymmetrical flow fields that are observed in symmetrical arrangements. Such effect will be shown in Chapters 6 and 7. Chapter 8 will also present flow arrangement that is very similar to the one showed in this chapter.

This chapter also shows possibility to experimentally investigate EM driven flows in weak conducting transparent fluids (e.g. saltwater) where visual measurement techniques can be applied.

5.1 Stability of 2D Taylor-Green vortex

The Taylor-Green (TG) vortex [77] is a widely used model in the investigation of fluid flows [87], in particular, generation of small-scale turbulence [88], MHD phenomena [89], superfluidic turbulence [90], and dynamo [91]. The 2D flow analyzed in Chapter 4 can be considered as a linear combination of TG vortexes with different sizes and intensity.

The velocity distribution near x=0, y=0 point in the 2D case analyzed in the Chapter 4 is similar to the hyperbolic flow near stagnation point described by velocity distribution $u_x = \gamma x$, $u_y = -\gamma y$ (in the vicinity of the stagnation point $\sin x \approx x$, $\sin y \approx y$). In the [92], the hyperbolic flow created in Taylors four-roll mill is investigated. This work showed that above some critical Reynolds number $Re_c = 17$, the flow in unstable to three dimensional perturbation, and therefore periodic vortexes in the plane perpendicular to xy plane occur. Similar experimental results shown also in [93], [94]. This result is also theoretically obtained in [95]; the stability analysis is provided in [96].

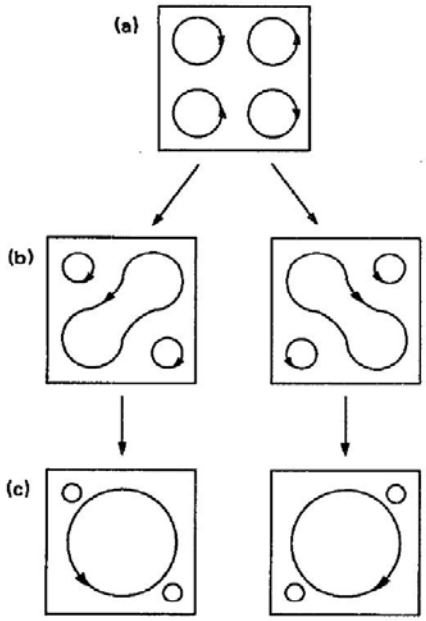

Figure 5.1: Sketch of Sommeria's experimental results [98]. a) stationary flow at low Reynolds numbers, b) stationary flow above the transition Reynolds number, and c) flow with spatiotemporal velocity fluctuations (high Reynolds numbers)

However, with the suppressing degrees of freedom in the plane perpendicular to the main flow plane, different instability can be obtained. One possibility is to use the stably stratified flow, where buoyancy is damping flow in vertical direction. Another way to suppress degree of freedom is to use shallow fluid layer.

Sommeria [97] analyzed the lattice of vertexes in horizontal liquid metal layer. The fluid was driven using the current between electrodes and applied vertical magnetic field. The important result of this work is the instability found in Taylor-Green vortex with the transition from four vortex to three vortex structure (see Figure 5.1). In general, this principle is applicable also for larger amount of vortexes. In Sommeria's work, the criteria for transition was R_h, which is the ratio between the bottom friction timescale and the turnover time. It was also found that hysteresis can occur for subcritical R_h numbers. However, it seems that this criteria is not universal; for example, in strongly stratified flows, the wall is not playing the role in this transition, and the bottom friction is insignificant.

In [99], it was shown that for any finite amplitude perturbation, there is a high enough Reynolds number at which the symmetry of TG flow will be broken. However, this statement does not say anything about the lower transition limit, that is, what is the highest Reynolds number at which any perturbation will be damped and flow

will be stable. The stability of TG vortexes is analyzed in more details in[98], [100].

In [101], vortex patterns under the influence of time-periodic forces is analyzed experimentally. It is shown that time-periodic forcing allows obtaining the vortex pattern similar to the Taylor-Green vortex pattern but slightly different from the pattern of steady forcing. The important result is obtained, which suggests that this intrinsically unstable vortex pattern can be stabilized when using time-periodic forcing.

The result of Sommeria is also in close connection with vortex merging topic. It is found that the merging of the vortexes proceeds in four phases: a diffusive stage, a convective merging phase when the vortex centers are rapidly pushed together, a brief second diffusive stage, and a final diffusion of the merged elliptic vortex [102]. In [103], it is shown that merging is very sensitive to the initial conditions, which is in agreement with the hysteresis at subcritical R_h values. Similar systems are often used as simplified models for inverse cascade of turbulence [104].

5.2 Numerical simulations of the transition

The transition was investigated in the configuration identical to the one described in Section 4.1.2, but at this time, no symmetry conditions were used so that the flow asymmetries can be found. Simulations were carried out in laminar steady-state regime.

At low forcing function magnitudes, flow is similar to the analytic solution obtained earlier, with four vortexes forming symmetrical velocity field Figure 5.2a. However, by increasing forcing function further, a sudden change in the flow structure appears, when some critical Reynolds number $Re_C \sim 100$ is reached 5.2b. These structures are similar to those shown in the work of Sommeria (see Figure 5.1). Further increase of forcing does not provide significant changes in the flow field (in laminar regime).

The direction of the rotation for the flow above Re_C is determined by the initial conditions in the simulation. Initialization of flow was performed with stream function $\pm\cos(2\pi x/L)\cos(2\pi y/L)$ – with opposite signs leading to opposite rotations. The initialization of solution with $\vec{u} = 0$ always gives the same rotation.

The vorticity ω_v in the central point of the domain is recorded to describe the transition quantitatively – in the four vortex regime, the vorticity in central point is 0, while in merged-vortex solution, it has obviously nonzero value. Taylor number based on the vorticity $Ta = \omega_v^2 L^4/\nu^2$ is used as a dimensionless quantitative value.

$\tilde{\omega}$	Re_G	Re	$F_{EM} \times 10^4$
2.5	1.08	87	1.94
10	1.40	95	4.44
40	1.3	106	16.65
100	0.43	150	59.63
160	0.48	160	106.01

Table 5.1: Summary of the obtained dimensionless numbers for case with highest subcritical Reynolds number

Reynolds and Taylor numbers are obtained in series of calculations by varying the forcing parameter at different shielding parameters $\tilde{\omega}$.

Taylor vs. Reynolds number data are plotted in Figure 5.3, where obvious tendency is visible that Re_C increases with increase of frequency. Taylor and Reynolds numbers were chosen with intention to eliminate the effect of forcing intensity in this characterization, and therefore, differences in Re_C with increase of frequency, can only be explained with the shape of the force distribution. As already shown in Section 4.1.2, the velocity gradient near the central point decreases with increase of frequency. This leads to assumption that shear stress is responsible for the initialization of vortex merging process.

To check this statement, gradient Reynolds number is introduced:

$$Re_G = \frac{\frac{\partial u_x}{\partial y}|_{x=0,y=0} L^2}{\nu}$$

However, no correlation between Re_G and transition between regimes is found. Table 5.1 summarizes dimensionless numbers for subcritical cases where highest Reynolds number was obtained; in other words, these numbers characterize the flow just below the critical Reynolds number. There is no obvious correlation between these data.

5.3 Experimental model of the Taylor-Green vortex merging

To find the transition Reynolds number experimentally, an experimental setup with PIV measurements in saltwater was designed. The proposed idea is to create $\nabla \times \vec{f}$ distribution similar to the one in equation 4.7 by means of applied current from electrodes and external magnetic field. Two concepts were proposed for this purpose, both shown in Figure 5.4. In the first concept (Figure 5.4a), the force density in the near wall region is perpendicular to the wall (therefore, this will be denoted as

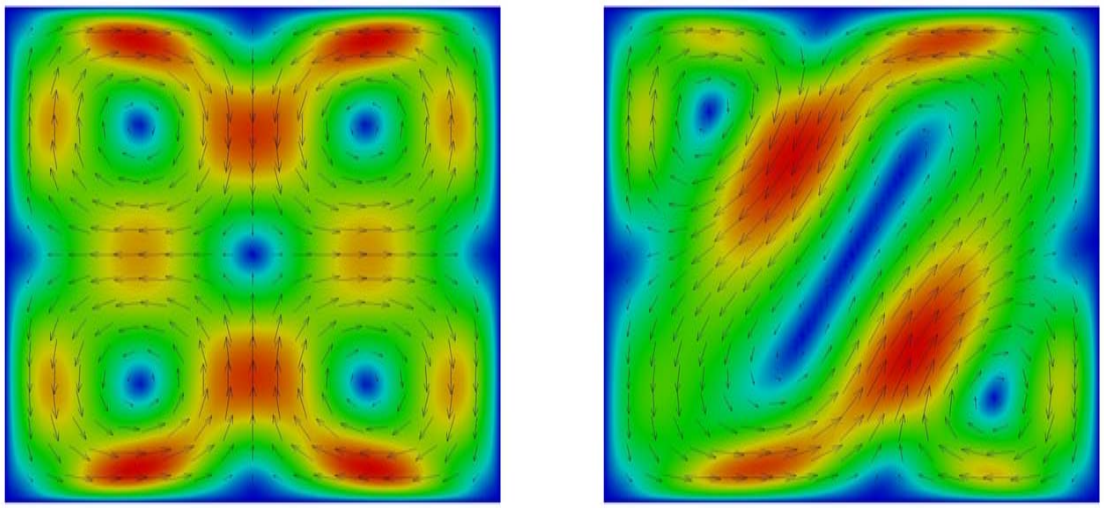

(a) $Re = 88.3$, $F_{EM} = 44.4$, $\tilde{\omega} = 10$ (b) $Re = 103.9$, $F_{EM} = 50.0$, $\tilde{\omega} = 10$

Figure 5.2: Two stable flows obtained below and above the critical Reynolds number.

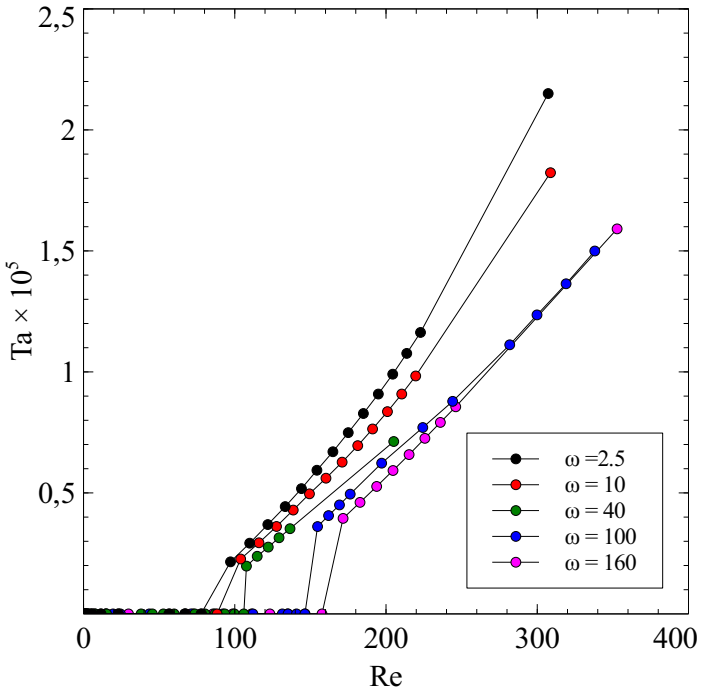

Figure 5.3: Taylor number vs. Reynolds number for 2D calculations with different shielding factor $\tilde{\omega}$

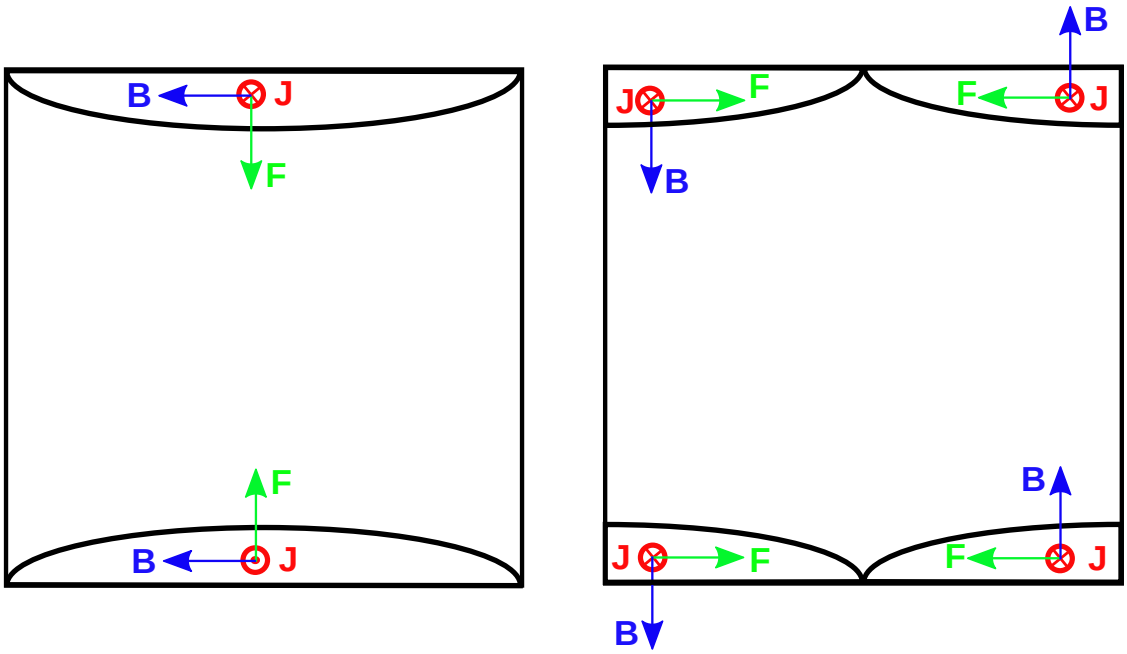

(a) "normal force" concept (b) "tangential force" concept

Figure 5.4: Proposed concepts for saline water model

"normal force" concept). For such purpose, magnetic field has to be in one direction in the whole near wall region; therefore, possible option is the use of Helmholtz coils.

For the second concept (Figure 5.4b), where forces are directed parallel to the walls ("tangential force" concept), magnetic field needs to have opposite directions in the near wall region on different ends of the electrode. For this reason, more complex magnetic field creation is necessary (described later in text).

Both concepts were built and experimentally tested. Tangential force concept was chosen, as it requires smaller force density to create same $\nabla \times \vec{f}$ magnitude, and thus, higher velocities can be achieved. In case of tangential force, $\nabla \times \vec{f} \sim F_{MAX}/\delta$, while for normal force, $\nabla \times \vec{f} \sim F_{MAX}/L$. At skin depths, much smaller than container size tangential force will always give more effective stirring. Another reason to choose tangential force concept was the visibility of the fluid – arranging both coils close to each other was not possible because it would disturb the visibility of saltwater. The increase of distance between coils would enhance visibility, but it would also lead to significant decrease in the magnetic field intensity in the test section.

The designed setup is a Plexiglas container with inner dimensions of 100 mm $\times$ 100 mm $\times$ 15 mm (see Figure 5.5). The AC voltage is applied on two pairs of stainless steel electrodes; distance between electrodes is 10 mm. The magnetic field is created externally using two coils with inner diameter of 170 mm and 400 copper

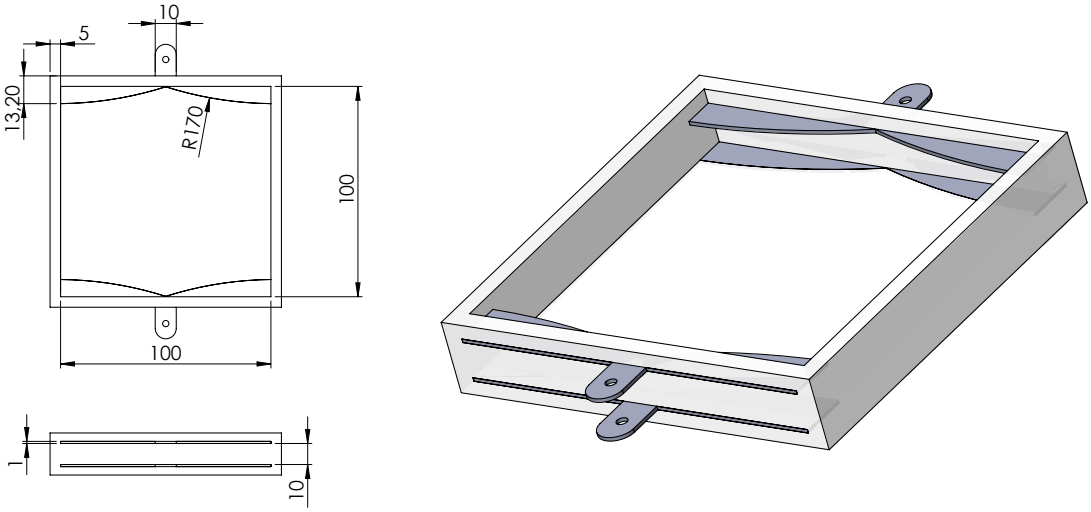

Figure 5.5: The saline water Plexiglas container design. Cross sections with corresponding dimensions shown on the left. Isometric view – on the left side

windings with 1 mm wire diameter. Coils were not specially designed, existing coils at the Institute of Electrotechnology were used; therefore, the Plexiglas model and magnetic field guides were only freely variable design parts.

The magnetic field guides were arranged like shown in Figure 5.6, where blue lines and arrows show principal magnetic flux lines. In the region between electrodes magnetic field density up to 28 mT was achieved (measured value). This value was achieved at the $9A$ current in coils. Higher values were not possible because coils were not water cooled, and long operations would cause coil damage.

The saltwater was produced using table salt, 15% wt solution was used. To estimate the electrical conductivity of the solution, voltage-current characteristic was recorded on the electrodes of the setup (Figure 5.7). The found resistance of the saltwater between two neighboring electrodes is $R = 1.9\Omega$, which corresponds to the electrical conductivity of the salt water $\sigma = 9.7S/m$. The number given in literature for 15% wt sodium chloride solution is $17.2S/m$ [105]. The electrical conductivity is evaluated using relation $R = l/\sigma A$ (l is distance between electrodes, A is area of the electrode). There is a number of possible errors in this estimation. An assumption is used that electrical current flows only in the space between electrodes. In reality, the effective area is larger, and therefore, estimated value is larger than real electrical conductivity.

The electrical conductivity value is important in simulations only to estimate the heating of the water and effect of buoyancy forces on the flow. The measured value is used in numerical simulations.

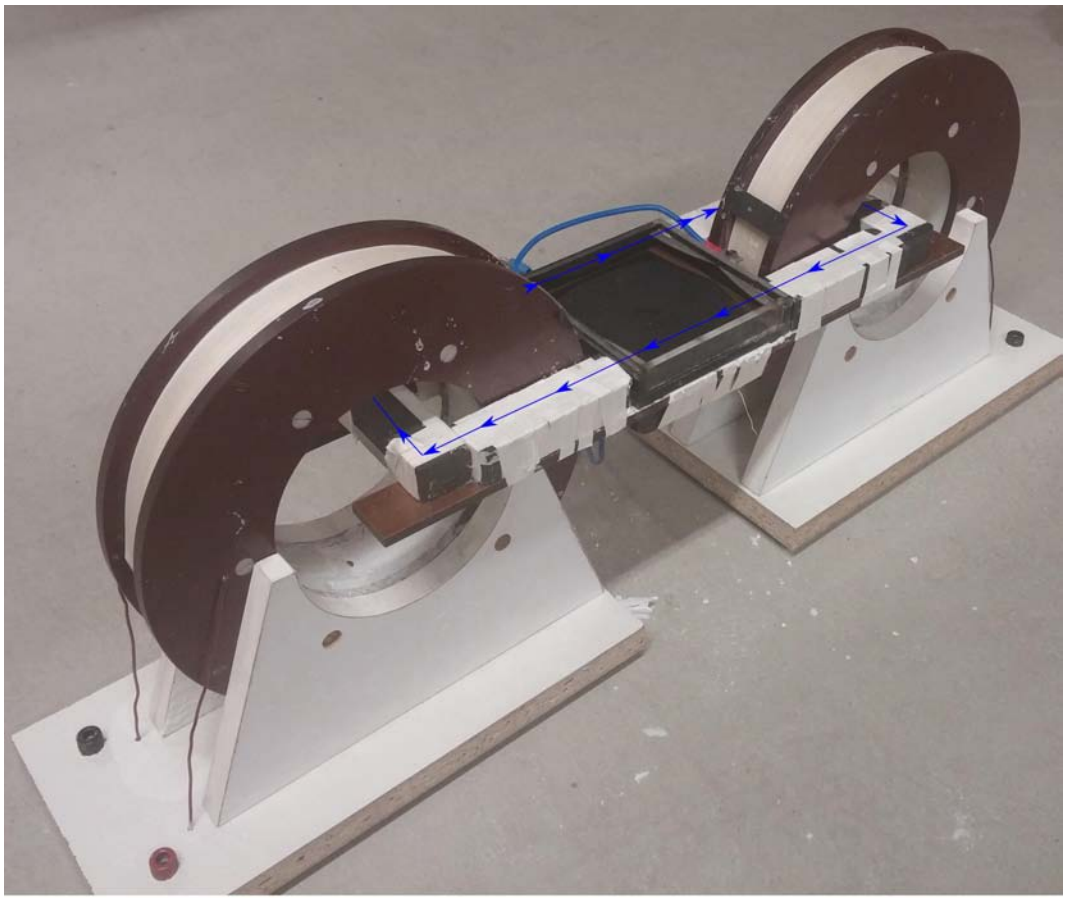

Figure 5.6: The assembled Plexiglas model with coils for magnetic field. Blue line with arrows shows principal magnetic flux lines

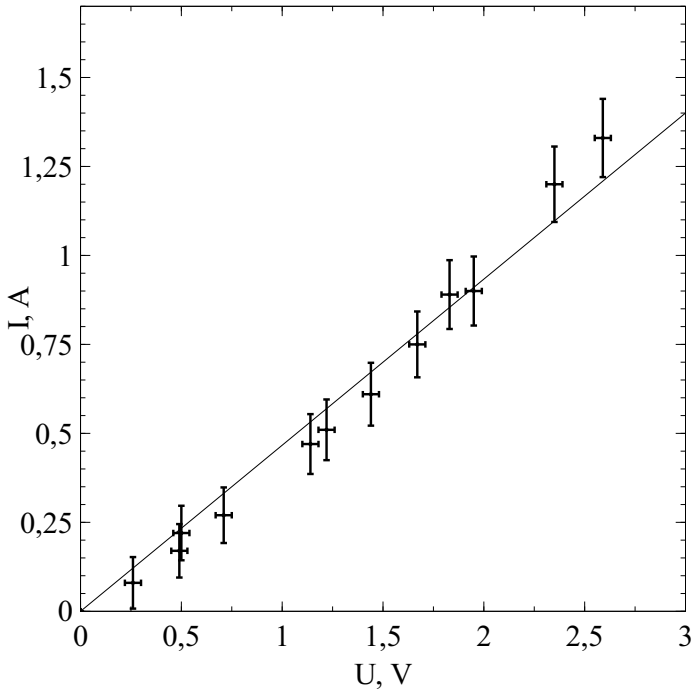

Figure 5.7: Current-voltage characteristic measured on the electrodes of the salt-water model. The slope $R^{-1} = 0.53\Omega^{-1}$

5.3.1 Self-made PIV

The commercial particle image velocimetry (PIV) equipment offers good possibilities of measuring velocity in different transparent fluids with different time and space resolutions. However, these systems are usually very expensive (tenths of thousands of Euros), mostly due to sophisticated high-speed cameras and lasers.

For the current application, main task is to find the critical Reynolds number for vortex merging and to show that such approach has potential in investigation of body force driven flows. 2D simulations showed that $Re_C \approx 90$. Simple estimations show that for 10 cm $\times$ 10 cm saltwater model, the velocities will be in the range of several mm/s; thus, space and time resolutions required for the measurement of velocity will be possible to meet using digital single-lens reflex camera. Canon 350D camera was used with Canon EF 50 mm f/1.8 II lens. The experiment with triggered camera shooting the running stopwatch showed that this camera was able to shoot two images with $\Delta t = 0.4$ s with precision ± 0.03 s. Due to relatively large error, the largest possible Δt was used for each case.

To illuminate the particles in the plane, 650 nm 200 mW Red Laser Line Module with 60° lens was used. It was found that 200 mW was enough to illuminate particles in this small setup (10 cm $\times$ 10 cm). Although the laser is not powerful in comparison

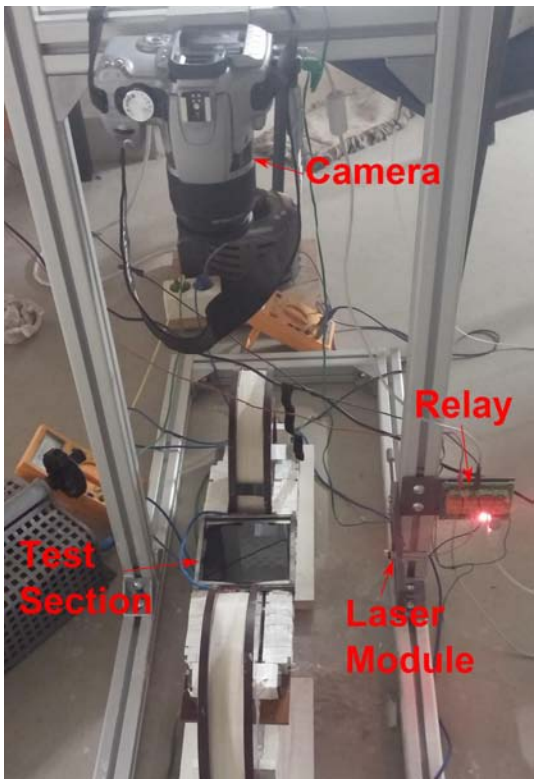

Figure 5.8: PIV arrangement and salt water test section.

to lasers used in PIV, it is not able to work continuously for more than 10 seconds due to overheating; therefore, it was also triggered along with the camera shutter.

The triggering of camera and laser was performed using KMTronic USB relay. Full arrangement of experimental model and PIV measurement system is shown in Figure 5.8. The post processing of the results was performed using open software PIV package for MATLAB – openpiv (www.openpiv.net). The spatial resolution of the final velocity field was 3.4 mm. This number was limited due to speed of the camera . At the velocity of the order of magnitude 5 mm/s and the image pair time difference $\Delta t = 0.5$ s, the movement of the particles was in the range of 2.5 mm.

5.3.2 Results of PIV measurements and simulations

Table 5.2 summarizes the PIV measurements and their corresponding parameters. The magnetic field is related to the current in coils I_C with experimentally found expression $B[mT] = 3.11 I_C[A]$.

Simulation of EM field is performed using ANSYS software, and fluid flow is calculated using ANSYS CFX. The curl of force in numerical simulations (Figure 5.9) showed certain similarity with the one assumed in Section 4.1.2. However, there

Case	I_C, A	I_M, A	N	Δt, s	U_{max}, mm/s
PIV1	4.0	0.4	50	0.8	1.4
PIV2	5.0	0.5	50	0.6	3.1
PIV3	6.0	0.6	50	0.5	4.7
PIV4	8.0	0.6	50	0.5	5.5
PIV5	8.0	0.7	50	0.4	6.3
PIV6	9.0	0.7	50	0.4	7.2

Table 5.2: Parameters of the PIV measurements. I_C is current in coils, I_M is current in water model, N is number of image pairs taken.

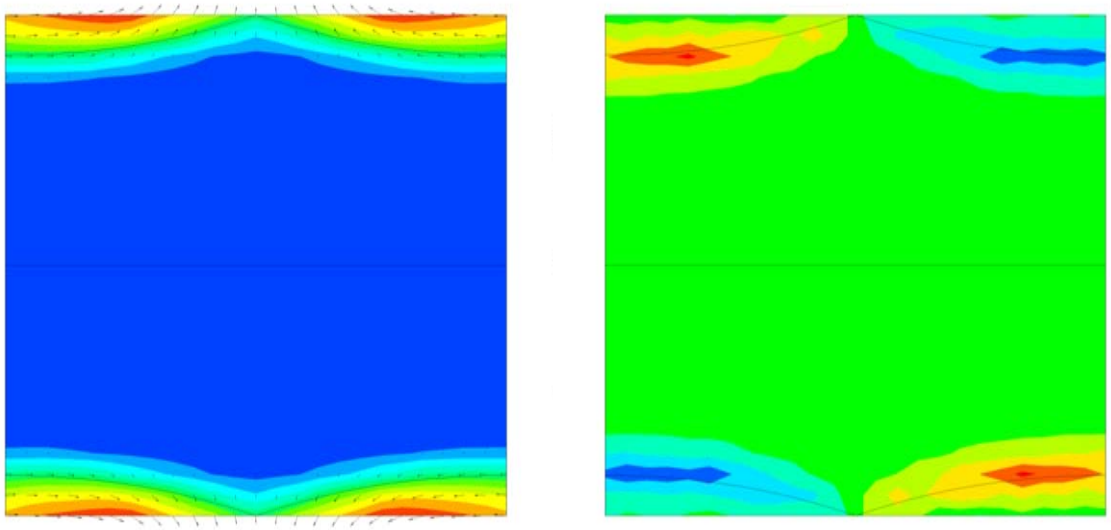

(a) $\vec{f}$ (b) $\nabla \times \vec{f}$

Figure 5.9: Force and curl of force distribution in the horizontal cross section, simulation results

is one significant difference – the highest force gradient is located directly under the edge of electrode, where highest current decrease in the direction away from wall is expected.

The fluid flow simulations showed vortex merging at the Reynolds number $Re_C \approx 210$ (Figure 5.10), which is slightly below the $Re_C \approx 250$ found in experimental measurements.

The comparison of PIV and CFD results on two lines (L1 - Y=-5 mm, L2 - Y=-20 mm) is shown in Figure 5.11. Good agreement is found on all presented lines for both regimes. Significant differences are present between coordinates X=0 mm and X=30 mm in both curves for case with merged vortexes. At this location, some artifacts can be seen in velocity plot in Figure 5.12b.

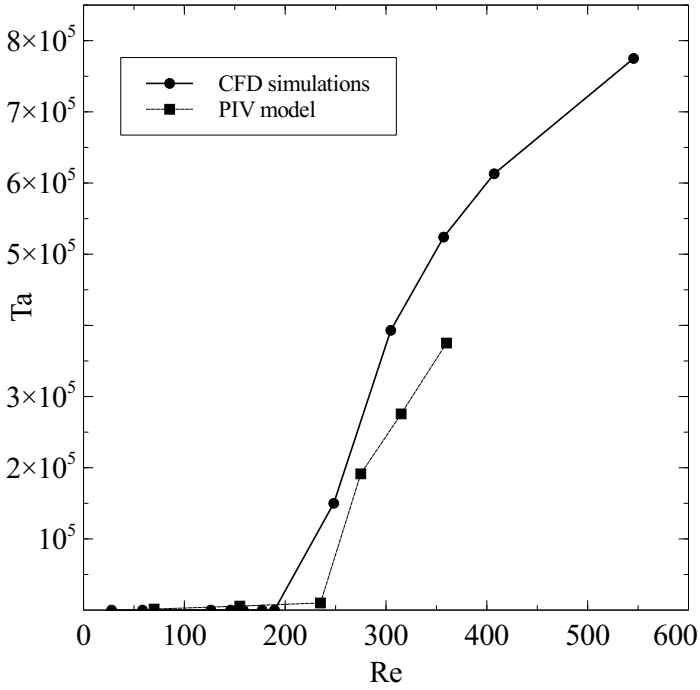

Figure 5.10: The modified Taylor number vs. Reynolds number plot in CFD results and in PIV measurements

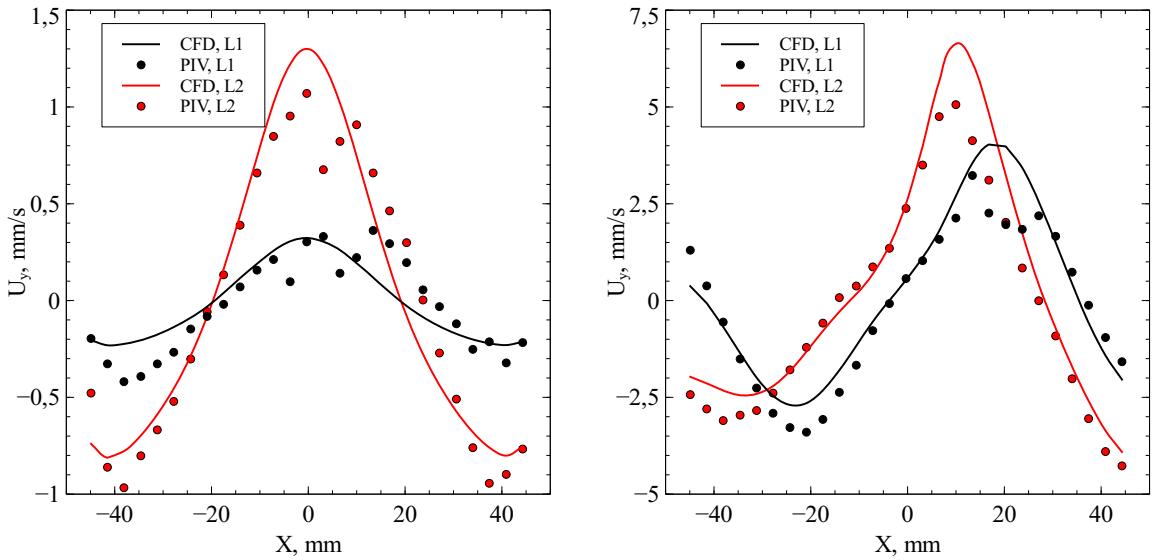

(a) $Re = 70$ (b) $Re = 275$

Figure 5.11: Comparison of the Y velocity component in PIV and CFD results on lines L1 and L2

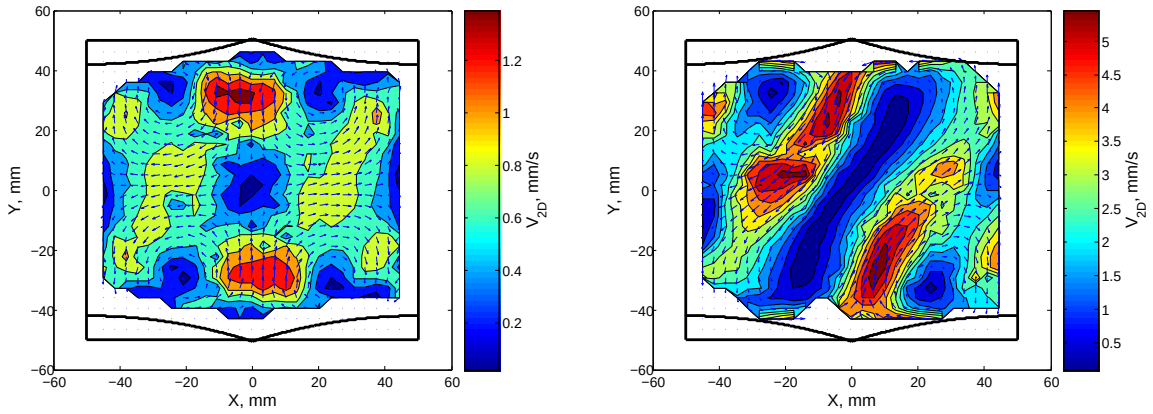

(a) $Re = 70$ (b) $Re = 275$

Figure 5.12: Two stable flows obtained below and above the critical Reynolds number

The 2D velocity distributions obtained in the PIV measurements for both flow regimes are shown in Figure 5.12. Slight asymmetry of the flow is visible in the sub-critical case (Figure 5.12a), which is most likely connected with imperfect symmetry in the experimental setup. Asymmetry of the setup was also proven by the results in the flow with merged vortexes (Figure 5.12b): the rotation of the largest vortex was always counterclockwise (with respect to coordinates in Figure 5.12). Even in cases when manual stirring with clockwise rotation was applied, after certain transition time, flow always ended up rotating counterclockwise. This fact is not in the agreement with simulation results, where initial conditions determine the direction of rotation.

5.3.3 Limitations of electrolytes as model fluids for liquid metal MHD

If the force density in the electrolyte model is the same as in the liquid metal equipment, the results from one can be transferred to another by using scaling laws. In practice, this is not the case, as only certain degree of similarity can be achieved.

The only benefit of using electrolyte as model is the transparency that allows using PIV or other optical methods for velocity measurements. The use of electrolyte is limited due to creation of gas bubbles during electrolysis process. The critical value of current was found when too intensive gas bubble creation did not allow using PIV. For DC current it was 0.25 A which corresponds to $j = 460$ A/m^2, for AC - 0.75 A or $j = 1,380$ A/m^2. Figure 5.13 shows a photo obtained in PIV with $j = 1,600$

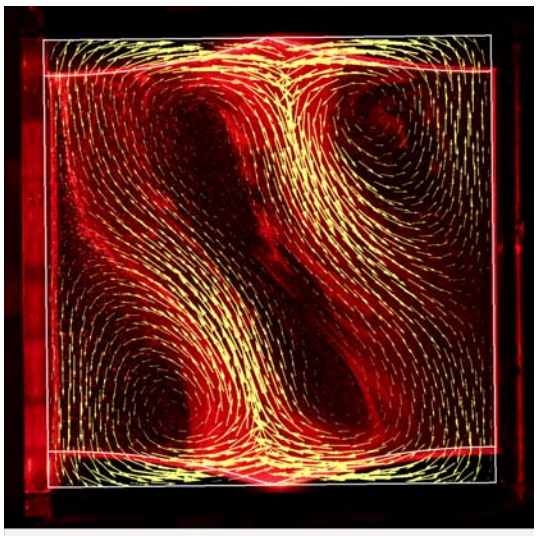

Figure 5.13: Photo obtained in PIV measurements with $j = 1,600$ A/m^2. Yellow vectors show the flow field in simulation results

A/m^2. Such photo is not usable for PIV; however, it shows very clearly the vortex structure in the flow. Yellow vectors overlaying the photo are obtained in simulation, good agreement is visible.

Due to current density limitations, the force density can be mostly influenced by magnetic field. In used setup maximal magnetic field density was $B = 20$ mT. With specially designed coils, this number might be increased up to 10 times.

The increase of geometrical size would allow increase in Reynolds number. Assuming three times increase (30 cm $\times$ 30 cm $\times$ 3 cm), would still be relatively compact system and will require 2.7 liters of water and approximately 500 grams of table salt. Since the main interest consists in the turbulent regime, $Re \sim \sqrt{F_0}$ can be assumed. Assuming force density magnitude does not change, one can obtain $Re \sim L^{3/2}$; thus, with three times increased linear size, Reynolds number will be increased 5.2 times. With the increase of magnetic field 10 times, the current setup with Reynolds number of 200 can be scaled up to $Re = 10,400$, which can already be considered as a turbulent flow.

In this chapter it was shown that electrolyte can be used as model fluid for liquid metal problems in certain cases. However, this approach is limited to isothermal fluid investigations only. Due to large differences in Prandtl number, water cannot be used as model liquid for thermal process. Another important difficulty in this approach is that finding proper magnetic field and electrode configurations is not straightforward for most liquid metal applications. For instance, it is very hard to imagine such model for cylindrical induction crucible.

Chapter 6

Experimental Measurements in Directional Solidification Model Setup

This chapter presents results of experimental measurements in Wood's alloy with and without presence of vertical temperature gradient to find influence of buoyancy forces on flow field. The results described in this chapter will be used for numerical model validation in the next chapter.

6.1 Temperature measurements in the stratified flow

The temperature measurements were performed using 0.5 mm K-type thermocouples. The time response curve for these thermocouples after immersion in Wood's alloy was recorded, and the resulting time constant was 100 ms. Temperature data in measurements were collected by Delphin Expert Key 100L data logger, which allows sampling rate up to 100 kHz. Temperature data were recorded with 2 Hz frequency.

6.1.1 Change of mixing regime near Ri_{CR}

The important effect of stratification is the damping of vertical motion, including vertical turbulent heat and mass transport. This phenomena was observed in the following experiment: at constant top heater power, EM forcing was turned on with different intensity (current I in windings) every time from the same initial conditions (fluid at rest, fixed heater power Q). For presentation of results, normalized vertical temperature difference is defined as follows:

$$\Delta\widetilde{T} = \frac{A\lambda\Delta T}{LQ}$$

Figure 6.1 shows $\Delta\widetilde{T}$ dependence on current I/I_{CR} in the windings. I_{CR} is a critical current at which Richardson number becomes smaller than unity, and turbulent mixing prevails. Vertical temperature difference slightly decreases with growth of I also below I_{CR}. This fact can be explained with the increase of turbulent pulsations and thus turbulent heat conductivity. The case with highest heater power has also highest critical EM force, and therefore, in this case, most intensive decrease in $\tilde{\Delta}T$ is observed below critical current.

As the current goes to zero, the normalized temperature tends to the asymptotic value $\Delta\widetilde{T} \approx 0.5$. This value is explained with the fact that only half of the power from heater flows through the melt in vertical direction. The rest are losses through the lid and walls.

When current reaches I_{CR}, the velocity-shear driven vertical turbulent motion is no longer damped by buoyancy forces, and the flow pattern changes from a stratified quasi two-dimensional wave-dominated pattern to a three-dimensional chaotic strongly turbulent regime [106]. Ri_{CR} corresponding to data in Figure 6.1 can be seen in Figure 6.2. The dependence of velocity on inductor current was assumed to be $U \sim I$ for inertia dominated flows, which is well-known result from cylindrical induction crucibles [82], and it is also shown in Chapter 4. With this assumption, Ri was calculated using the following estimations: $S^2 = U^2/H^2$, $N^2 = g\beta\Delta T/H$.

The vertical effective heat conductivity λ_{eff}, which allows to estimate the influence of fluid motion, defined here using assumption that total vertical heat flux is constant – ${}^{\lambda_{eff}}/_{\lambda} = {}^{\Delta T_0}/_{\Delta T}$. λ is molecular conductivity, ΔT is vertical temperature difference, and ΔT_0 is vertical temperature difference without mixing (generator off). In such definition, effective heat conductivity has impact of molecular, turbulent, and convective heat transport. ${}^{\lambda_{eff}}/_{\lambda}$ ratio appears to be much higher than unity (Figure 6.2) in purely turbulent regime. On the other hand, in strong stratification regime ($Ri \gg 1$), only molecular heat conductivity is present ($\lambda_{eff} \to 1$ as $Ri \to \infty$).

The critical Richardson number Ri_{CR} in the investigated case is reasonably higher than 1, which is standard threshold for shear flows. One reason for difference is the calculation of Ri, which is based on global, not local, values and limited applicability of this definition for flows with vertical flow component. Second possible reason is different character of flow. If buoyancy forces are not present, the flow in investigated system tends to form toroidal vortices, while shear flows are mainly horizontal also at

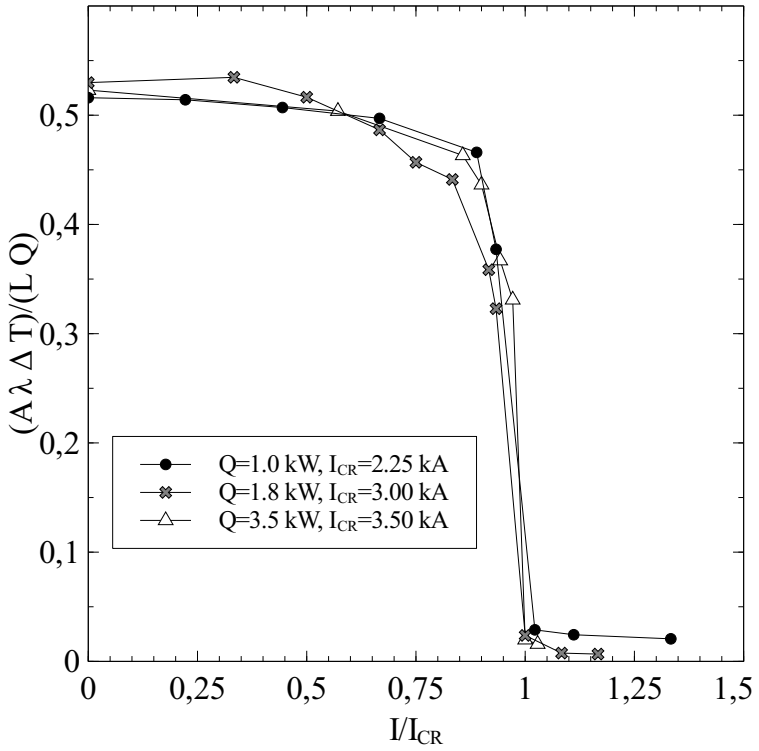

Figure 6.1: Vertical temperature difference dependence on current in windings

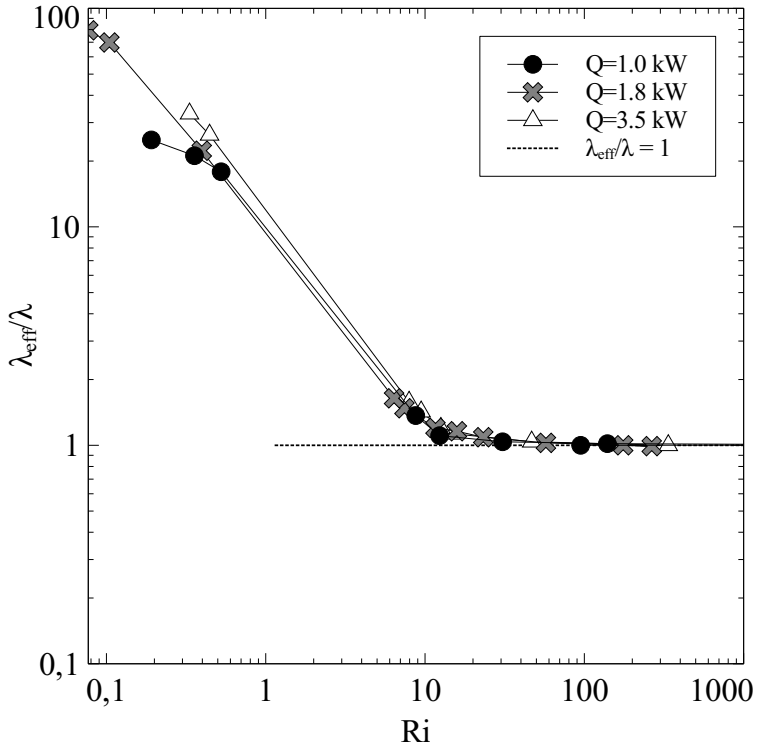

Figure 6.2: λ_{eff}/λ ratio dependence on Richardson number for different heater powers. All curves asymptotically reach 1 as $Ri \to \infty$

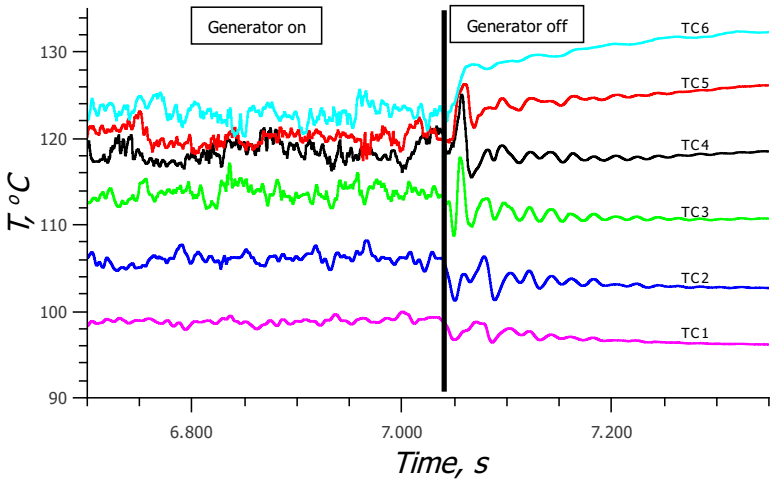

Figure 6.3: Temperature time series at different locations after turning off the generator. $Ri = 11.8$. The thick vertical line shows time of turning off

small Ri. In case of shear flows, the threshold is between two mixing regimes, while in investigated setup, it is also between two different mean flow structures.

6.1.2 Transition after turnoff

One of the phenomena in stratified fluid known from textbooks is the existence of internal waves (buoyancy waves). The fluid parcel displaced in stably stratified media oscillates with angular frequency N (Brunt-Väisälä frequency). The temperature oscillations of such nature are observed in present experimental model. For flow with high $Ri = 11.8$ and EM forcing on, generator is turned off at certain time, thus allowing the flow to slow down. At turnoff moment (t=7,040 s in Figure 6.3) temperature temporal evolution character changes rapidly from fast, turbulent, and chaotic to slower wave-like pulsations. The buoyancy frequency corresponding to this case is $N = 0.53$ Hz, while the spectrum analysis of the measured oscillations during first 200 s after turnoff gives value of $\omega = 0.44$ Hz. As both values almost match, the temperature oscillations seem to represent buoyancy waves. It is also important, that mean vertical temperature gradient increases steeply immediately after turnoff, then more slowly due to thermal conduction. Such rapid temperature gradient increase after stop of forcing can be explained by conserved potential energy in fluid layers during mixing, release of which causes buoyancy waves. The latter are then dissipated into heat by viscous forces.

During stationary process, there must be equilibrium between generated and dissipated turbulence kinetic energy (TKE). TKE is generated by shear; dissipation in

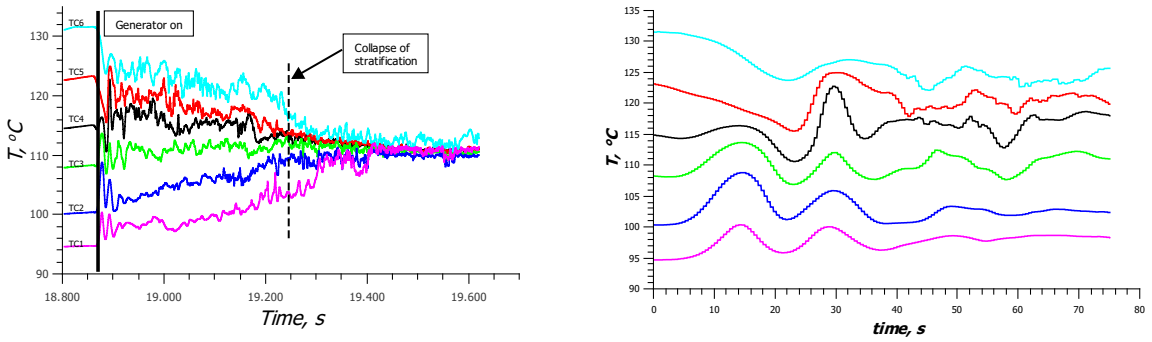

(a) Full process of collapse

(b) First 75 seconds after turn-on

Figure 6.4: Collapse of stratification for current in the inductor $I = 3.0$ kA and heater power $Q = 1.8$ kW

3D turbulent flows is due to viscous forces. In stratified flows, some part of TKE is, however, transferred into turbulence potential energy (TPE), which produces buoyancy waves. Obviously, these waves are not observable due to superposition with shear-generated turbulence, but energy exchange between TKE and TPE is of high importance for proper description of stratified turbulence as shown in [106].

6.1.3 Collapse of stratification

Other transition happens after turning on the generator at the inductor current close to the critical I_{CR}. Figures 6.4 and 6.5 show the collapse of stratification after turn-on for two cases – $I = 3.0$ kA, $Q = 1.8$ kW and $I = 3.5$ kA, $Q = 3.5$ kW respectively. It is noteworthy that at these parameters collapse proceeded in two stages. First, the temperature differences between TCs decrease due to turbulent mixing that increases effective heat conductivity. This continues for approximately 380 s in Figure 6.4 and 1,970 s in Figure 6.5 until the situation appears when buoyancy forces are insufficient to retain stratification. As this happens, strong mixing takes place, and the temperature in whole fluid volume becomes nearly homogeneous (within approximately 50 s and 200 s, respectively). In case if higher current is used, there is only fast stage in the collapse – the turbulent pulsations at the beginning are high enough to dominate over buoyancy forces.

The difference in the mixing times might seem unexpected, because the forcing is stronger in the second case. However, near critical point I_{CR} two-stage collapse is very sensitive to the current in windings and initial temperature difference $\Delta T = T_{TC6} - T_{TC1}$. For example, experiments with $Q \approx 1.8$ kW heater power near $I = 3.0$ kA current have shown that initial temperature difference of $\Delta T = 34$ K would lead

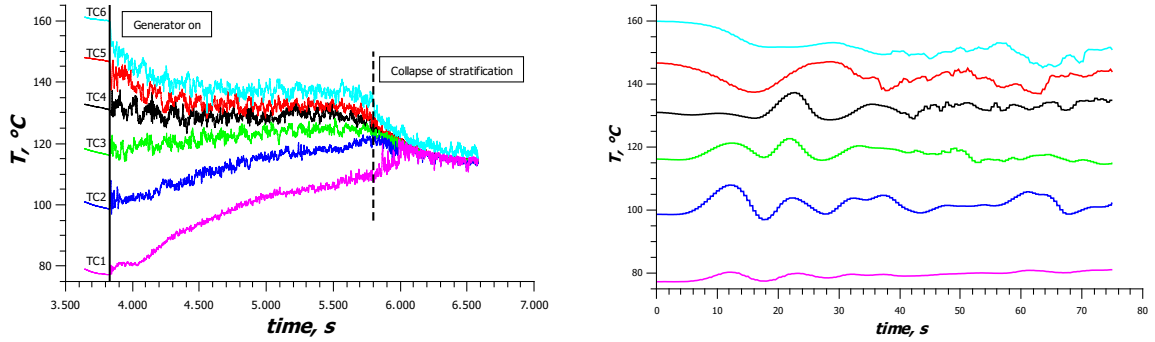

(a) Full process of collapse

(b) First 75 seconds after turn-on

Figure 6.5: Collapse of stratification for current in the inductor $I = 3.5$ kA and heater power $Q = 3.5$ kW

to two-stage collapse, but $\Delta T = 37$ K to stable stratification (no collapse occurs). More precise setting of the temperature difference is not possible due to very large time constant ~ 20 min and due to some drift in experimental values.

The current in this setup can be set with precision up to $50A$. The error is mostly due to the properties of the transformer, which is not water cooled and therefore has some drift in output current during long measurements. The precise thermal conditions are barely repeatable. The temperature difference values at constant heater power are drifting within ± 3 K. The reason for that is non-steadiness of the heating; even precise setting of heater power and bottom cooling flow rate leads to slow rise or decrease of the average temperature with the speed of ~ 5 K/h.

At the very first moments after turn-on (Figure 6.4b) two to three periods of waves appear. The nature of these waves is likely connected with the buoyancy waves. Although the buoyancy period $\tau_b = 2\pi/N$ estimated from the experimental results during first two to three pulsations is always 30%-40% higher than theoretical value for corresponding temperature gradient, one can conclude that the periods of these pulsations are related to vertical temperature difference as $\tau_b \sim \Delta T^{-1/2}$, which is in agreement with theory. Figure 6.6 shows the temperature pulsations directly after turn-on (t=0) measured by the thermocouple TC2 for different heating/mixing parameters. Temperature dependency is scaled with respect to τ_b (theoretical, based on the initial temperature difference), all the parameters are depicted in the label of the figure. One can see that the character of the time dependence during first pulsations is very similar for all cases. Similarity is less pronounced for case below the critical current ($I = 3.3$ kA, $Q = 3.5$ kW). For currents that are more than 20% lower than I_{CR}, the pulsations at the turn-on are not observed due to significant

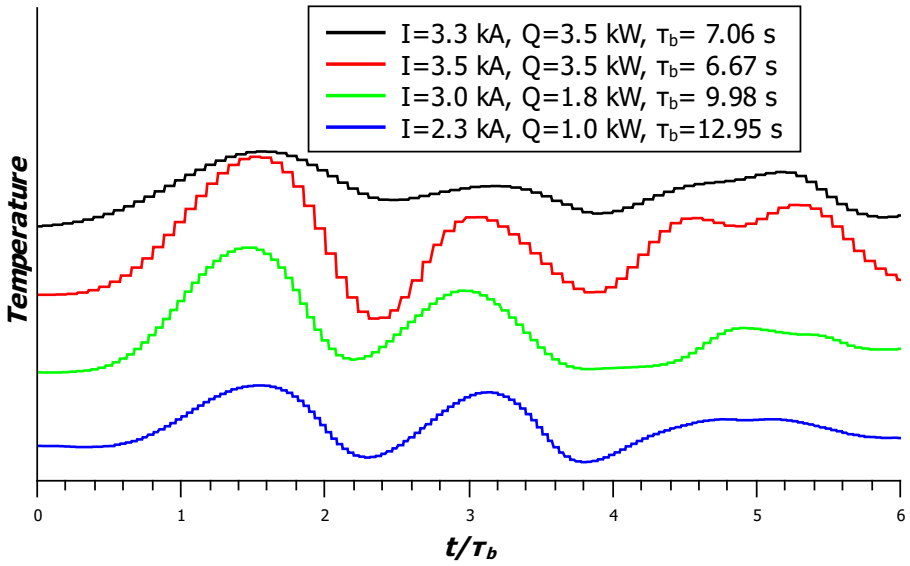

Figure 6.6: Temperature pulsations measured by the thermocouple TC2. Temperature dependency is scaled with respect to τ_b

buoyant damping forces.

6.2 UDV measurements

6.2.1 Measurement description

The measurements of velocity were performed using 10 mm ultrasonic probe (see Figure 6.7) through the steel wall for isothermal and stratified flows. Measurement principle is shown in Figure 6.8; they are always done through the left wall. A coordinate system is introduced for convenience with (X,Y)=(0,0) point located in the middle of crucible. Third, Z axis has 0 point at the bottom of the crucible. Ranges for all coordinates in the melt are X=-210...210 mm, Y=-210...210 mm, Z=0...120 mm.

The measurements through the wall were limited to two horizontal planes (Z=80 mm and Z=30 mm) and one vertical plane (Y=0 mm) due to presence of windings.

All the measurements are summarized in the table 6.1. The time step between measured profiles was 200 ms, total 1,500 profiles were recorded for each data set, thus averaging time was 300 seconds.

The measurements in planes are done on several lines and then reconstructed into planar distribution in MATLAB software. Measurements in Z=80 mm plane consisted of 11 lines, and measurements in Y=0 plane of 6 lines. No measurements

Figure 6.7: 10 mm high-temperature ultrasonic probe from Signal Processing SA

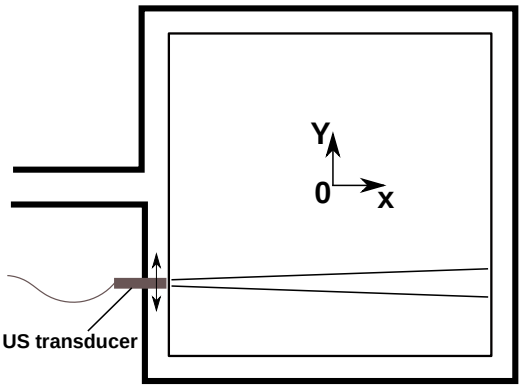

Figure 6.8: Ultrasound probe location in measured system. It can be moved along the wall to measure velocity profiles in different locations

Case	ΔT, K	I, kA	Location
E1	0	1.5	Y=0 mm plane
E2	0	2.5	Z=80 mm, Y=0 mm planes
E3	40	2.1	Z=80 mm, Y=0 mm planes
E4	40	2.5	Z=80 mm planes
E5	0	0–4.5	U(I) at (Y, Z)=(0 mm, 80 mm) line
E6	80	0–4.5	U(I) at (Y, Z)=(0 mm, 80 mm) line
E7	40	2.1	Z=30 mm plane

Table 6.1: Experimental measurement cases. ΔT is temperature difference between thermocouples TC6 and TC1.

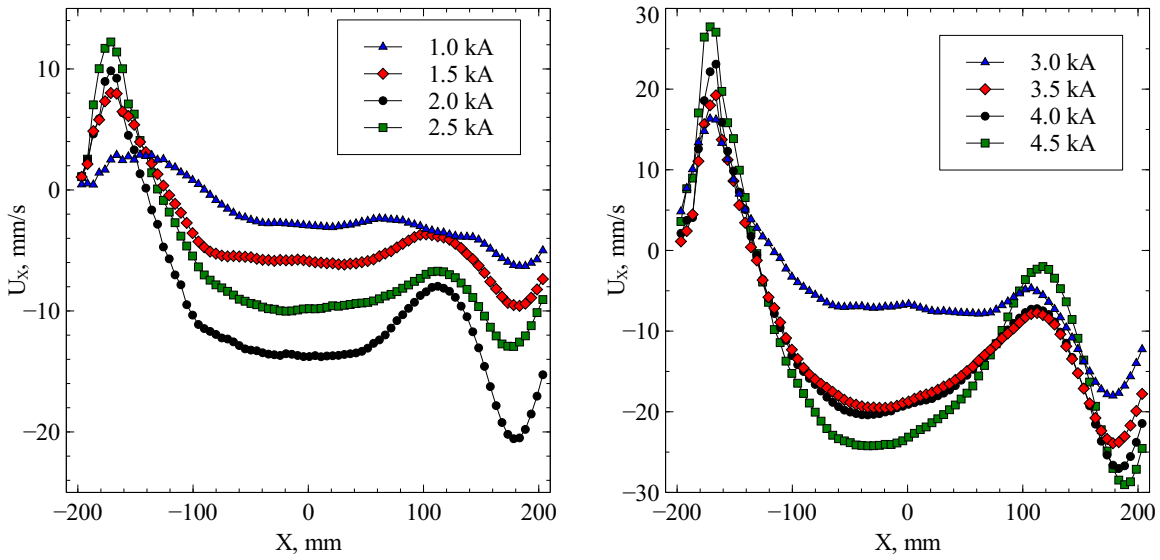

(a) I=1.0...3.5 kA (b) I=3.0...4.5 kA

Figure 6.9: U_X velocity distribution on the line (Y, Z)=(0 mm, 80 mm), isothermal flow

were performed near walls, but velocity is set to 0 in graphical representations of results in planes.

6.2.2 Isothermal measurements

The velocity measurements along one horizontal line with different currents in windings showed the development of the velocity profile with the increase of current (Figure 6.9). At small currents (Figure 6.9a, $I = 1.0$ kA), the velocity peak nearest to the probe (X=-210 mm) is wider (approximately 100 mm wide), and peak value reaches 3 mm/s. At the $I = 1.5$ kA current, the velocity peak gets narrower (approximately 60 mm). Further increase of current does not show significant change in the velocity profile shape, except highest currents, $I = 3.5...4.5$ kA, where velocity distribution shape in the middle part of the profile (X=-100...100 mm) becomes more curved.

Obtained profiles are not symmetrical with respect to the X=0 mm point, which can be explained with asymmetry due to the inductor connectors – the force on the connector side is smaller than on other edges of the crucible.

Characteristic velocity dependence on the current in windings is shown in Figure 6.10. For isothermal flow, maximal value in the near-wall peak is depicted. For stratified flows, averaged value over whole profile. This is done due to the change in the flow structure at $I = 3.5$ kA for stratified flow (see further in text). Linear

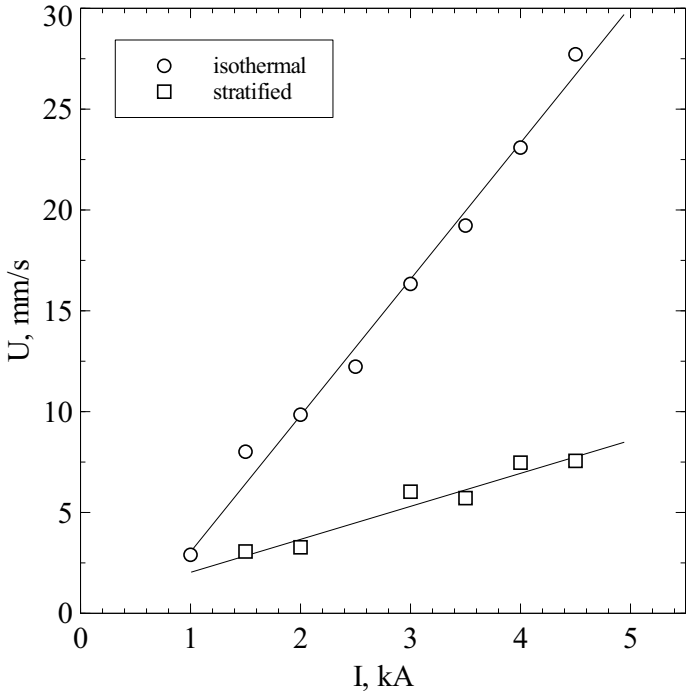

Figure 6.10: Velocity dependence on current in windings. Peak value used in isothermal case. In stratified flow, average over profile

dependence is obtained in both cases. For isothermal flow, dependence is $U[mm/s] = -3.72 + 6.76 \cdot I[kA]$. For stratified flow, the slope is less steep because of averaging: $U[mm/s] = 0.39 + 1.64 \cdot I[kA]$.

To obtain 2D planar distribution of the X velocity component, showed in Figure 6.11a, measurements were performed on 6 lines in the plane Z=80 mm. For this distribution only half of the crucible was measured. Mirrored data are shown in the plot. Obvious tendency is visible that fluid is moving towards the center of the crucible in this cross section – in the left part velocity X component has positive values (motion in the positive X direction), while in the right part of the figure, velocity has negative values (motion in negative X direction). No symmetry with respect to the X=0 mm line is observed. The flow is moving in the negative X-axis direction in the central part (X=-100...100 mm, Y=-50...50 mm) of the cross section. As already mentioned, this is connected with inductor connectors that cause smaller EM forces on the left side of the crucible.

In vertical cross section (Y=0 mm), plane measurements consist of six profiles. One vortex is present in this plane on each side of the crucible (Figure 6.11b), in which fluid is moving away from the wall in upper part of the crucible and towards the wall near the bottom. Again, the symmetry with respect to the line X=0 is weakly

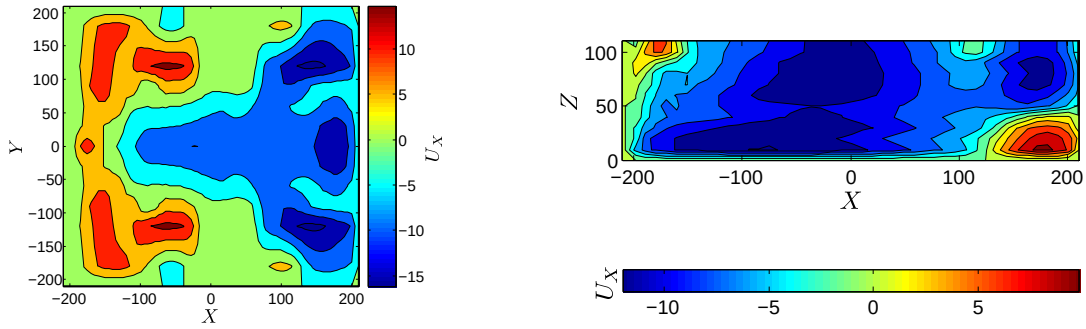

(a) Z=80 mm (b) Y=0 mm

Figure 6.11: U_X velocity distribution in the Z=80 mm and Y=0 mm planes for isothermal case. U_X defined codirectionally with X-axis - positive velocity means fluid moving to the right and negative to the left

pronounced, in most part of this cross section, fluid is moving in the $-X$ direction. This result is consistent with results on $Y = 0$ mm line in horizontal cross section (Figure 6.11a).

Figure 6.12 shows velocity signal time dependence for two different current values – 2.5 kA and 4.5 kA. Low-pass filter with cutoff frequency 1.0 Hz is applied to these data. It is clearly visible how amplitude of pulsations increases in the case with higher current, as well as velocity mean value. Pulsations are better visible in the zoomed velocity-time dependence (Figure 6.12b), where significant peaks are detected approximately every 5-10 seconds. It is noteworthy that large-scale pulsations of similar periods are present in both cases, but no pulsations of shorter periods are present. This fact is likely connected with the sampling volume of UDV. By using Taylor's frozen turbulence hypothesis (equation (2.31)), one can estimate cutoff frequency as

$$f_c = \frac{\bar{u}}{2\pi \cdot 2d} \tag{6.1}$$

Here, d is diameter of the ultrasonic beam. For mean velocity of $\bar{u} = 20$ mm/s the cutoff frequency is 0.16 Hz, which corresponds to period of 6.3 seconds. This explains why no pulsations with shorter periods are detected.

The autocorrelation function (Figure 6.13) of velocity signals does not reveal any strongly pronounced periodicity of the flow. Small peaks appear in 40–80 seconds range for flow with $I = 4.5$ kA.

Turbulence energy spectral density obtained from the autocorrelation of velocity signals is shown in Figure 6.14. This graph clearly illustrates inability of UDV technique to resolve the smallest turbulent eddies – the cutoff wavelength does not allow

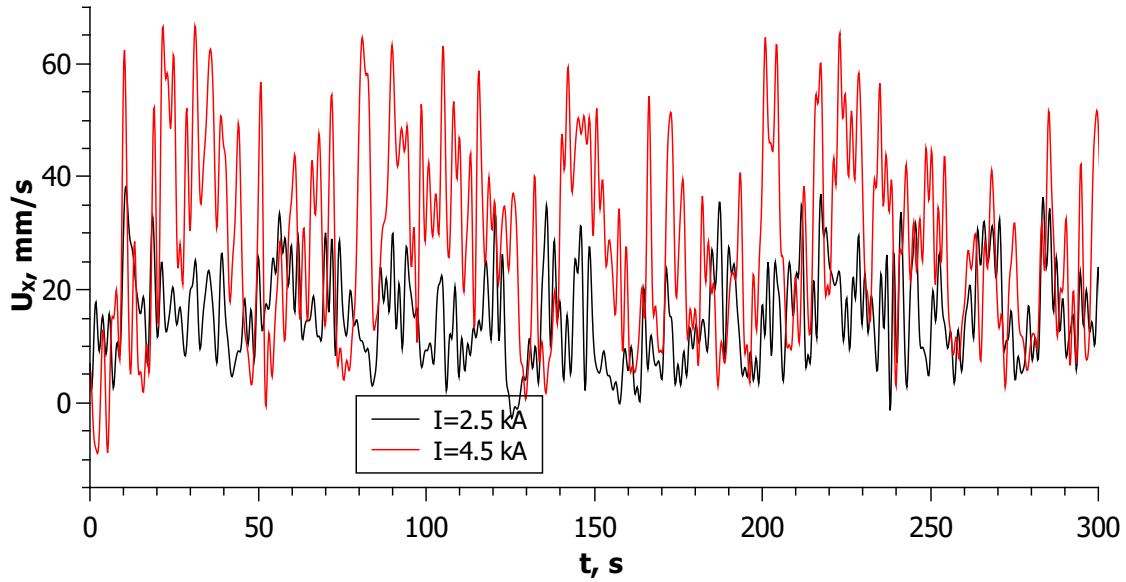

(a) Full time range

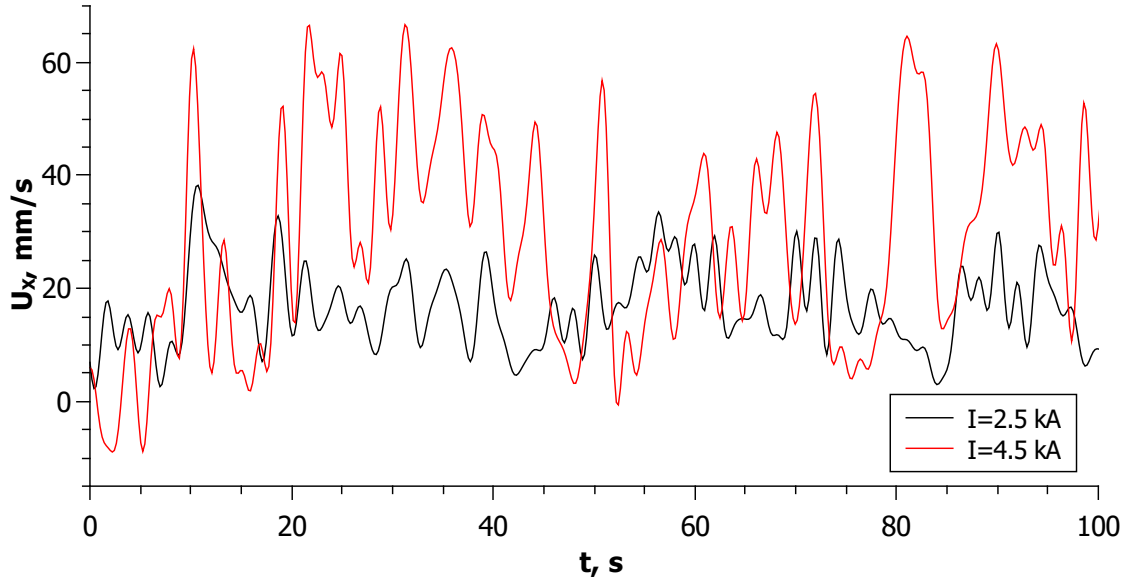

(b) Zoomed time range

Figure 6.12: U_X velocity pulsations at the point (X,Y,Z)=(-180, 0, 80). Low-pass filter is applied to measurement data with 1.0 Hz cutoff frequency. Measurement frequency was 5 Hz

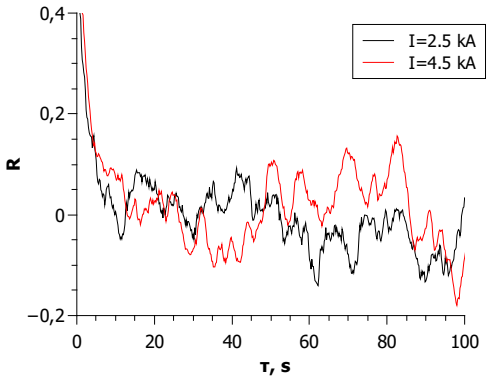

Figure 6.13: Autocorrelation of the measured velocity signals at the point (X,Y,Z)=(-180, 0, 80)

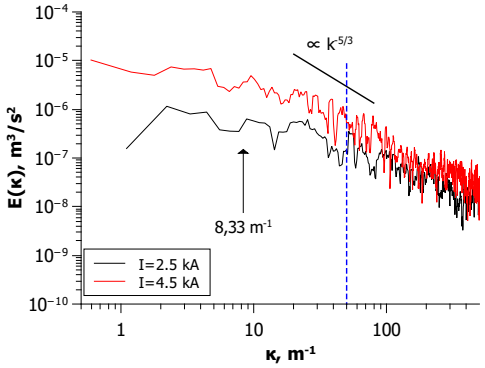

Figure 6.14: FFT of autocorrelation of velocity signals at the point (X,Y,Z)=(-180, 0, 80). Blue line shows cutoff wavelength corresponding to the UDV sampling volume dimensions – 10 mm

to detect an inertial range. Cutoff wavelength $k = 50$ m^{-1} corresponds to the doubled size of ultrasound beam volume in UDV technique (2×10 mm). Other commercial probes are available with sizes down to 5 mm. This would, however, only allow using smaller sampling volumes at small measuring depths because beam divergence angle at 2 MHz ultrasound frequency for 5 mm probe is almost twice larger than for 10 mm probe. The arrow in the figure points to the characteristic size of the crucible ($\kappa = 1/12$ cm$= 8.33$ m^{-1}).

6.2.3 Measurements in stratified flow

The U_X velocity component distribution measured in the Z=80 mm plane is shown in Figure 6.15. Velocity fields obtained for two different winding currents ($I = 2.1$ kA and $I = 2.5$ kA) have identical character. There are two large vortexes on the X range from -150 to 50 with velocity directed in $-X$ (minus X) direction in the middle and in the $+X$ direction near the walls. Two smaller vortices also exist on the X range 50 to 150. The flow seems to be symmetrical with respect to Y=0 line but unsymmetrical to X=0 line like in isothermal flow.

The flow structure in stratified flow differs from isothermal; however, it is not possible to make clear conclusion about the changes in flow field from horizontal cross section only. Additional measurements were performed in vertical Y=0 plane. The vertical cross section results reveal that there is a significant change in the velocity distribution in stratified flow in comparison to isothermal (compare Figures 6.11b

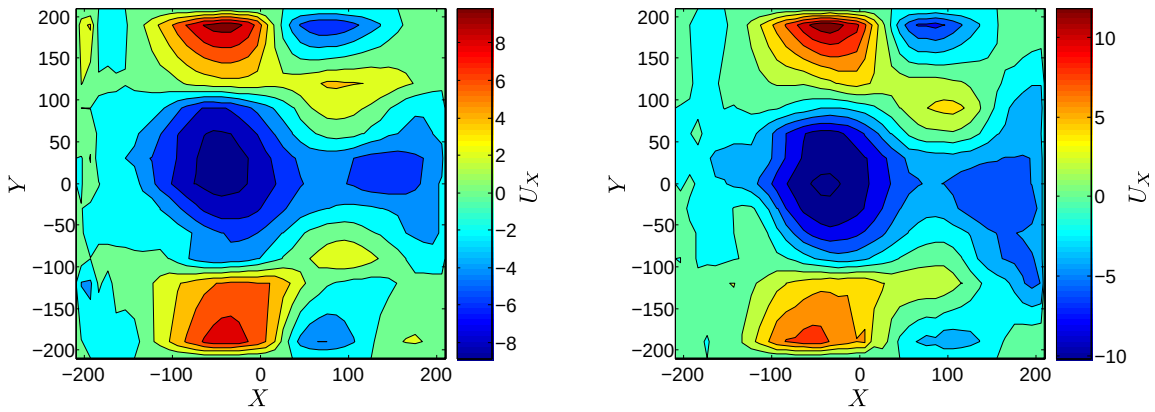

(a) $I = 2.1$ kA (b) $I = 2.5$ kA

Figure 6.15: U_X velocity distribution in Z=80 mm plane. Vertical temperature difference $\Delta T = 40$ K

and 6.16a). Temperature field prevents formation of the flow structures with vertical velocity component, and therefore, there are no evidence for vertical motion.

The existence of vertical motion is judged by the presence of $U_X = 0$ isolines, which are parallel to the X-axis. In other words, it means fluid moving in reversed directions on opposite sides of such isoline, and therefore, there might be vertical motion that encloses oppositely directed flows in vortex. Such judgment is, however, not strict, unless flow is two dimensional. It is impossible to get understanding about flow structure without knowing the whole flow in details, and therefore, either more measurement data are necessary in different cross sections, including other velocity components, or numerical simulation data. Numerical simulations will be discussed in the next chapter, and the author used his knowledge about numerical results to evaluate the measurement data. This remark is made with intention to explain how the existence of vortexes in certain planes is stated with having only one velocity component.

In the horizontal Z=30 mm plane measurements were carried out with longer averaging times for each profile (600 seconds, 3,000 profiles). This was done due to poor signal quality at the lower levels in stratified flow. The flow field obtained in these measurements is shown in Figure 6.16b. The velocity distribution does not have any symmetry with respect to X=0 mm and Y=0 mm lines. It consists of one large vortex filling whole domain and two smaller vortexes in the bottom left and right corners. Such flow structure looks inconsistent with force distribution in the crucible. Same flow structure is obtained also for $I = 2.5$ kA current. Measurements do not

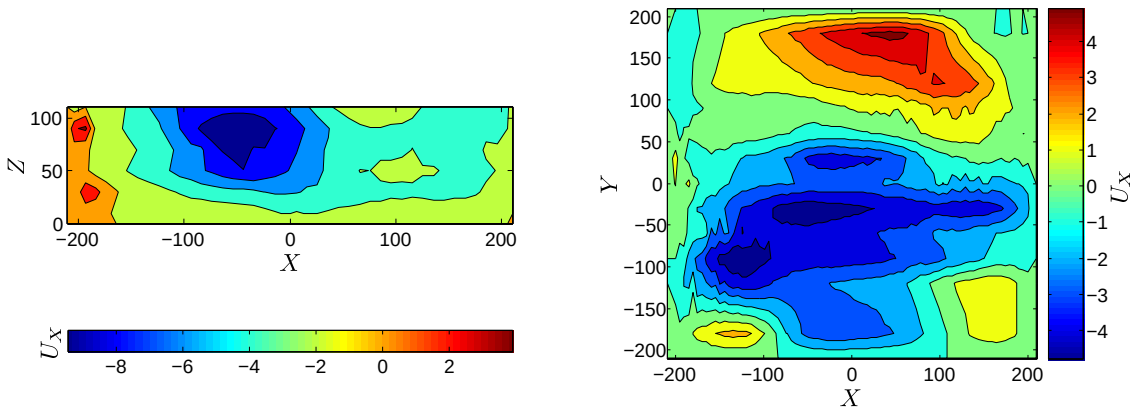

(a) Y=0 mm plane

(b) Z=30 mm plane

Figure 6.16: U_X velocity distribution in Z=30 mm and Y=0 mm planes for isothermal case. Vertical temperature difference $\Delta T = 40$ K, current in windings I=2.1 kA

explain the rise of such flow distribution, and it is not clear how does velocity change from the one in Z=80 mm plane (Figure 6.15a) to such distribution.

Measurements on higher lines (larger Z coordinate) for stratified cases were not always stable, mostly due to higher temperature of the wall at those spots. One reason for poor performance of measurements through the wall at higher temperatures is a working temperature limitation of the ultrasonic gel. When temperature of the wall exceeded 100 ℃, the gel started to convert into sticky glue-like mass, and the measured signal became weaker due to the worsening of ultrasonic coupling. This problem was partially resolved by using other coupling media, for example, vacuum grease. Another issue was poor signal at larger depths (large X coordinate), which occurred only in stratified cases for highest elevations (Z >90 mm). On the other hand, in stratified case, the reflected ultrasound signal close to the bottom of the crucible was weak along the whole profile. The possible explanation for such behavior is that natural impurities in the Wood's alloy have certain density, which in the stratified case allows them to concentrate in certain layer of the flow. This would explain why signal near bottom is weak – particle/impurity concentration is not sufficient there. Close to the top impurity concentration is larger, and this increases the attenuation of ultrasonic signal, and measurements can be made to some limited profile depth only.

The velocity profiles were also recorded for different current values for stratified case, with heater power $P = 3.5$ kW. Measurements were performed on horizontal line (Y, Z)=(0 mm, 80 mm). Measured profiles at different winding current values are shown in Figure 6.17. At low currents, the flow velocity in the middle region

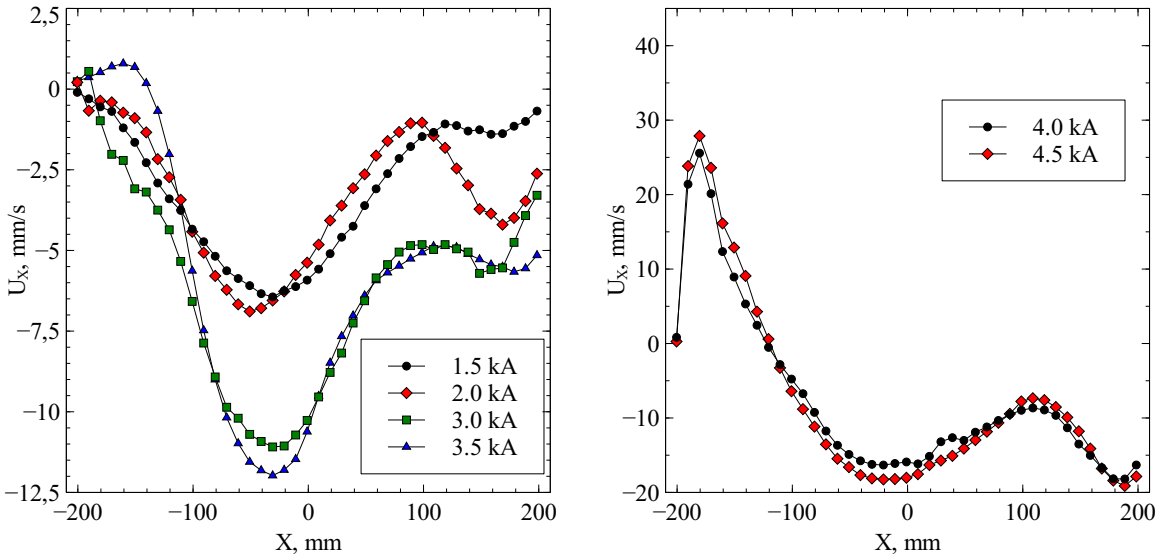

(a) I=1.5...3.5 kA (b) I=4.0...4.5 kA

Figure 6.17: U_X velocity distribution on the line (Y, Z)=(0 mm, 80 mm), heater power $P = 3.5$ kW

increases without change of the distribution form. Flow moving away from the left wall first appears at the $I = 3.5$ kA current. This current value corresponds to the critical current for $P = 3.5$ kW heater power. Sudden increase of flow velocity near wall is seen at $I = 4.0$ kA. The obtained velocity profiles for currents above $I = 3.5$ kA are very similar to those obtained in isothermal measurements. Near-wall peak values match for both cases within 10% (for currents $I = 4.0$ kA and $I = 4.5$ kA, the peak values for isothermal case are 23.4 mm/s and 27.7 mm/s, for stratified case, 25.6 mm/s and 27.9 mm/s), while peak location is slightly shifted – X=-170 mm for isothermal and X=-180 mm for stratified case. The peaks on the opposite side (X=+180 mm) have about 35% smaller values than in isothermal case (for currents $I = 4.0$ kA and $I = 4.5$ kA, the peak values for isothermal case are -27.0 mm/s and -29.0 mm/s, for stratified case, 18.2 mm/s and -19.2 mm/s). Velocity values in the the middle part of the profile are slightly smaller in the stratified case than in isothermal flow for same current value.

Although the velocity profiles obtained with heaters above the critical current have slight differences from isothermal flow, possibly caused by nonuniform temperature distribution in the melt, a conclusion can be made that also in velocity measurements, the transition between stratified and fully three-dimensional flow is found.

Chapter 7

Numerical Study of Thermally Stratified Flows

This chapter is devoted to analysis of results obtained in numerical simulations of the setup described in Section 3.4, and whose experimental results were presented in Chapter 6. The validation of results, flow regime change, and anisotropy aspects will be discussed here.

7.1 Large eddy simulation results

The Large eddy simulations (LES) were performed using OpenFOAM toolbox. The fluid flow simulation domain consisted of the melt domain only with sizes same as in experimental setup (see Chapter 3). Two different mapped meshes were used in LES calculations – coarser mesh with 800 k finite volume cells and finer mesh with 3 M cells (mesh example shown in Figure 7.1). Refinement near walls was used in both meshes. The mesh parameters are summarized in Table 7.1

Euler scheme was used for discretization of time derivative, and Gauss linear method was used for discretization of gradient, divergence and laplacian terms.

Electromagnetic calculations were performed using GetDP open source software with $T - \Omega$ formulation. EM simulation was performed once and then used Lorentz force and Joule heat were used as sources in fluid dynamics simulations. The force density distribution in vertical and horizontal cross sections is shown in Figure 7.2. In

Mesh	Max. cell size, mm	Near wall, mm	Nr. cells
M1	4.0	0.33	800 k
M2	2.0	0.068	3.5 M

Table 7.1: Parameters of the meshes used in the simulations

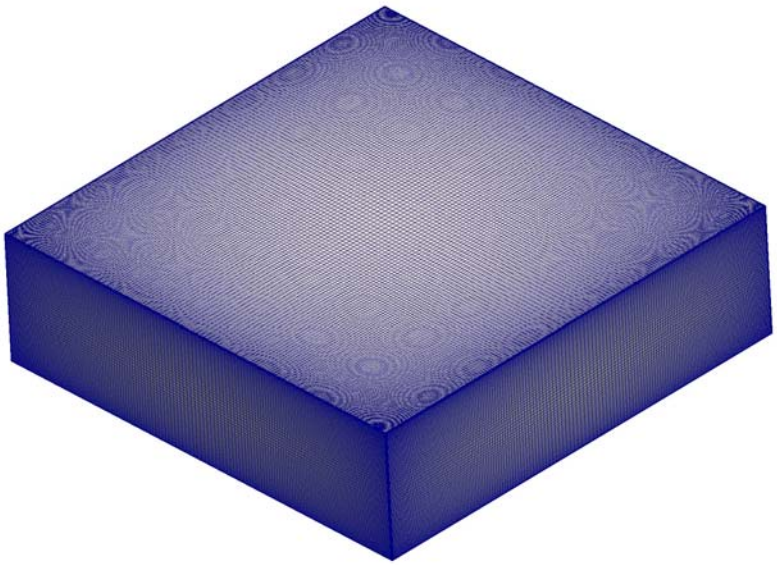

Figure 7.1: Finite volume mesh for fluid dynamics simulations.

the vertical cross section, force density has largest component in horizontal direction, with slight vertical force density component directed downward in the upper edges. In the horizontal plane, force density has similar distribution shape near all sides of the crucible, except the left one, where force is weaker due to inductor connectors.

Large eddy simulations were performed for different heating and EM forcing parameters. The simulation parameters are summarized in Table 7.2. For all cases, time step 500 µs was used, with total simulation time 1,200 s. Averaging was done over last 600 s. The simulations for mesh M2 were performed on 24 cores, and one run took in average 30 days. For M1 mesh, usually 8 cores were used, and one run took approximately 15 days.

7.2 Validation of simulation results

The velocity data from simulations were compared with experimental results on several lines. Lines are defined as follows: L1 - (Y,Z)=(0 mm,110 mm), L2 - (Y,Z)=(0 mm, 80 mm), L3 - (Y,Z)=(180 mm, 80 mm). Figures 7.3, 7.4, and 7.5 show such comparison for cases A1, A6, and A7 over different lines.

The results for isothermal flow are compared only in range X=-210...50 mm. The rest is not used in comparison because of significant velocity gradients in directions perpendicular to the X-axis (ultrasonic beam) in the flow. Since ultrasonic beam has increasing diameter along measuring depth, the sampling volume is increasing, and

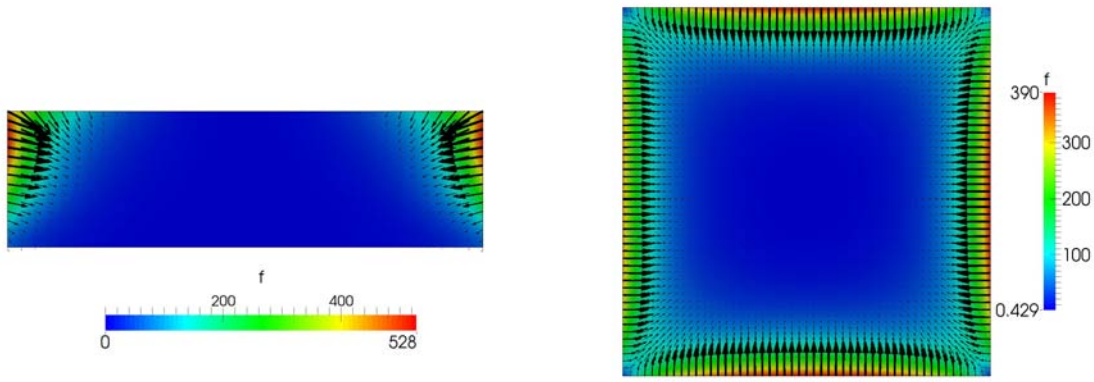

(a) vertical plane Y=0 mm (b) horizontal plane Z=60 mm

Figure 7.2: Force density distribution in the melt for $I = 3.0$ kA current

Case	Current I, kA	T_{TOP}, $°C$	h, W/m^2K	Re	Ri
A1*	2.5	150	1,400	10,400	0.08
A2*	3.0	150	1,400	6,133	17.1
A3*	3.0	230	1,000	5,813	40.1
A4*	4.2	150	1,400	12,373	3.0
A5	6.0	150	1,400	24,347	0.6
A6*	2.1	150	1,400	4,027	40.9
A7	2.5	130	1,400	5,200	17.1
A8	2.5	150	1,400	4,827	28.0
A9	3.0	130	1,400	6,347	11.1

Table 7.2: Parameters of LES simulations. I - total current in both windings, T_{BOT} - bottom wall temperature was always 80 ℃, T_{TOP}, h - reference temperature, and heat transfer coefficient at top surface. Simulations in A1 are performed with reduced buoyancy effect – g was set to 10^{-3}. Cases marked with star in superscript are simulated for both M1 and M2 meshes; others are only for M1.

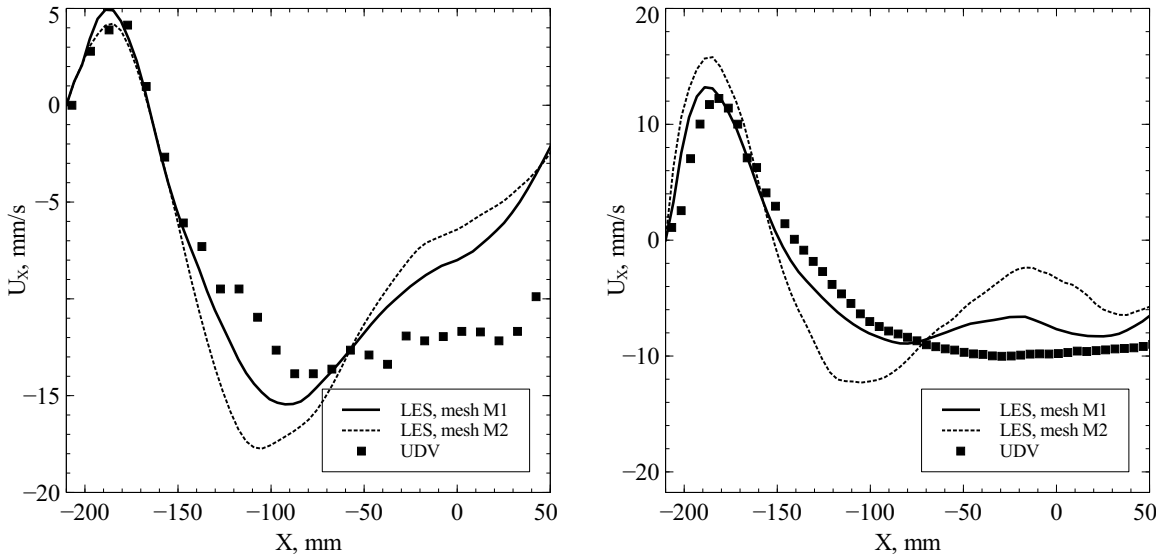

(a) Line L1 (b) Line L2

Figure 7.3: U_X velocity component comparison for A1 case. Lines show LES results, dots – UDV

therefore, comparison of UDV data with single line from simulation is not a correct approach. In isothermal flow (Figures 7.3a and 7.3b), UDV and LES results have best agreement at small measurement depths (X=-210...100 mm). Both LES curves have the same character, their peak values differ about 15%, while there is significant difference between LES and UDV results in region further away from US transducer - X=-50...50 mm. Furthermore, it seems that coarser mesh results have better match with experimental data. There might be an explanation for this fact, based on the analogy between sampling volume in UDV and finite volume filter in LES.

Another reason for deviations between LES and UDV results is the presence of high gradients in the flow. On all lines where LES results are compared, even 5 mm shifting of line in any direction changes velocity profile significantly.

For stratified flow in cases A6 and A7, similar order of agreement is achieved (see Figures 7.4 and 7.5). Experimental results in both cases have very similar character, just the magnitude changes. On the other hand, in LES simulations, there is a slight change at the right wall near coordinates X=190 mm, where additional velocity peak appears in A7 case.

The possible cause of discrepancies between experimental and simulation results can also be the physical assumptions in numerical computations. Here is a list of assumptions that might introduce certain error:

- Temperature dependence of material properties were neglected. This might be

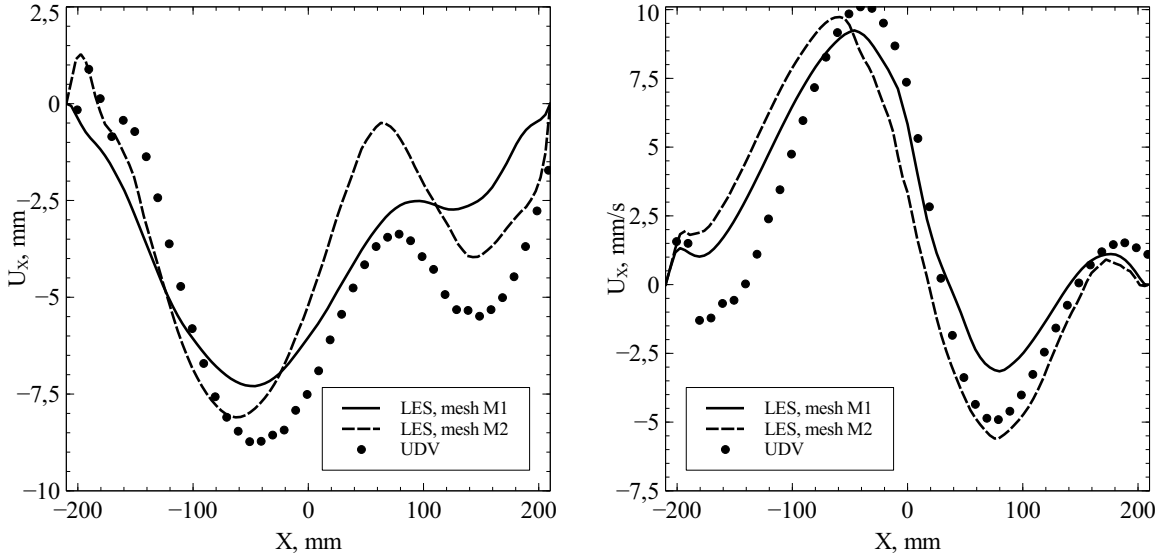

(a) Line L2 (b) Line L3

Figure 7.4: U_X velocity component comparison for A6 case. Lines show LES results, dots – UDV

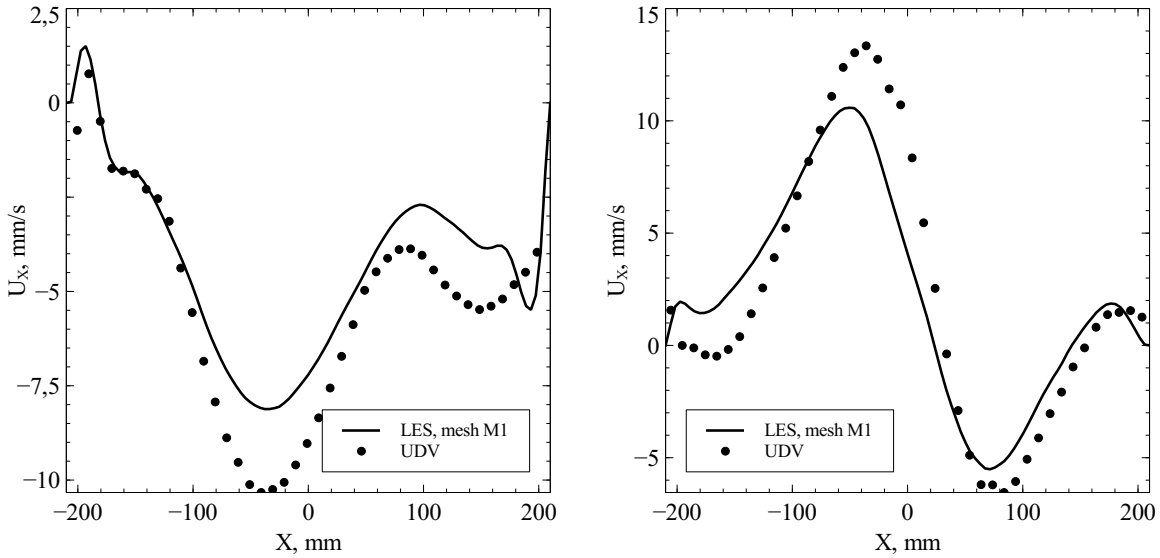

(a) Line L2 (b) Line L3

Figure 7.5: U_X velocity component comparison for A7 case. Lines show LES results, dots – UDV

especially important in stratified flow, where up to 80 K temperature variations occur. Measurements of viscosity in Wood's alloy [107] showed that viscosity at 150℃ is 30% lower than at 80℃.

- Change of alloy's composition in stratified case was neglected. In experiments, it was observed that if after stratified flow measurements the melt was let to cool down without stirring (not below 80℃, bottom plate heating was still on), a solidified material occured on the surface. This material had reasonably higher melting point, approximately 110℃, which leads to conclusion that alloys decomposition during stratified runs takes place.

- Thermal condition on walls is idealized. Assuming inner temperature of the wall 150℃ (this will be overvaluation, because temperature is linearly decreasing in $-Z$ direction), outer temperature 30℃, thickness of isolation 20 mm, and Armaflex thermal conductivity ($\lambda = 0.042$ W m^{-2}K^{-1}), one can obtain estimation for wall heat flux – $q_w = 252$ W m^{-2}. Assuming vertical temperature difference in melt 70℃, vertical heat flux is estimated as $q_v = 8200$ W m^{-2}. This shows that vertical heat flux is 30 times higher than maximal wall heat flux.

- Thermal condition on free surface is idealized. In simulations, the boundary condition $q = h(T - T_0)$ is assumed on the free surface. The coefficient h is estimated from experimental observations by measuring temperature in the air 5 mm above the free surface. At 2.0 kW heater power, the temperatures measured 5 mm above and below the free surface were 204℃ and 152℃, respectively. Taking into account the 0.5 factor for the heat flux (shown in previous chapter), the heat transfer coefficient can be estimated as $h_{EXP} = 109$ W m^{-2}K^{-1}. For the 3.5 kW power - $h_{EXP} = 97$ W m^{-2}K^{-1}. However, such boundary condition in simulation does not allow to estimate a vertical temperature gradient in melt a priori; therefore, it was decided to increase heat transfer coefficient and decrease ambient temperature. In simulations, typical value $h = 1400$ W m^{-2}K^{-1} was used with ambient temperature $T_0 = 150$℃.

- Uniform temperature is assumed on the bottom. This assumption was checked by measuring the bottom temperature in an empty crucible by using infrared camera. Maximal difference of 4 K was obtained.

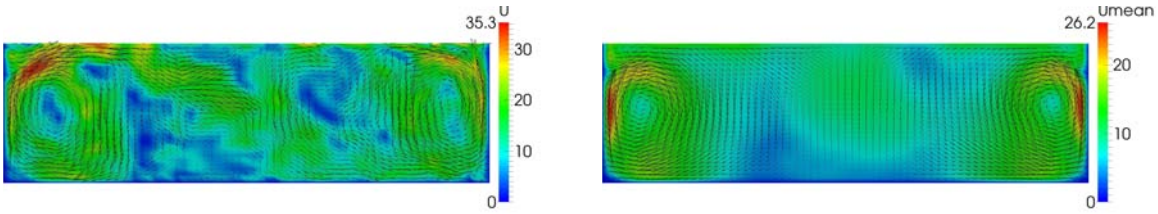

(a) Instantaneous (b) Mean

Figure 7.6: Velocity field in the vertical cross section X=0 for the case A1

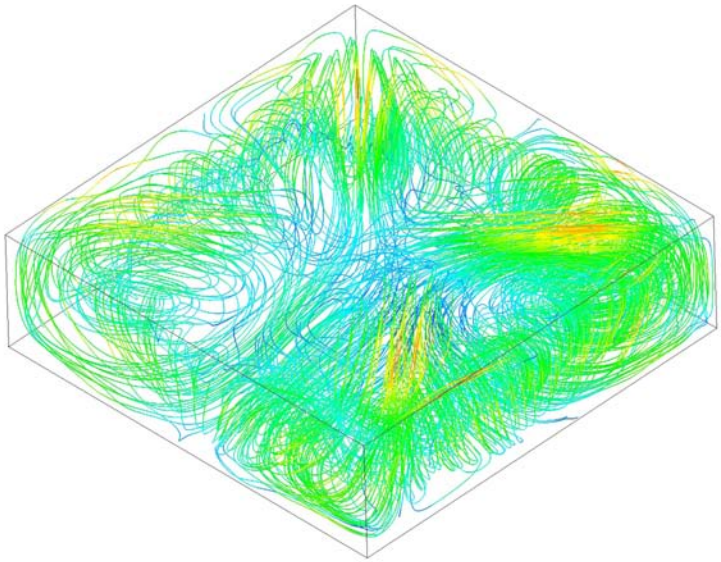

Figure 7.7: Streamlines in the LES simulation in the case A1

7.3 Velocity field for isothermal and stratified cases

The isothermal case (Table 7.2) was calculated with reduced free-fall acceleration $g = 10^{-3}\mathrm{m/s}^2$, and therefore, temperature field has negligible effect on the velocity field. In this case, flow has significant z velocity component. In Figure 7.6, velocity field in the vertical cross section is shown, where vortexes are visible with their vorticity vector parallel to the sidewalls of the crucible (see streamlines in Figure 7.7). The rotation of the vortexes is such, that velocity is directed upward near the wall and downward in the center of the crucible.

The distribution of the mean velocity in the horizontal plane (Figure 7.8b) is symmetric with respect to Y=0 plane. The instantaneous distribution (Figure 7.8a) shows the presence of small-scale eddies down to the size of 15 mm. The maximal mean velocity magnitude in the volume is 39 mm/s, while instantaneous velocity reaches 55 mm/s in peaks.

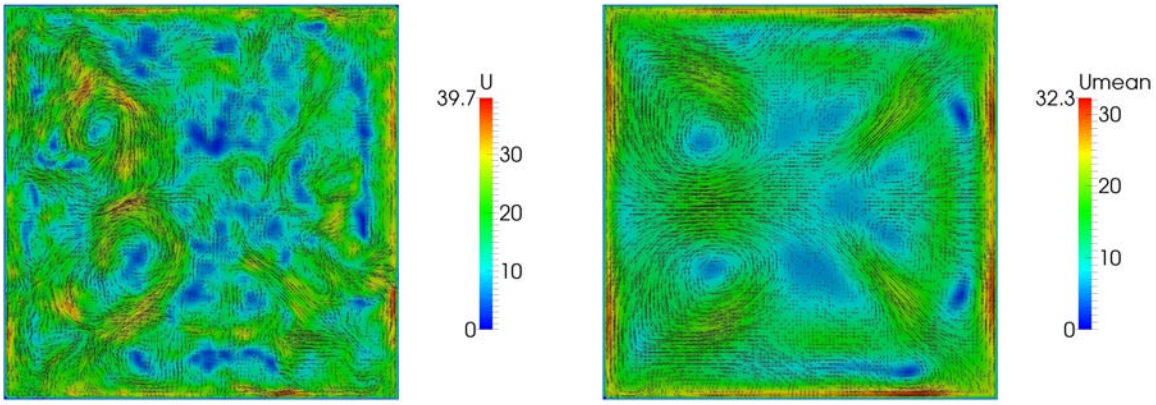

(a) Instantaneous (b) Mean

Figure 7.8: Velocity field in the horizontal cross sections Z=6 cm for the case A1

In the stratified flow, fully two-dimensional flow is expected. However, LES results show that even at Richardson number $Ri = 11.1$ (case A9), there exists vertical motion. In Y=0 mm plane (Figure 7.9), two small vortexes near each wall are detected. Stronger vortex with characteristic velocities up to 16 mm/s in the upper part is caused by the vertical force component near the crucible edge. The lower vortex is generated by shear stress in the zones between eddies, because force densities in this region are insufficient to produce eddies with typical velocities up to 5 mm/s (only in-plane components are considered for this value).

In the horizontal plane (Figure 7.10), symmetric structures (with respect to Y=0 plane) are observed in the Z=90 mm plane, less symmetry is present in Z=60 mm plane, and fully unsymmetrical flow field in near bottom of the crucible in Z=30 mm plane. This finding is consistent with measured unsymmetrical flow structure in the same plane (Figure 6.16b). Furthermore, the structure of both flows is similar – one large vortex filling almost whole domain and two smaller vortexes in edges. Same effect in similar system (square crucible with electromagnetic forcing) is observed also in [29]. Creation of such rotation most likely has same nature as vortex merging, described in Chapter 5. However, such effect can take place only in case of conditions close to two-dimensional. It can be achieved either by strong stratification, like in Figure 7.10, or by shallow fluid layer (Chapter 5 and [29]).

The creation of rotating flow by means of multiphase magnetic field in directional solidification furnace is shown in [22]. In such system, flow rotation is possible to control by frequency, phase shift, and magnetic field intensity.

Large vortex at the bottom of crucible was found both in numerical simulations and experiments, and it raises a question – is it possible to create controllable rotation

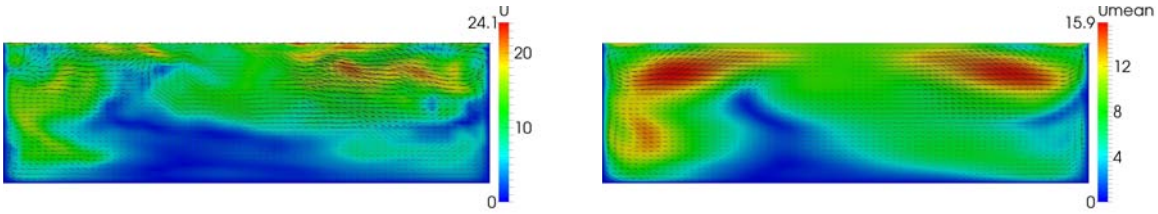

(a) Instantaneous (b) Mean

Figure 7.9: Velocity field in the vertical cross section X=0 for the case A9

of flow in square crucibles by using single-phase magnetic field? One is clear – there will always be additional smaller vortexes to keep the angular momentum of the system zero. Furthermore, it is not clear how such flow can influence crystal growth. This topic needs further investigation.

7.4 Spectral analysis of calculation results

In all simulations velocity, temperature and pressure in certain points of interest were recorded on each time step to obtain time dependence (full set of variables in all finite volume cells were saved only each 1,000 time steps). Three points are analyzed here; all are located in Y=0 mm plane. P1 is located in the mass center of the crucible (X,Y,Z)= (0 mm, 0 mm, 60 mm). This point is interesting because it is far away from walls, and the flow here is with smallest vertical component in the stratified cases. Two points are also chosen in the zone of active forcing, P2 – (X,Y,Z)= (200 mm, 0 mm, 60 mm), and P3 – (X,Y,Z)= (200 mm, 0 mm, 90 mm). Points P2 and P3 are of great interest because in the isothermal case, they are in the region of most intensive vortexes, while in the stratified cases, they lay in different zones – P3 in the region where Z component is present, and P2 in the stratified layers.

Autocorrelation of velocity signal can show how significantly vertical temperature influences turbulence. Figures 7.11a and 7.11b show the autocorrelation coefficient R for cases A1 and A7 in point P2. Slower variation of R in stratified case is direct evidence to elimination of high-frequency oscillations. To quantify this change in flow, Eulerian timescale is calculated (equation 2.33), which is seen in figures 7.11c and 7.11d. Timescale in stratified case is significantly larger. Taylor microscale is also calculated for each point. Data are summarized in Table 7.3. For isothermal flow, Reynolds number based on Taylor microscale is $Re_\lambda \approx 250$ in point P3, while for stratified case, it is $Re_\lambda \approx 120$. Flows below $Re_\lambda = 100$ are considered as weakly turbulent, and therefore, one can say that both isothermal and stratified cases are

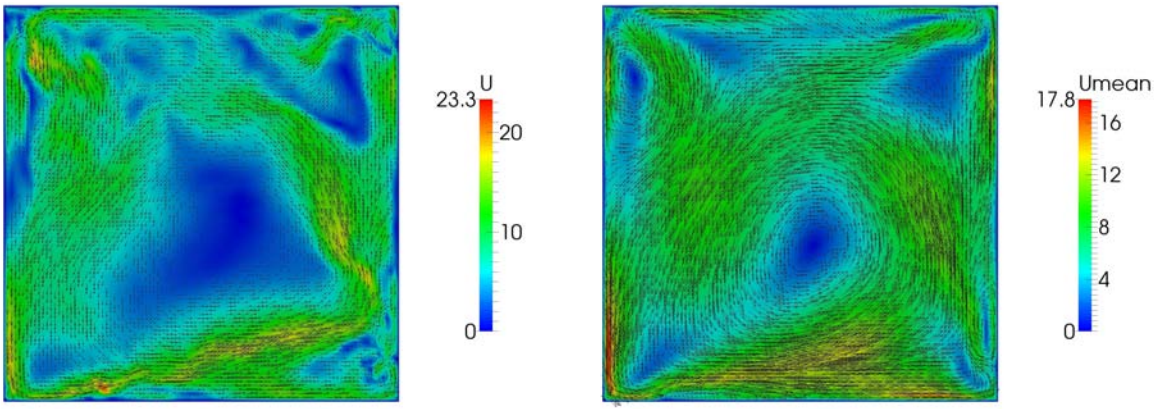

(a) Instantaneous, Z=3cm (b) Mean, Z=3cm

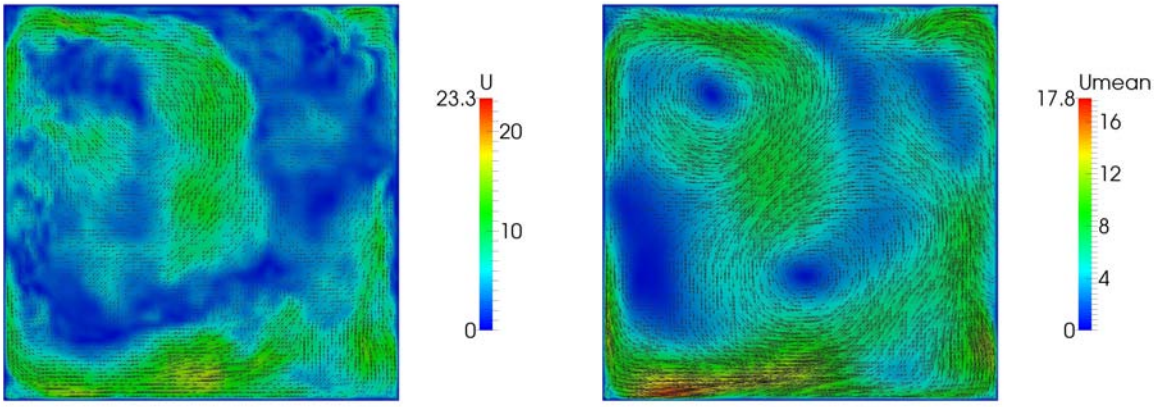

(c) Instantaneous, Z=6cm (d) Mean, Z=6cm

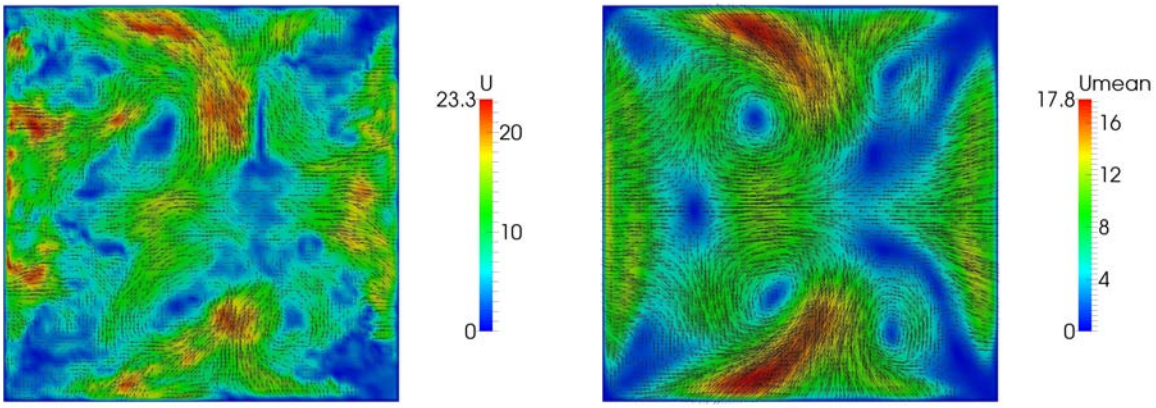

(e) Instantaneous, Z=9cm (f) Mean, Z=9cm

Figure 7.10: Velocity field in the horizontal cross sections Z=const for the case A9

Variable		P1			P2			P3		
s	s	x	y	z	x	y	z	x	y	z
A1	$\bar{u}$	-8,18	1,92	-6,13	1,80	-0,34	23,22	-11,63	1,42	11,78
	$\overline{u'u'}$	39,59	77,08	39,89	39,33	39,41	43,04	23,91	35,66	137,89
	τ_E	1,31	1,42	1,37	0,52	0,49	0,44	0,67	0,57	0,84
	λ_T	8,24	12,42	8,62	3,28	3,08	2,86	3,28	3,40	9,90
	ϵ	3,24	4,19	3,12	8,09	8,63	10,17	4,92	7,08	9,40
A7	$\bar{u}$	-4,73	-5,20	0,10	-0,43	6,04	-0,54	-4,84	-0,94	-0,35
	$\overline{u'u'}$	2,62	8,18	0,62	0,86	10,25	0,77	3,15	11,94	1,96
	τ_E	4,38	6,07	3,54	3,18	4,69	2,72	3,42	4,55	2,46
	λ_T	7,10	17,37	2,78	2,94	15,01	2,39	6,07	15,74	3,44
	ϵ	0,25	0,32	0,15	0,20	0,46	0,22	0,35	0,51	0,39

Table 7.3: Microscale parameters calculated for cases A1 and A7. List of units for variables: $[\bar{u}] = mm/s$, $[\overline{u'u'}] = mm^2/s^2$, $[\tau_E] = s$, $[\lambda_T] = mm$, $[\epsilon] = m^2/s^3 \cdot 10^{-8}$.

within turbulent regime, at least in certain regions of the flow, where highest velocities appear.

Figure 7.12 shows energy spectra in points P1, P2, and P3 for cases A1 and A7. Some important tendencies are visible in the comparison of the isothermal and stratified cases. First of all, the spectral energy is always higher in the A1 case, although both cases have the same current in windings. Stratified flow has lower velocity values, and therefore, the turbulence intensity is lower.

Another important aspect is the difference between energy spectra intensity of different velocity components. In A1 case, the isotropic turbulence assumption might be valid, especially in the middle zone, far away from the walls (Figure 7.12a). In all spectra of the A7 case, the Z energy spectrum has lower intensity than other components. The largest difference is in the point P1 (Figure 7.12b), where pulsations in Y and X directions have energy about one magnitude higher than pulsations in Z direction.

The spectra in the point P2 (Figure 7.12c) has untypical character, where region parallel to the $k^{-5/3}$ curve is very short. Probably such character is dictated by the fact, that this point is exactly in the vortex edge with velocity maximum.

7.5 Analysis of the anisotropy of flow

Anisotropy coefficients K (see Chapter 2) are used to quantify anisotropy of the stratified flow. Four coefficients are chosen for this purpose [108]:

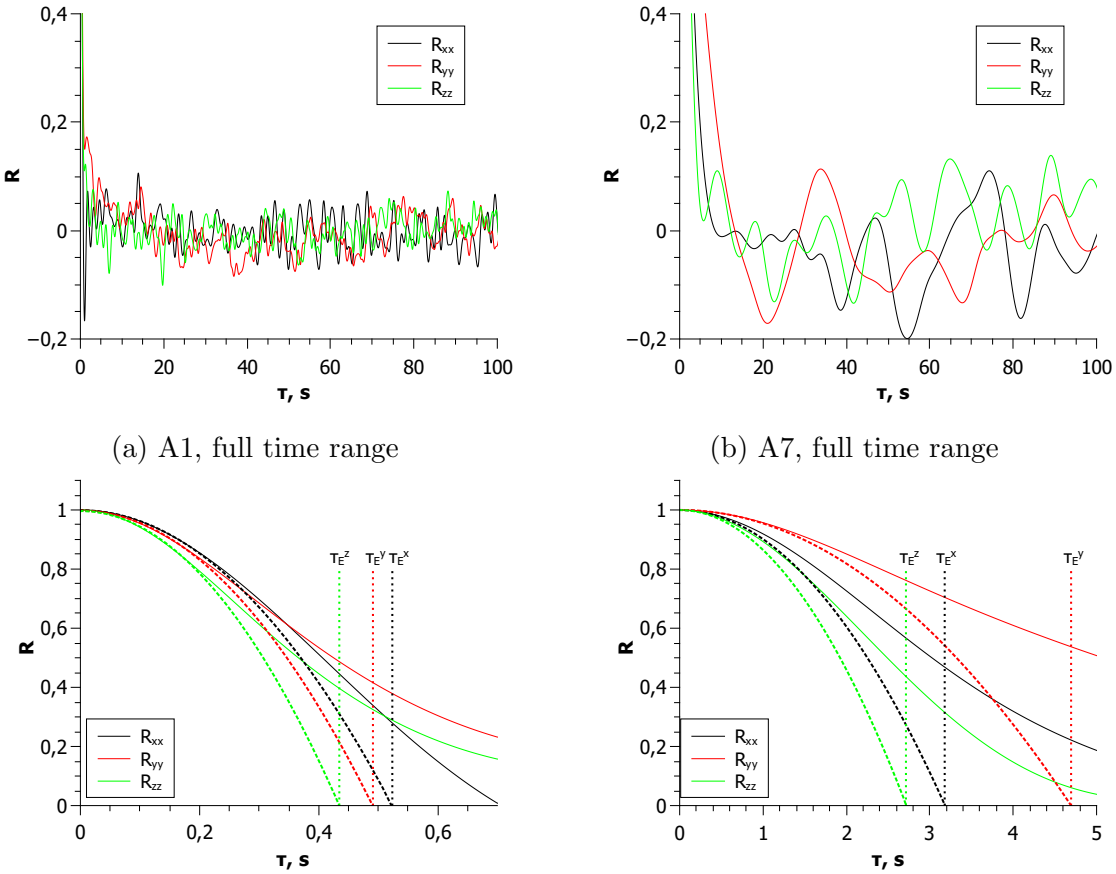

(a) A1, full time range

(b) A7, full time range

(c) A1, zoomed time range

(d) A7, zoomed time range

Figure 7.11: Autocorrelation function in point P2

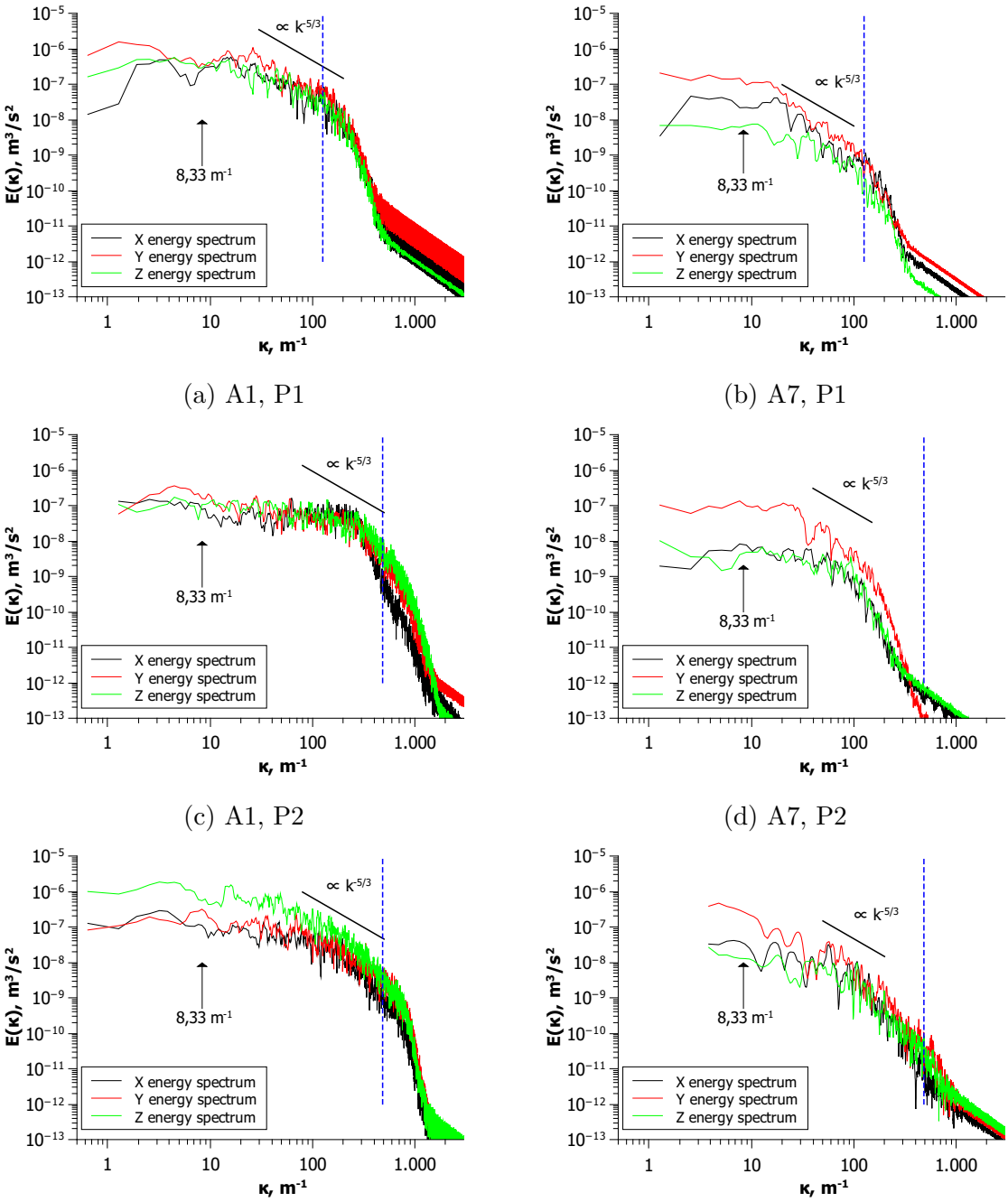

(a) A1, P1

(b) A7, P1

(c) A1, P2

(d) A7, P2

(e) A1, P3

(f) A7, P3

Figure 7.12: Energy spectra from LES data

$$K_1 = 2\frac{\left\langle \left(\frac{\partial u_x}{\partial x}\right)^2 \right\rangle}{\left\langle \left(\frac{\partial u_y}{\partial x}\right)^2 \right\rangle} \qquad K_2 = 2\frac{\left\langle \left(\frac{\partial u_x}{\partial x}\right)^2 \right\rangle}{\left\langle \left(\frac{\partial u_z}{\partial x}\right)^2 \right\rangle}$$

$$K_3 = 2\frac{\left\langle \left(\frac{\partial u_y}{\partial y}\right)^2 \right\rangle}{\left\langle \left(\frac{\partial u_x}{\partial y}\right)^2 \right\rangle} \qquad K_4 = 2\frac{\left\langle \left(\frac{\partial u_y}{\partial y}\right)^2 \right\rangle}{\left\langle \left(\frac{\partial u_z}{\partial y}\right)^2 \right\rangle}$$

Other coefficients, which will not be shown here, behave in similar manner. All cases are scaled with respect to coefficient ($\overline{K_1}$) in A1 case (see Table 1):

$$\overline{K_1} = \frac{1}{T}\int_0^T K_1(t)dt \tag{7.1}$$

Then corresponding normalized coefficients are

$$K_i^* = \frac{K_i}{\overline{K_1}} \tag{7.2}$$

The development of anisotropy is compared for four cases – small buoyancy effect (A1), intermediate Richardson number (A9 and A2), and stratified flow (A6). The results are presented in Figure 7.13. For all cases with $Ri >> 1$ (A2, A6, A9), stratification changes flow character, but anisotropy coefficients K never differ from unity by more than four times. Therefore, strain rate tensor components $S_{ij} = 1/2(\partial\overline{u_i}/\partial x_j + \partial\overline{u_j}/\partial x_i)$ are obviously within one order of magnitude. Notable difference exists in the time required for coefficients K to reach steady value in all cases. The A1 case results (Figure 7.13a) are almost constant in time, since coefficients K reach their mean value already after 20τ ($\tau = L/U$). Intermediate Ri cases (A2 and A9 – Figures 7.13c, 7.13b) require nearly 125τ to reach their end value, while high Ri case (A6, Figure 7.13d) – less than 25τ. This is most likely connected with initial condition for temperature ($T = const$). Vertical temperature gradient develops from zero to maximal value significantly slower than velocity field (Peclet number is large – $Pe = RePr$). Three-dimensional flow structure, which develops in all simulations at the initial time, is either slowly damped while temperature gradient is increasing, or changes rapidly if critical gradient value is reached when buoyancy forces are greater than inertial.

Coefficients K_2 and K_4, which both include derivative of u_z, are always lower than K_1 and K_3. Since this effect is present also in case that is weakly influenced by buoyancy (Figure 7.13a), possible cause could be the flattened geometry (height/width

ratio is $\approx$ 0.3) where flow is more damped by walls in vertical direction than in horizontal.

For more detailed analysis of the flow anisotropy invariants of $b_{i,j}$ tensor (Eq. 2.34) are used, results are plotted in Figure 7.14. Lumley [53] showed that invariants II and III are limited in their values, and the plane of these values forms turbulence triangle; the values outside of triangle are not allowed. The (0,0) point corresponds to three-dimensional turbulence, leftmost point – isotropic 2D turbulence, and rightmost point – 1D turbulence. The upper line of triangle represents 2D turbulence that by moving from left to right transforms from oblate to prolate.

The results obtained in LES simulations at different time steps are plotted on this triangle for cases A1–A6. Three cases with highest Richardson number have points in most upper left corner of turbulence triangle. A6 has the highest Ri and therefore, A6 data are placed in the most upper left position in the triangle. However, all these cases also have Reynolds numbers in the range 4,000–6,100, where developed turbulence assumption may not be valid. Other cases have points closer to 3D turbulence. As shown in the experiment, transition to strong mixing regime in this system appears at $Ri_{CR} \sim 5...10$, and A4 case is then also below this threshold. However, it is unclear why both cases within strong mixing regime (A1 and A5) are further away from 3D turbulence point than A4 case.

The results of $b_{i,j}$ invariants point to the anisotropy of Reynolds stress tensor $\tau_{ij} = -\rho\overline{u_i' u_j'}$ for strongly stratified flows. The widely used eddy viscosity assumption ($\tau_{ij} = 2\mu_t S_{ij}$) based models might therefore experience difficulties capturing these effects. A number of anisotropic eddy viscosity assumption based models are developed [109]; however, they still require calibration of constants. One of most important constants in turbulent heat transfer calculation is turbulent Prandtl number $Pr_T = \nu_t/\alpha_t$. The typical values used for turbulent flows vary between 0.7 and 1.0. However, it is shown that Prandtl number depends on local temperature gradient [110].

In LES simulations, volume averaged Pr_T and Ri is obtained for sub-volumes – calculation domain is divided in 10×10 blocks along X and Y directions respectively. To separate vertical mixing, the Prandtl number is calculated as

$$Pr_T = \frac{\overline{u_h' u_z'}}{2S_{hz}} \frac{\partial \overline{T}/\partial z}{\overline{u_z' T'}}$$

Here, index h corresponds to horizontal velocity $u_h = (u_x^2 + u_y^2)^{1/2}$. These data are plotted in Figure 7.15 as well as the fitting curve. From theoretical considerations in

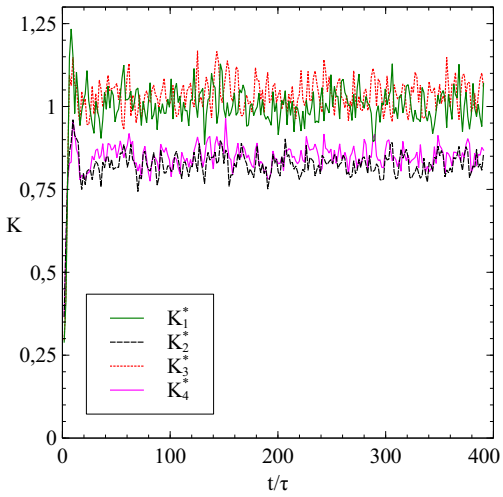

(a) Case A1. Re=10,400, Ri=0.08

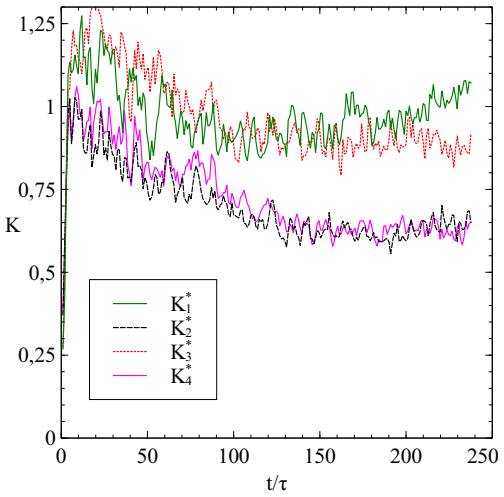

(b) Case A9. Re=6,347, Ri=11.1

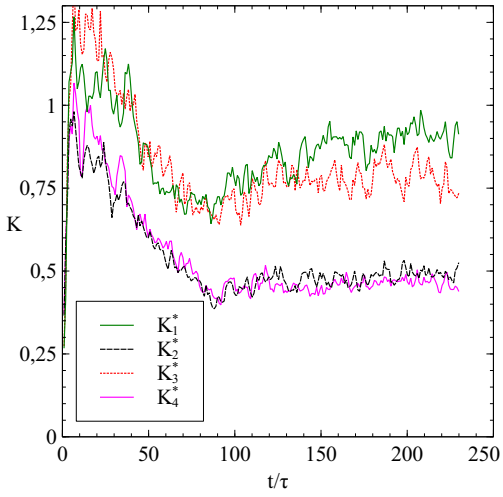

(c) Case A2. Re=6,133, Ri=17.1

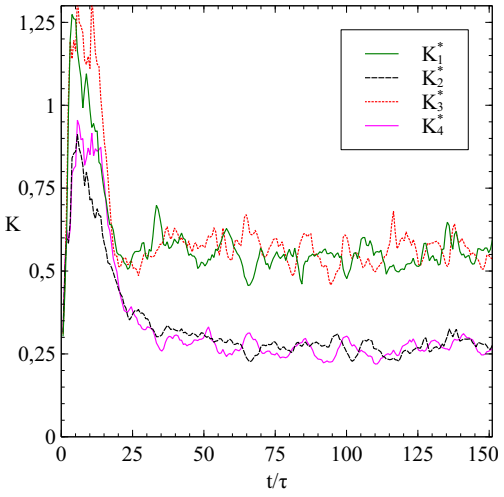

(d) Case A6. Re=4,027, Ri=40.9

Figure 7.13: Development of anisotropy coefficients K^*_{1-4} over time for simulations

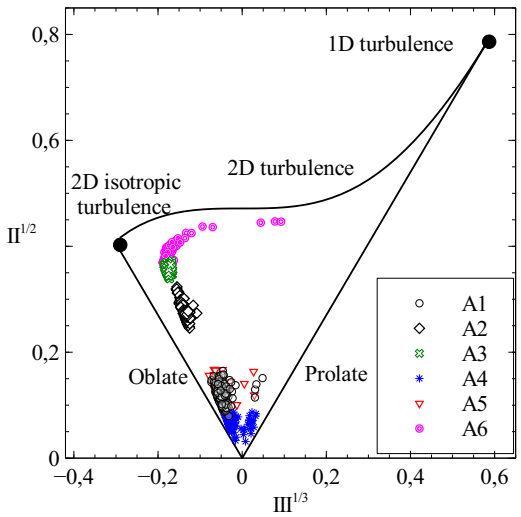

Figure 7.14: LES results plotted on turbulence triangle. (0,0) point corresponds to 3D turbulence. Form of the triangle defined in [53]

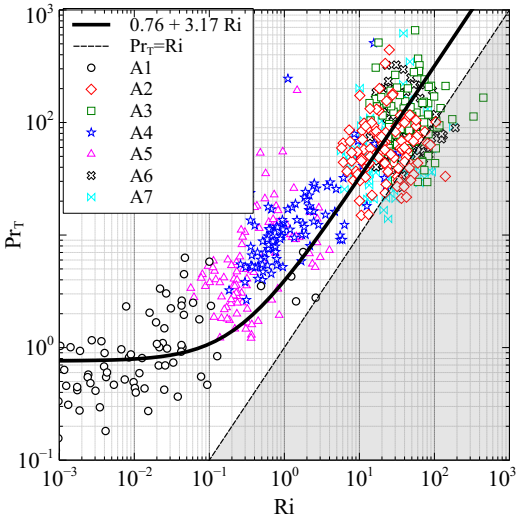

Figure 7.15: Pr_T as function of Ri in LES simulations for different cases

[110], it is known that Prandtl number is a linear function of Richardson number at high Ri.

The fitting is performed using logarithmic least squares method, and the obtained curve is $0.76 + 3.17Ri$. The $Pr_{T0} = 0.76$ is close to typical values for turbulent flows, as well as the slope of curve, 3.17, and the values found in literature are 4.0 in [110], 5.0 in [106], and 2.0 in [111]. Linear curve is used since it gives the best agreement for the whole Richardson number range – Prandtl number is equal to Pr_{T0} at very small Ri (neutral conditions) and theoretically proven constant slope as $Ri \to \infty$. However, linear function does not give good approximation of weakly stable stratification regime – $Ri = 0.1...1.0$, where different functions are used to fit the Prandtl number [112, 111].

The dashed line in Figure 7.15 represents the constant flux Richardson number Ri_f

$$Ri_f = \frac{Ri}{Pr_T} = \frac{g\beta\overline{u_z' T'}}{\tau S}$$

The numerator here represents the turbulence dissipation by buoyancy, and the denominator represents the turbulence generation by shear; therefore, Ri_f cannot exceed 1. In the present results (Figure 7.15), there are certain points in the high-Ri flow regimes, where Ri_f locally exceed unity. Local exceeding of this threshold can

be explained with nonuniform turbulence generation, which is then transported by convection to zones with high temperature gradient and buoyant dissipation.

Chapter 8

Simulations for industrial applications

In current chapter an example of numerical simulations for industrial directional solidification furnace will be shown. This research was initiated by ALD Vacuum Technologies GmbH, who is producer of described equipment. Confidentiality agreement allows to show only part of data specific to this equipment.

8.1 Investigated industrial furnace model

8.1.1 Thermal boundary conditions

The investigated system is shown in Figure 8.1. The 84 cm $\times$ 84 cm base area crucible is filled till the level of 24 cm with silicon melt (initially loaded as scrap or powder, and then molten by heaters – blue colored parts in the Figure 8.1). This system consists of three heater types - top, side and bottom heaters. All of them can be used as heaters and EM stirrers, because they are powered with 50 Hz AC current, thus creating alternating magnetic field. Design of the furnace also allowed to switch one of the heaters to DC power supply, thus retaining thermal heating, but losing EM stirring effect. Side heaters will not be used in this particular example, because they create flow field identical to examined previously in Chapters 7 and 6.

The solidification process is controlled by heater power and cooling plate visibility factor, which can be adjusted by means of special controllable heat gate in the bottom part of the furnace.

All the simulations in this chapter are performed with ANSYS software for global thermal and EM field calculations and ANSYS CFX for fluid flow results. First step in modeling of the melt flow was estimation of the thermal boundary conditions. Simplest approach would be applying fixed temperature conditions on the top and

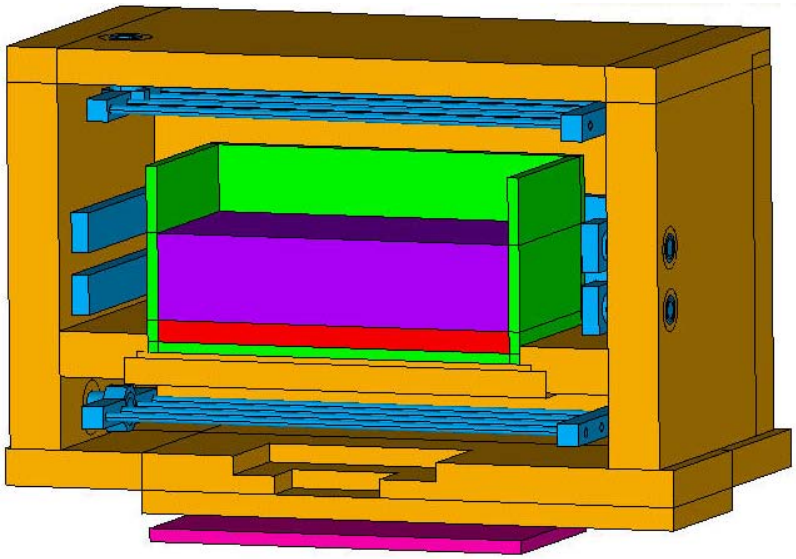

Figure 8.1: Industrial DS furnace, Model from ANSYS, cut in half. Colors show different materials. Purple - silicon melt, red - crystalline silicon, green - crucible, blue - heaters/inductors, orange - isolation, pink - cooling plate/heat sink.

bottom surfaces with adiabatic conditions on walls. However, such approach does not allow considering horizontal temperature gradients near the edged of the crucible. Global thermal simulations were performed for the whole furnace, including radiation heat flux by means of view factor method [113] (Global here means "for the whole furnace", to distinguish it from simulations in the melt only). Coupling of global thermal calculation and fluid flow in melt would lead to large computational costs, therefore global thermal calculation was performed only once and then heat fluxes were imported into the fluid simulation as boundary conditions.

For simulations, nominal current $I_N = 1700$ A was applied in the top heater, $I = 0.6I_N$ in the bottom heater and $I = 0.4I_N$ in each of both side heaters. First global simulations showed very high temperature differences in the melt, even in the horizontal direction, which was caused by non-uniform radiation heat flux at the free surface. Such temperature distribution is unrealistic, because motion of fluid was not considered in global simulations.

For more realistic distribution of the temperature in the melt, anisotropic thermal conductivity was set for melt material. Molecular vertical conductivity $\lambda_v = \lambda_m$ was used, while horizontal conductivity was 100 times increased, $\lambda_h = 100\lambda_m$. Necessity for such conductivity increase is dictated by the fluid motion, which enhances heat transfer in horizontal plane, while no additional heat transfer in vertical direction is expected (stratified flow). It is also known, that silicon in such furnace has nearly

horizontal solid-liquid interface, and therefore horizontal temperature gradients are small. Anisotropic heat transfer coefficients allowed to reduce horizontal temperature differences from 50 K down to $1 - 2$ K.

Figure 8.2 shows temperature distribution obtained in the global simulation of the furnace for the case when whole silicon volume is molten. Highest temperatures in the furnace are obtained on the top and bottom heaters, which are designed to have larger electrical resistance.

Use of fixed heat flux thermal boundary conditions in fluid flow simulations might lead to convergence difficulties in steady state simulations and to increase or decrease of the average temperature with time in transient calculations, because integral heat flux over all surfaces has to be zero; it can not be fulfilled due to numerical errors. Instead, more flexible boundary conditions were used. $T = T_{MELT}$ was set on the bottom of the melt. Heat flux boundary condition $q = q(\vec{r})$ was set on the top; $q(\vec{r})$ was obtained in global thermal simulation. On the sides convective heat flux boundary condition was set $q = h(T - T_o(\vec{r}))$, where $T_o(\vec{r})$ is the temperature distribution on the outer surface of the crucible obtained from the global thermal simulation.

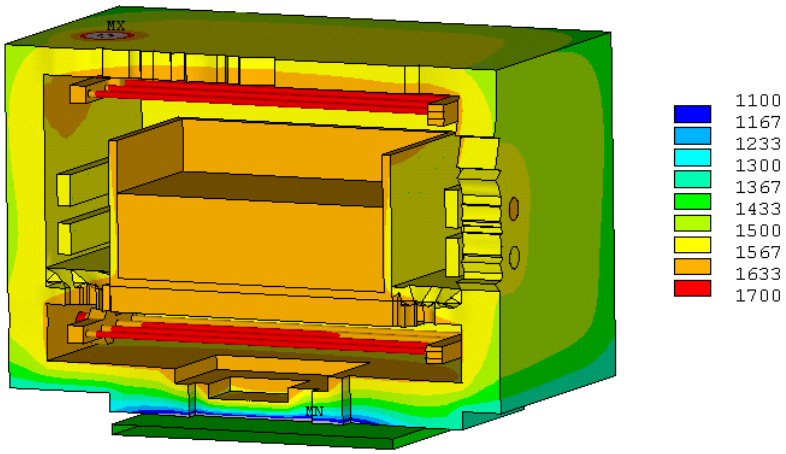

Figure 8.2: Temperature distribution obtained in global simulation.

8.1.2 EM force distribution

Lorentz force and buoyancy force are only driving mechanisms of fluid motion in the silicon melt. Lorentz force distribution in two cross sections is shown - in vertical, which represents symmetry plane, and horizontal at certain height from the crucible bottom.

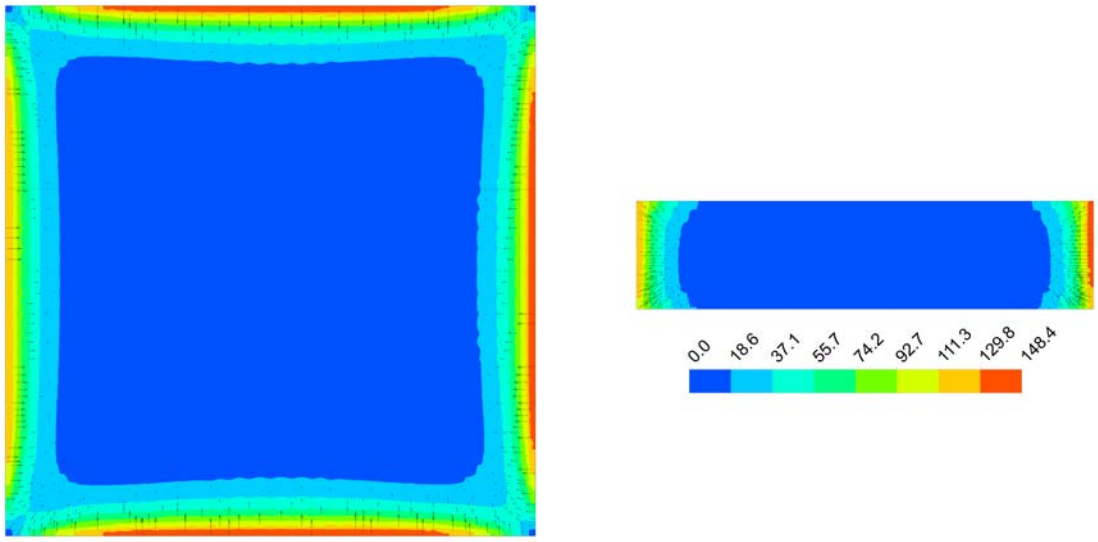

Figure 8.3: Lorentz force distribution in the melt created by side heaters. Left - horizontal cross section, right - vertical cross section.

The force field created by the side heaters is similar to the one in physical model, described previously in this work. Force field is nearly symmetrical, with 20% less force density on the electrical connector side (Figure 8.3). However, unlike the experimental model, there is no pronounced vertical force in the upper edge of the melt.

The melt flow can be controlled also by two other heaters, which create different force field than side heaters. The force field of the top heater is shown in Figure 8.4. The horizontal section is taken 15 mm below the melt free surface. There is pronounced downward directed force component in the upper edge of the crucible, which might be able to create vortex along the wall in the upper part of the crucible, similarly like in the model with Wood's alloy (Chapter 7). Furthermore, the force in the horizontal cross section is strong on two opposite sides, with smaller force density on the left (Figure 8.4), which is opposite to heater connector side. Side heaters and top heaters are connected on opposite sides (see Figure 8.1). Finally, the force created by the bottom heater is very similar to the one of top heater reflected with respect to the central horizontal plane of the crucible.

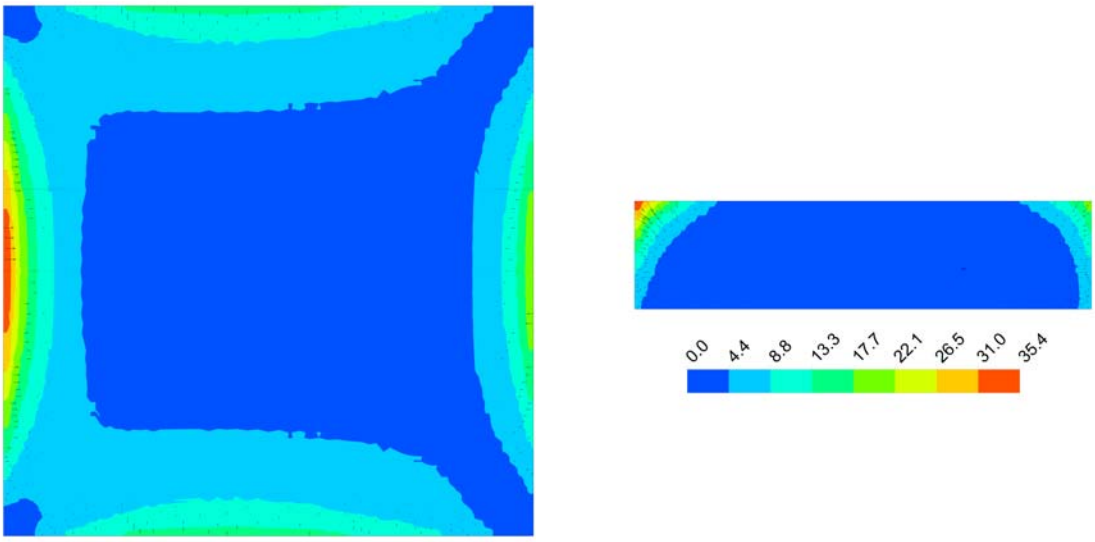

Figure 8.4: Lorentz force distribution in the melt created by the top heater. Left - horizontal cross section, right - vertical cross section.

8.2 Simulation of melt flow for quasi-mono silicon growth

Quasi-mono silicon growth [114] is relatively new topic which has gained popularity recently, because it offers great perspective of growing large size mono-crystalline silicon in DS crucibles. However, this method still experiences problems, mainly connected with interactions of growing crystals with crucible walls. Other issue is the required size of the seed crystal, which is larger than any common method can grow. Usually split seed is used - several seed crystals used instead of one. This however, leads to defects in the zones between growing crystals.

In the furnace described before (Section 8.1), split seed approach was used for growth of the quasi mono-crystalline silicon. The seed was placed at the bottom of crucible, covered with raw silicon; melting started from the top. When all silicon (except the seeds) was molten, growth process started.

In the final silicon block, wash-outs of the seed crystals were observed at the locations shown in Figure 8.5. It was assumed that they are generated by the flow motion in the early stages of the growth process. It is also known that side heater do not influence wash-outs, because they were not used in the initial stages of the growth process.

Three cases calculated by Large eddy simulation (see table 8.1) will be presented here. For each case, different stages of crystallization were simulated, each time with

Figure 8.5: Wash-outs in the final silicon block (red circle). Bottom of the block is shown. 6×6 seed crystals were used. Courtesy of ALD Vacuum Technologies GmbH

Case Name	Top current	Bottom current
TOP DC	I_N DC	$0.6I_N$ AC
BOT DC	I_N AC	$0.6I_N$ DC
AC-180	I_N AC	$0.6I_N$ AC 180° phase shift

Table 8.1: Cases of LES simulations for industrial furnace

steady geometry (neglecting front movement), for melt fractions in crucible 0.8, 0.65, and 0.5. Mesh for melt fraction 0.8 contained 1.3 millions of elements. Solidification front movement was neglected because its movement is slow ($\sim$ 1 cm/h) and time scale of fluid dynamic processes is much smaller.

For the case TOP DC smaller velocities are expected near the free surface of the melt. On the other hand, near the solid-liquid interface, motion is manly generated by the bottom heater. Figure 8.6 shows velocity distribution at $1/3H$ horizontal plane in the melt (H - melt height). Velocity distribution shows slightly asymmetrical pattern, which is similar to the one observed in Chapter 5 salt-water model measurements. It is also observed that velocity decreases with decrease of melt fraction. This can be explained with larger distance between melt bottom and bottom heater, which is the only active AC stirring heater in this case.

For the case BOT DC, where only top heater is actively acting on melt flow, higher flow velocities are observed due to higher current values used in top heater. Up to 2.2 cm/s velocities observed in BOT DC case, while only 1.2 cm/s velocity is reached in TOP DC case. Furthermore, in BOT DC results flow structure becomes more asymmetric and central vortex becomes more pronounced than in TOP DC case.

The stagnation zones between the vortexes near the crucible side walls approx-

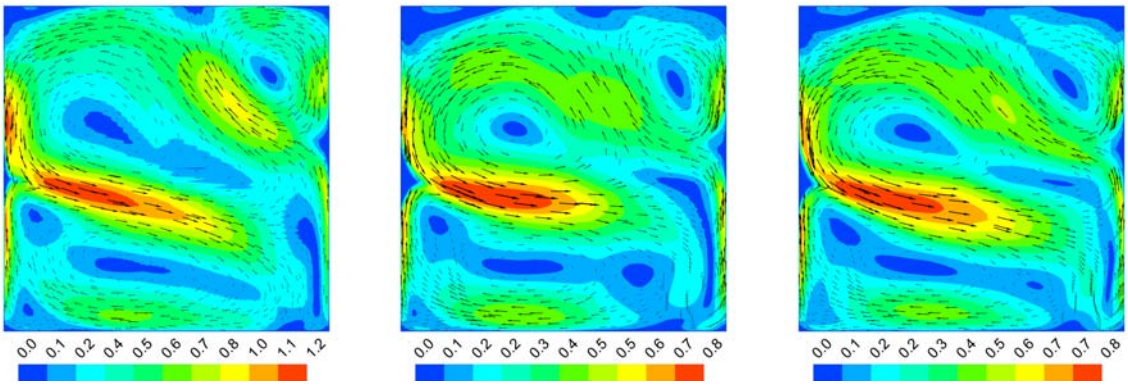

(a) Melt fraction 0.8 (b) Melt fraction 0.65 (c) Melt fraction 0.5

Figure 8.6: Velocity distribution at $1/3H$ horizontal plane for case TOP DC. Velocities showed in cm/s units

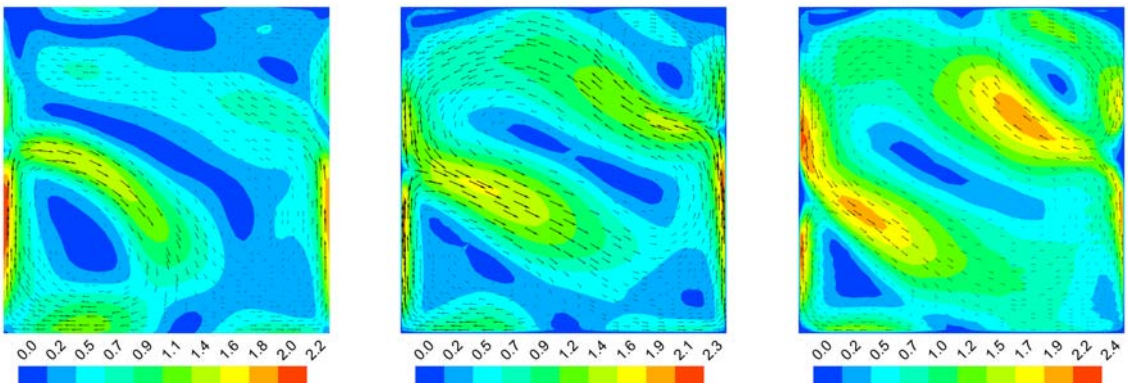

(a) Melt fraction 0.8 (b) Melt fraction 0.65 (c) Melt fraction 0.5

Figure 8.7: Velocity distribution at $1/3H$ horizontal plane for case BOT DC. Velocities showed in cm/s units

imately correspond with the wash-out zones in the seed crystals. From cylindrical induction crucibles it is known that intensive velocity pulsations are present between the vortexes. This phenomena can lead to intensified turbulence heat transfer near the melt-crystal interface and produce wash-outs. This hypothesis is partially proven in turbulence kinetic energy plots (Figure 8.8). TKE here is derived from resolved velocity in LES.

Turbulence kinetic energy distribution for BOT DC case (Figure 8.8b) is inconsistent with velocity distribution showed in figure 8.7. The reason for that is different plotting planes for both figures - TKE is plotted in plane 10 mm from the solid-liquid interface, but velocity plot is made on $1/3H \approx 70$ mm plane. Central vortex rotation direction change is observed at 50 mm from the bottom. This is result of fluid layer

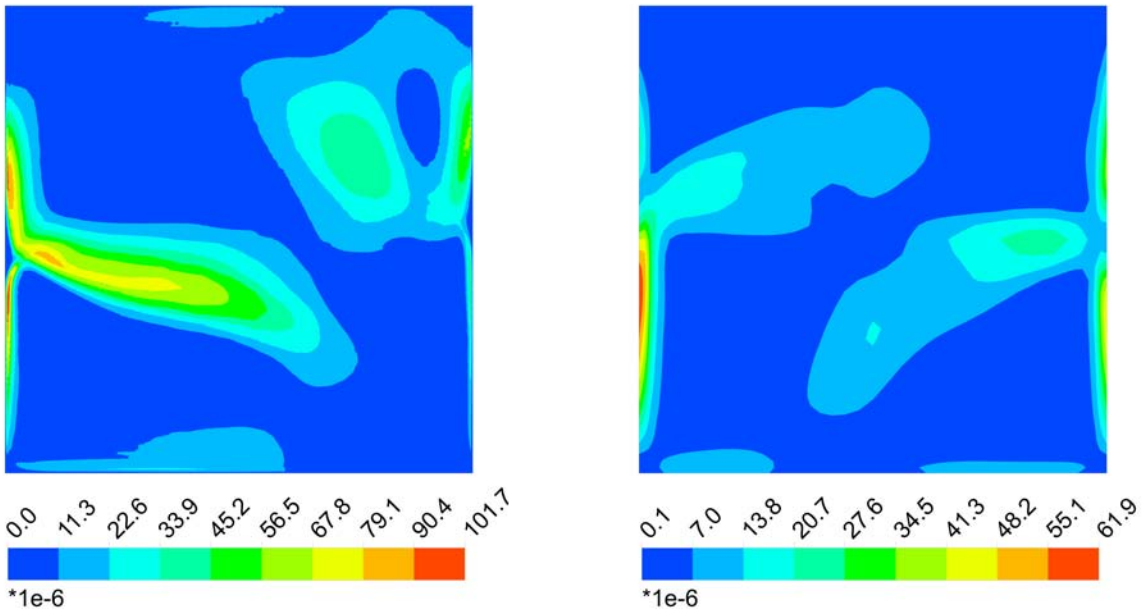

(a) TOP DC (b) BOT DC

Figure 8.8: Turbulence kinetic energy distribution on horizontal plane 1 cm from the solid-liquid interface. TKE units are J/kg.

separation (reduced interaction between layers) in stratified flow.

Turbulence kinetic energy is most intensive in the zones between vortexes, but it's generation most likely appears in the streams near the side walls due to shear stresses. Small turbulent structures are then transported with the flow towards the location where flow branches merge in one jet. This can be seen on figure 8.8a where two maximums are located next to the left wall, where high velocities appear. Since velocity on the wall is zero, strong shear stress generates turbulence here. In the middle zone, TKE maximum is in the same location as flow jet. Turbulence kinetic energy dissipates by moving further away from the wall because turbulence generation is insignificant at this location due to small shear stresses.

To quantify the flow motion and turbulence intensity in different layers of stratified flow, horizontal average α of local quantity α_l is introduced as

$$\alpha(z) = \frac{1}{2\Delta z} \int_{z-\Delta z}^{z+\Delta z} \alpha_l(\zeta) d\zeta$$

Here z - vertical coordinate, Δz - small deviation. Horizontally averaged quantities are shown in Figure 8.9. Distributions of $U^2/2$ and turbulence kinetic energy along height are very similar (Figures 8.9a and 8.9b). Scaling laws suggest that TKE is

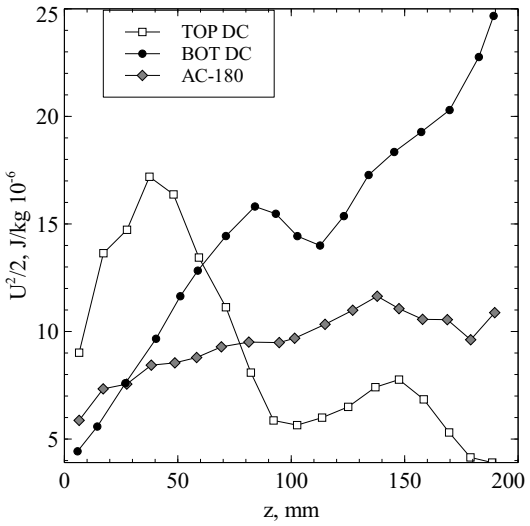

(a) $U^2/2$

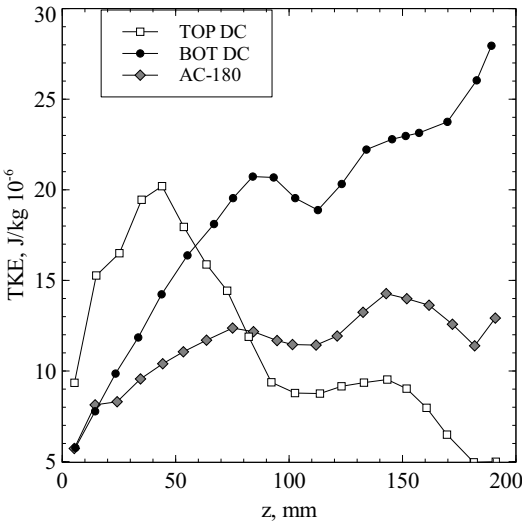

(b) $0.5(u'_x u'_x + u'_y u'_y + u'_z u'_z)$

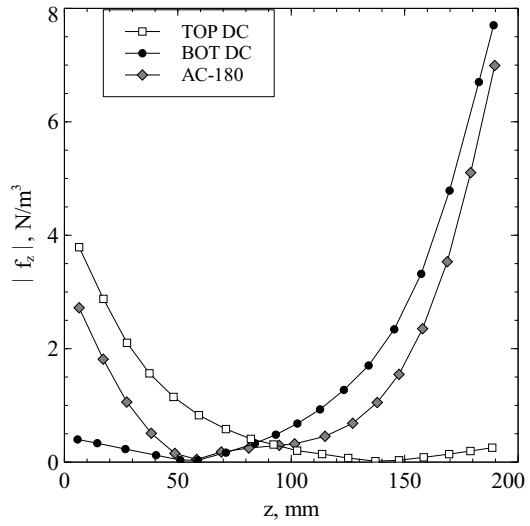

(c) Vertical force amplitude $|f_z|$

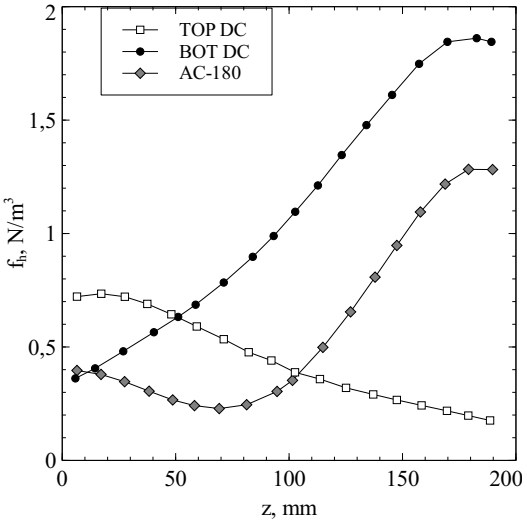

(d) Horizontal force $\sqrt{f_x^2 + f_y^2}$

Figure 8.9: Horizontally averaged quantity distribution along height of the melt

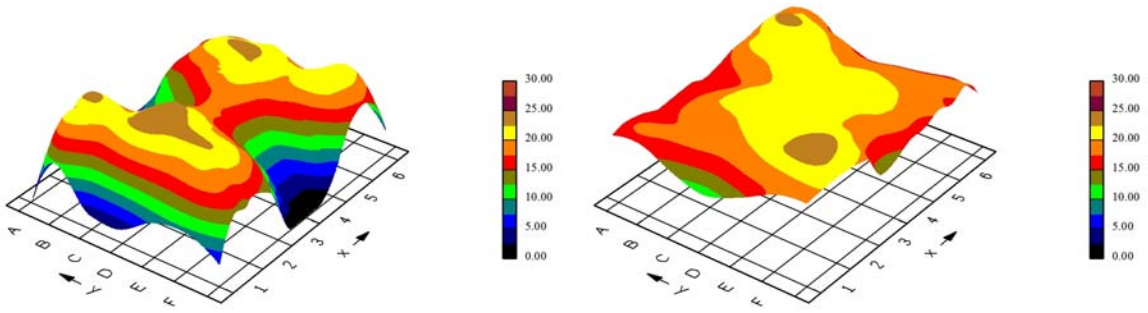

Figure 8.10: Measured seed crystal height after melting stage for two cases: TOP DC (above) and AC-180 (below). Courtesy of ALD Vacuum Technologies GmbH

proportional to velocity squared; that is illustrated by this agreement between both values.

Vertical EM forces play minor role in strongly stratified flows, which can be also shown by horizontally averaged EM force distribution. Figures 8.9c and 8.9d show horizontally averaged vertical and horizontal force distribution. Only horizontal force is in good correlation with flow energy distribution. This correlation leads to conclusion that minimization of force density near the solid-liquid interface can lead to smaller wash-out effects.

Simulations of flow allowed to understand the nature of wash-outs in seed crystals and minimize them by using different heater configurations during melting process. Figure 8.10 shows measured seed crystal height directly after melting stage for cases TOP DC and AC-180. Measurements data are property of ALD Vacuum Technologies GmbH.

Qualitatively similar results are obtained for temperature distribution near solid-liquid interface (Figure 8.11, results are shown in first element near simulation domain boundary). Lower temperature in Figure 8.11 correspons to higher seed crystal in Figure 8.10. There are certain differences in the near-wass region, which are most likely connected with fixed calculation domain. In reality, wash-outs lead to different thermal conditions and turbulent heat and mass exchange, especially if wash-outs are deep, like in TOP DC case (up to 30 mm). Nevertheless, good agreement is achieved with used model.

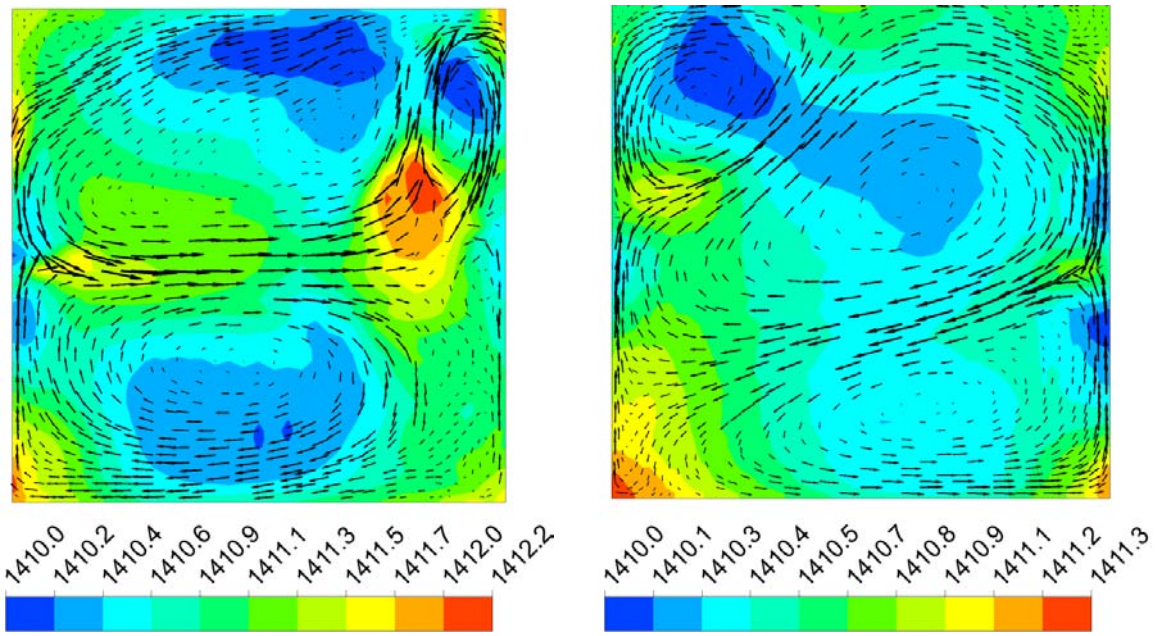

Figure 8.11: Calculated temperature distribution near solid-liquid interface and velocity field 2 cm from the interface for two cases: TOP DC on the left and AC-180 on the right

Chapter 9

Conclusions

1. Flow velocity dependence on magnetic field frequency in square-shaped domains has pronounced maximum at $\tilde{\omega} \approx 5$, which can be described by created analytic model. Such dependence for cylindrical domain has pronounced maximum at $\tilde{\omega} \approx 20$. These results are consistent with the results from literature.

2. Created saltwater similarity model showed existence of transition between full four-vortex and three-vortex regime (vortex merging). It is found that this transition occurs at typical Reynolds numbers $Re \approx 80...250$.

3. It is proven that electromagnetically driven flows can be investigated with transparent liquid (electrolyte) in system with specially designed electrodes and magnetic field guides. Such method is, however, limited to investigation of fluid dynamic phenomena only. Thermal processes in liquid metals and water cannot be compared due to large differences in Prandtl number.

4. A transition between three dimensional and stratified flow is observed at the critical Lorentz force (current in windings) at the Richardson number between 5 and 10.

5. Unsymmetrical flow pattern is observed in the stratified flow despite symmetric EM forces. This result is shown in experiment and LES simulations. Numerical simulations were validated with experimental results and good agreement was achieved.

6. Simulations showed anisotropy in velocity pulsations. The intensity of pulsations in vertical direction is smaller than in other directions, especially it was visible in volume-averaged values. At very high Richardson numbers, turbulence character is close to 2D isotropic turbulence.

7. Increase of turbulent Prandtl number with increase of Richardson number is observed in simulations, with approximation curve $Pr_T = 0.76 + 3.17Ri$. This finding is consistent with the results in atmospheric flow investigations in literature.

8. Designed setup allows higher temperature gradients than other experimental models reported in literature; therefore, further investigations under different field types (rotating, traveling, pulsating) can be interesting from practical and scientific point of view.

References

[1] H. Wirth. Aktuelle Fakten zur Photovoltaik in Deutschland (in German language), October 2014. URL: `www.pv-fakten.de`.

[2] G. del Coso, C. del Cinizo, and W.C Sinke. The impact of silicon feedstock on the pv module cost. *Solar Energy Materials and Solar Cells*, 94:345–349, 2010.

[3] C. Reimann, M. Trempa, T. Jung, J. Friedrich, and G. Muller. Modeling of incorporation of O, N, C and formation of related precipitates during directional solidification of silicon under consideration of variable processing parameters. *Journal of Crystal Growth*, 312:878–885, 2010.

[4] H.J. Möller, L. Long, M. Werner, and D. Yang. Oxygen and carbon precipitation in multicrystalline solar silicon. *Physica Status Solidi (a)*, 171:175–189, 1999.

[5] G. Du, N. Chen, and P. Rossetto. On-wafer investigation of SiC and Si3N4 inclusions in multicrystalline Si grown by directional solidificatione. *Solar Energy Materials and Solar Cells*, 92:1059, 2008.

[6] I. Silier, A. Gutjahr, F. Banhart, M. Konuma, E. Bauser, V. Schöllkopf, and H. Frey. Growth of multi-crystalline silicon on seeded glass from metallic solutions. *Materials Letters*, 28(13):87 – 91, 1996.

[7] W.O. Filtvedt, A. Holt, P.A. Ramachandran, and M.C. Melaaen. Chemical vapor deposition of silicon from silane: Review of growth mechanisms and modeling/scaleup of fluidized bed reactors. *Solar Energy Materials and Solar Cells*, 107(0):188 – 200, 2012.

[8] J. Czochralski. A new method for the measurement of the crystallization rate of metals. *Zeitschrift fr Physikalische Chemie*, 92:219 – 221, 1918.

[9] H. Jeong, Y. Lee, M. Ji, G. Lee, and H. Chung. The optimum solidification and crucible rotation in silicon czochralski crystal growth. *Journal of Mechanical Science and Technology*, 24(1):407–414, 2010.

[10] Z. Lu and S. Kimbel. Growth of 450mm diameter semiconductor grade silicon crystals. *Journal of Crystal Growth*, 318(1):193 – 195, 2011. The 16th International Conference on Crystal Growth (ICCG16)/The 14th International Conference on Vapor Growth and Epitaxy (ICVGE14).

[11] Chung-Wen Lan, Chao-Kuan Hsieh, and Wen-Chin Hsu. Czochralski silicon crystal growth for photovoltaic applications. In Kazuo Nakajima and Noritaka Usami, editors, *Crystal Growth of Si for Solar Cells*, volume 14 of *Advances in Materials Research*, pages 25–39. Springer Berlin Heidelberg, 2009.

[12] Stefan C. W. Krauter. *Solar Electric Power Generation - Photovoltaic Energy Systems*. Springer, 2006.

[13] W.G. Pfann. Principles of zone-melting. *Transactions of the American Institute of Mining and Metallurgical Engineers*, 194:747–273, 1952.

[14] B. Jayant Baliga. *Fundamentals of Power Semiconductor Devices*. Springer Publishing Company, Incorporated, 1 edition, 2008.

[15] M. Jurisch. W. Keller, A. Mühlbauer. Floating-Zone Silicon. *Kristall und Technik*, 16(12):1418–1418, 1981.

[16] T.F. Ciszek, G.H. Schwuttke, and K.H. Yang. Directionally solidified solar-grade silicon using carbon crucibles. *Journal of Crystal Growth*, 46(4):527 – 533, 1979.

[17] Ying-Yang Teng, Jyh-Chen Chen, Bo-Siang Huang, and Ching-Hsin Chang. Numerical simulation of impurity transport under the effect of a gas flow guidance device during the growth of multicrystalline silicon ingots by the directional solidification process. *Journal of Crystal Growth*, 385(0):1 – 8, 2014. The 7th International Workshop on Modeling in Crystal Growth.

[18] Liang He, Gang Wang, and Yi-ming Rong. Modeling on directional solidification of solar cell grade multicrystalline silicon ingot casting. *Journal of Shanghai Jiaotong University (Science)*, 16(3):316–319, 2011.

[19] V. Galindo, G. Gerbeth, W. von Ammon, E. Tomzig, and J. Virbulis. Crystal growth melt flow control by means of magnetic fields. *Energy Conversion and Management*, 43(3):309 – 316, 2002.

[20] Peter Rudolph. Travelling magnetic fields applied to bulk crystal growth from the melt: The step from basic research to industrial scale. *Journal of Crystal Growth*, 310(79):1298 – 1306, 2008. the Proceedings of the 15th International Conference on Crystal Growth (ICCG-15) in conjunction with the International Conference on Vapor Growth and Epitaxy and the {US} Biennial Workshop on Organometallic Vapor Phase Epitaxy.

[21] Qinghua Yu, Lijun Liu, Zaoyang Li, and Peng Su. Global simulations of heat transfer in directional solidification of multi-crystalline silicon ingots under a traveling magnetic field. *Journal of Crystal Growth*, 401(0):285 – 290, 2014. Proceedings of 17th International Conference on Crystal Growth and Epitaxy (ICCGE-17).

[22] N. Dropka, C. Frank-Rotsch, and P. Rudolph. Numerical study on stirring of large silicon melts by carousel magnetic fields. *Journal of Crystal Growth*, 354(1):1 – 8, 2012.

[23] ALD Vacuum Technologies. Solar-grade silicon crystallization units for multicrystalline and mono-crystalline ingot production, brochure, January 2015. URL: `http://web.ald-vt.de/cms/fileadmin/pdf/prospekte/Solarprospekt_270412.pdf`.

[24] Tong Liu, Zhiyuan Dong, Youwen Zhao, Jun Wang, Teng Chen, Hui Xie, Jian Li, Haijiang Ni, and Dianxin Huo. Purification of metallurgical silicon through directional solidification in a large cold crucible. *Journal of Crystal Growth*, 355(1):145 – 150, 2012.

[25] R. Hull. *Properties of crystalline silicon.* London: INSPEC, the Institution of Electrical Engineers., 1999.

[26] V. Haslavsky, A. Yu. Gelfgat, and E. Kit. Experimental modelling of Czochralski melt flow with a slow crystal dummy rotation. *Acta Physica Polonica, A.*, 124(2):193 – 197, 2013.

[27] P. Hintz, D. Schwabe, and H. Wilke. Convection in a Czochralski crucible Part 1: non-rotating crystal. *Journal of Crystal Growth*, 222(12):343 – 355, 2001.

[28] A. Cramer, J. Pal, and G. Gerbeth. Model experiments for the czochralski crystal growth technique. *The European Physical Journal Special Topics*, 220(1):259–273, 2013.

[29] K. Dadzis, J. Ehrig, K. Niemietz, O. Pätzold, U. Wunderwald, and J. Friedrich. Model experiments and numerical simulations for directional solidification of multicrystalline silicon in a traveling magnetic field. *Journal of Crystal Growth*, 333:7–15, 2011.

[30] K. Dadzis, K. Niemietz, O. Pätzold, U. Wunderwald, and J. Friedrich. Non-isothermal model experiments and numerical simulations for directional solidification of multicrystalline silicon in a traveling magnetic field. *Journal of Crystal Growth*, 372:1454–156, 2013.

[31] Y.Y. Teng, J.C. Chen, B.S. Huang, and C.H. Chang. Numerical simulation of impurity transport under the effect of a gas flow guidance device during the growth of multicrystalline silicon ingots by the directional solidification process. *Journal of Crystal Growth*, 385:1–8, 2014.

[32] N. Dropka, W. Miller, R. Menzel, and U. Rehse. Numerical study on transport phenomena in a directional solidification process in the presence of travelling magnetic fields. *Journal of Crystal Growth*, 312:1407–1410, 2010.

[33] O. Zikanov and A. Thess. Direct numerical simulation as a tool for understanding MHD liquid metal turbulence. *Applied Mathematical Modelling*, 28:1–13, 2004.

[34] X. Wang, Y. Fautrelle, J. Etay, and R. Moreau. A periodically reversed flow driven by a modulated traveling magnetic field: Part I. experiments with GaInSn. *Metallurgical and Materials Transactions B*, 40(1):82–90, 2009.

[35] H. K. Moffatt. Electromagnetic stirring. *Physics of Fluids A: Fluid Dynamics (1989-1993)*, 3(5):1336–1343, 1991.

[36] R. S. Rogallo and P. Moin. Numerical simulation of turbulent flows. *Annual Review of Fluid Mechanics*, 16(1):99–137, 1984.

[37] Haecheon Choi and Parviz Moin. Grid-point requirements for large eddy simulation: Chapmans estimates revisited. *Physics of Fluids (1994-present)*, 24(1):011702, 2012.

[38] Myoungkyu Lee, N. Malaya, and R.D. Moser. Petascale direct numerical simulation of turbulent channel flow on up to 786k cores. In *High Performance Computing, Networking, Storage and Analysis (SC), 2013 International Conference for*, pages 1–11, Nov 2013.

[39] M. M. Stanisić. *The mathematical theory of turbulence*. Universitext. Springer-Verlag, New York, 1985.

[40] D.C. Wilcox. *Turbulence Modeling for CFD*. DCW Industries, Incorporated, 1994.

[41] F. R. Menter. Two-equation eddy-viscosity turbulence models for engineering applications. *AIAA Journal*, 32(8):1598–1605, 1994.

[42] Vadims Geža, Rade Ž. Milenković, Ralf Kapulla, Sergejs Dementjevs, Andris Jakovičs, and Michael Wohlmuther. Computational and experimental studies of the flow field near the beam entrance window of a liquid metal target. *Nuclear Engineering and Design*, 275(0):96 – 106, 2014.

[43] J.-J. Lee, S.J. Yoon, G.-C. Park, and W.-J. Lee. Turbulence-induced heat transfer in pbmr core using les and rans. *Journal of Nuclear Science and Technology*, 44(7):985–996, 2007.

[44] S. B. Pope. *Turbulent flows*. Cambridge, Cambridge University Press, 2000.

[45] J. Smagorinsky. General circulation experiments with the primitive equations. *Monthly Weather Review*, 91(3):99–164, 1963.

[46] A. N. Kolmogorov. The local structure of turbulence in incompressible viscous fluid for very large Reynolds numbers. *Proceedings: Mathematical and Physical Sciences*, 434(1890):pp. 9–13, 1991.

[47] K. R. Sreenivasan. On the universality of the Kolmogorov constant. *Physics of Fluids*, 7(11):2778–2784, 1995.

[48] G. I. Taylor. Statistical theory of turbulence. *Proceedings of the Royal Society of London A: Mathematical, Physical and Engineering Sciences*, 151(873):421–444, 1935.

[49] T. de Karman and L. Howarth. On the statistical theory of isotropic turbulence. *Proceedings of the Royal Society of London A: Mathematical, Physical and Engineering Sciences*, 164(917):192–215, 1938.

[50] G. I. Taylor. The spectrum of turbulence. *Proceedings of the Royal Society of London A: Mathematical, Physical and Engineering Sciences*, 164(919):476–490, 1938.

[51] R.V. Ozmidov. On turbulent exchange in stable stratified ocean. *Izvestia Academii Nauk USSR, Atmosphere and Ocean Physics*, 8:493–497, 1965.

[52] William K. George and Hussein J. Hussein. Locally axisymmetric turbulence. *Journal of Fluid Mechanics*, 233:1–23, 12 1991.

[53] J.L. Lumley and G.R Newmans. The return to isotropy of homogeneous turbulence. *Journal of Fluid Mechanics*, 81:161–178, 1977.

[54] V.Geža, A.Jakovičs, U.Krieger, and B.Halbedel. Modelling of electromagnetic heating and mixing conditions in glass melt output equipment. *COMPEL: The International Journal for Computation and Mathematics in Electrical and Electronic Engineering*, 30(5):1467–1478, 2011.

[55] S. O. Reza Moheimani and A. J. Fleming. *Piezoelectric Transducers for Vibration Control and Damping*. Springer London, 2006.

[56] A.Cramer, G. Gerbeth, P. Terhoeven, and A. Krätzschmar. Fluid velocity measurements in electrovortical flows. *Materials and Manufacturing Processes*, 19:665–678, 2004.

[57] M.Sajben. Hot wire anemometer in liquid mercury. *Review of Scientific Instruments*, 36:945–953, 1965.

[58] I.Platnieks and G.Uhlmann. Hot-wire sensor for liquid sodium. *Journal of Physics E: Scientific Instruments*, 17:862–863, 1984.

[59] S. Eckert, A. Cramer, and G. Gerbeth. Velocity measurement techniques for liquid metal flows. *Fluid Mechanics and Its Applications: Magnetohydrodynamics*, 80:275–294, 2007.

[60] E. Baake, A. Nikanorov, V.N. Timofeyev, and R.M. Khristinich. Melt flow measurement in aluminium alloys in electromagnetic stirred industrial furnace. In *Proceedings of the International Scientific Colloquium Modelling for Electromagnetic Processing*, number 3-00-011073-9, pages 273–278. ISBN, 2003.

[61] H.Hayashi, A.Becker, and J.W.Evans. Towards a probe for velocity measurements in molten metals at high temperatures. *Metallurgical ant Materials Transactions B*, 30B:623–630, 1999.

[62] R. Kapulla, B. Sigg, S. Horanyi, and M. Hudina. Local velocity measurements in a thermally-stratified sodium mixing layer using a permanent-magnet probe. *Experimental Thermal and Fluid Science*, 20:115–136, 2000.

[63] M. Kirpo. *Modeling of Turbulence Properties and Particle Transport in Recirculated Flows*. PhD thesis, University of Latvia, 2009.

[64] A. Cramer, K. Varshney, Th. Gundrum, and G. Gerbeth. Experimental study on the sensitivity and accuracy of electric potential local flow measurements. *Flow Measurement and Instrumentation*, 17(1):1 – 11, 2006.

[65] Y. Takeda. Ultrasonic Doppler method for velocity profile measurement in fluid dynamics and fluid engineering. *Experiments in Fluids*, 26:177–178, 1999.

[66] S. Eckert, G. Gerbeth, and V. I. Melnikov. Velocity measurements at high temperatures by ultrasound Doppler velocimetry using an acoustic wave guide. *Experiments in Fluids*, 35:381–388, 2003.

[67] L. Büttner, R. Nauber, M. Burger, D. Räbiger, S. Franke, S. Eckert, and Jürgen Czarske. Dual-plane ultrasound flow measurements in liquid metals. *Measurement Science and Technology*, 24(5):055302, 2013.

[68] F. Stefani, T. Gundrum, and G. Gerbeth. Contactless inductive flow tomography. *Physical Review E*, 70:056306, Nov 2004.

[69] Y. Takeda. Velocity profile measurement by ultrasound Doppler shift method. *International Journal of Heat and Fluid Flow*, 7(4):313–318, 1986.

[70] Signal Processing S.A. DOP3000 series, user's manual. software: 4.03, revision 1.

[71] Y. Takeda. Instantaneous velocity profile measurement by ultrasonic Doppler method. *JSME International Journal Series B Fluids and Thermal Engineering*, 38(1):313–318, 1995.

[72] Signal Processing S.A. DOP3010 internal architecture overview, December 2014. URL: `http://www.signal-processing.com/`.

[73] Velocimetry Technology. Particle image velocimetry, March 2015. URL: `http://velocimetry.net/principle.htm`.

[74] H. K. Moffatt. On fluid flow induced by a rotating magnetic field. *Journal of Fluid Mechanics*, 22:521–528, 7 1965.

[75] A.D. Sneyd. Theory of electromagnetic stirring by AC fields. *IMA Journal of Management Mathematics*, 5(1):87–113, 1993.

[76] L. L. Tir. Features of mechanical energy transfer to a closed metal circuit in electromagnetic systems with azimuthal currents. *Magnetohydrodynamics*, 12:100–108, 1976.

[77] G.I. Taylor and A.E. Green. Mechanism of the production of small eddies from large ones. *Proceedings of the Royal Society of London A: Mathematical, Physical and Engineering Sciences*, 158(895):499–521, 1937.

[78] N. El-Kaddah, J. Szekely, E.Taberlet, and Y. Fautrelle. Turbulent recirculating flow in induction furnaces: A comparison of measurements with predictions over a range of operating conditions. *Metallurgical Transactions B*, 17B:687–693, 1986.

[79] F. Taberlet and Y. Fautrelle. Turbulent stirring in an experimental induction furnace. *Journal of Fluid Mechanics*, 159:409–431, 1985.

[80] J. C. R. Hunt and M. R. Maxey. Estimating velocities and shear stresses in turbulent flows of liquid metals driven by low frequency electromagnetic fields. In *Proceedings of the 2nd Bat-Sheva Intl. Seminar on MHD Flows and Turbulence*, pages 249–269, 1978.

[81] R. Moreau. *Magnetohydrodynamics*. 3rd ed. Dordrecht / Boston / London, Kluwer Academic Publishers, 1990.

[82] E. Baake. *Grenzleistungs- und Aufkohlungsverhalten von Induktions-Tiegelöfen*. PhD thesis, Institut für Elektrowärme der Universität Hannover, 1994.

[83] G. Arfken. *Mathematical Methods for Physicists*. 3rd ed. Orlando, FL: Academic Press, 1988.

[84] J.R. Bowler and T.P. Theodoulidis. Eddy currents induced in a conducting rod of finite length by a coaxial encircling coil. *J. Phys. D: Appl. Phys.*, 38:2861–2868, 2005.

[85] T. Theodoulidis and J. Bowler. Eddy current interaction of a long coil with a slot in a conductive plate. *IEEE Transactions on Magnetics*, 41:1238–1247, 2005.

[86] L.L. Tir and M.Y. Stolov. *Electromagnetic Devices to Influence the Circulation in Electric Furnaces (in russian)*. Moscow, Metallurgia, 1975.

[87] M. E. Brachet. Direct simulation of three-dimensional turbulence in the Taylor-Green vortex. *Fluid Dynamics Research*, 8(1-4):1, 1991.

[88] M.E. Brachet, D. Meiron, S. Orszag, B. Nickel, R. Morf, and U. Frisch. The Taylor-Green vortex and fully developed turbulence. *Journal of Statistical Physics*, 34(5-6):1049–1063, 1984.

[89] A. Pouquet, E. Lee, M. Brachet, P.D. Mininni, , and D.L. Rosenberg. The dynamics of unforced turbulence at high Reynolds number for Taylor–Green vortices generalized to MHD. *Geophysical and Astrophysical Fluid Dynamics*, 104:115–134, 2010.

[90] C. Nore, M. Abid, and M. E. Brachet. Decaying Kolmogorov turbulence in a model of superflow. *Physics of Fluids (1994-present)*, 9(9):2644–2669, 1997.

[91] G. Krstulovic, G. Thorner, J.P. Vest, S. Fauve, and M. Brachet. Axial dipolar dynamo action in the Taylor-Green vortex. *Physical Review E*, 84(6):066318, 2011.

[92] B. Andreotti, S. Douady, and Y. Couder. An experiment on two aspects of the interaction between strain and vorticity. *Journal of Fluid Mechanics*, 444:151–174, 2001.

[93] R.R. Lagnado and L.G. Leal. Visualization of three-dimensional flow in a four-roll mill. *Experiments in Fluids*, 9(1-2):25–32, 1990.

[94] Yu.A. Aryshev, V.A. Golovin, and Sh.A. Ershin. Stability of colliding flows. *Fluid Dynamics*, 16(5):755–759, 1981.

[95] O.S. Kerr and J.W. Dold. Periodic steady vortices in a stagnation point flow. *Journal of Fluid Mechanics*, 276:307–325, 1994.

[96] K. Brattkus and S.H. Davis. The linear stability of plane stagnation-point flow against general disturbances. *Quarterly Journal of Mechanics and Applied Mathematics*, 44:135–146, 1991.

[97] J. Sommeria and J. Verron. An investigation of nonlinear interactions in a twodimensional recirculating flow. *Physics of Fluids (1958-1988)*, 27(8):1918–1920, 1984.

[98] A. Thess. Instabilities in two-dimensional spatially periodic flows. Part II: Square eddy lattice. *Physics of Fluids A: Fluid Dynamics (1989-1993)*, 4(7):1396–1407, 1992.

[99] V. Dallas and A. Alexakis. Symmetry breaking of decaying magnetohydrodynamic Taylor-Green flows and consequences for universality. *Physical Review E*, 88:063017, Dec 2013.

[100] T. Gau and Y. Hattori. Modal and non-modal stability of two-dimensional Taylor-Green vortices. *Fluid Dynamics Research*, 46(3):031410, 2014.

[101] M. Lauret, L. P. J. Kamp, G. J. F. van Heijst, M. R. de Baar, and H. Nijmeijer. Experimental stabilisation of 2D vortex patterns using time-dependent forcing. *EPL (Europhysics Letters)*, 104(2):24003, 2013.

[102] C. Cerretelli and C.H.K. Williamson. The physical mechanism for vortex merging. *Journal of Fluid Mechanics*, 475:41–77, 2003.

[103] P. Capran and J. Verron. Numerical simulation of a physical experiment on two-dimensional vortex merging. *Fluid Dynamics Research*, 3(1-4):87, 1988.

[104] D. Byrne, H. Xia, and M. Shats. Robust inverse energy cascade and turbulence structure in three-dimensional layers of fluid. *Physics of Fluids*, 23:095109, 1984.

[105] A. V. Wolf. *Aqueous Solutions and Body Fluids.* Harper and Row, New York, 1966.

[106] S.S. Zilintikevich, T. Elperin, N. Kleeorin, I. Rogachevskii, I. Esau, T. Mauritsen, and M. Miles. Turbulence energetics in stably stratified geophysical flows: Strong and weak mixing regimes. *Quarterly Journal of the Royal Meteorological Society*, 134:793–799, 2008.

[107] H A Kuhn, W F Hughes, and E W Gaylord. Measurements of the viscosity of liquid Wood's metal. *British Journal of Applied Physics*, 13(10):527, 1962.

[108] W.D. Smith and J.N. Moun. Anisotropy of turbulence in stably stratified mixing layers. *Physics of Fluids*, 12:1343–1362, 2000.

[109] S. M. Murman. A scalar anisotropy model for turbulent eddy viscosity. *International Journal of Heat and Fluid Flow*, 42:115–130, 2013.

[110] S. K. Venayagamoorthy and D. D. Stretch. On the turbulent Prandtl number in homogeneous stably stratified turbulence. *Journal of Fluid Mechanics*, 644:359–369, 2010.

[111] S. Sukoriansky, B. Galperin, and I. Staroselsky. A quasinormal scale elimination model of turbulent flows with stable stratification. *Physics of Fluids*, 17:085107, 2005.

[112] P. S. Anderson. Measurement of Prandtl number as a function of Richardson number avoiding self-correlation. *Boundary-Layer Meteorology*, 131:345–362, 2009.

[113] F. P. Incropera. *Fundamentals of Heat and Mass Transfer*. John Wiley & Sons, 2006.

[114] M. Trempa, C. Reimann, J. Friedrich, G. Müller, and D. Oriwol. Monocrystalline growth in directional solidification of silicon with different orientation and splitting of seed crystals. *Journal of Crystal Growth*, 351(1):131 – 140, 2012.